Spectroscopic and Molecular Dynamics Study of Solvation and Translational Dynamics in Ionic Liquids

Eric Wu
Department of Chemistry
Carnegie Mellon University

Preface

This dissertation is submitted for the degree of Doctor of Philosophy at the Carnegie Mellon University. The research reported below was conducted by the author, Eric Wu, under the supervision of Dr. Linda A. Peteanu and Dr. Hyung J. Kim in the Department of Chemistry between August 2011 and February 2017.

The work reported in this dissertation is to the best of my knowledge original. I was responsible for all data collection and analysis. A version of chapter 2 has been published [Wu, E. C.; Kim, H. J. MD Study of Stokes Shifts in Ionic Liquids: Temperature Dependence. *J. Phys. Chem. B,* **2016**, *120* 4644–4653.] A version of chapter 3 has been published [Wu, E. C.; Kim, H. J.; Peteanu, L. A. Spectroscopic and MD Study of Dynamic and Structural Heterogeneities in Ionic Liquids. *J. Phys. Chem. B*, **2017**, *121*, 1100–1107.] A version of chapter 4 is currently being prepared for submission to a journal.

Eric C. Wu

January 2017

Acknowledgements

I would like to express my sincere gratitude to my advisors, Dr. Hyung J. Kim and Dr. Linda A. Peteanu, for their excellent guidance and support throughout my graduate school career. Their knowledge and countless discussions with them were invaluable, and guided me to think critically about my projects. I never would have been able to get through graduate school without their suggestions, criticisms, and support.

Next I would like to thank my committee members, Dr. Maria Kurnikova, Dr. Ryan Sullivan, and Dr. Sean Garrett-Roe for their help with the original proposal, ABD meetings, and thesis defense.

I would like to thank the Peteanu and Kim group members for their friendships and endless support; in no particular order, Dr. Nilesh Dhumanl, Dr. Hyunjun Kim, Andrew DeYoung, Jon Wilcox, Jiannan Liu, Hadi Abroshan, Dr. Fangyong Yan, Yao Li, Christian Legaspi, Dr. Sourav Dey, Woong Young So, Sikandar Abbas, Dr. John Pettersson, and numerous undergraduate students. Countless discussions, both scientific and non-scientific, were had.

Next, I would like to thank Dr. Shinji Saito from Institute for Molecular Science at Okazaki, Aichi, Japan. The month at Japan and the discussions about computational chemistry were invaluable. I would also like to thank Dr. Toshifumi Mori and Dr. Shin-ichi Koda for their help during my stay in Japan.

A bunch of thanks to my friends, students, and people I met at Carnegie Mellon University. In this regard, I would like to thank Katie Hanson, Ashley Wong, Jackie Lee, Christina Cabana, and Sarah Deluty for their never-ending support and countless late-nights working together.

Lastly, I would like to thank my parents, my sister, and my wife for their support throughout my entire graduate school career.

Table of Contents

List of Tables

List of Figures and Schemes

Chapter 1. Introduction to Ionic Liquids

Room temperature ionic liquids (RTILs or ILs) are a class of chemical salts that have low melting points and are liquids at room temperature. The cations are either nitrogen-based (ammonium, imidazolium, pyrazolium, pyridinium, and pyrrolidinium), sulfur-based (sulfonium), or phosphate-based (phosphonium), and the anions are either organic (*e.g.* acetate) or inorganic (e.g. PF_6^-). For each class of cations and anions, many modifications are possible, such as changing alkyl chain length or adding additional functional groups. The number of ILs that can be synthesized is, therefore, nearly infinite.[1] In addition to pure ILs, mixtures of ILs have also been used in many applications.[2–11] By creating mixtures of ILs, the number of possible ILs increases exponentially and these mixtures of ILs have enabled additional methods for fine-tuning the physical and chemical properties of these materials. With such a large number of available ILs, a better understanding of the structure and dynamic of ILs is needed to facilitate the development of task-specific ILs.

In addition to the ease of modification, ILs have many desirable properties, including non-volatility, non-flammability, good thermal stability, high intrinsic ion concentration, high conductivity, and wide electrochemical windows.[12] On the other hand, because of their ionic nature and strong coulombic interactions, one of the drawbacks of ILs are their viscosity. With these interesting properties, ILs have found applications in many different areas. These include synthesis (as catalysts or solvents),[13–19] energy storage (such as lithium batteries, capacitors, or dye-sensitized solar cells),[20–25] gas separations and storage,[26–32] and biofuel production.[12,33]

ILs show both structural and dynamic heterogeneity. For example, experiments and simulations have shown that ILs form nonpolar and polar domains.[34–40] The nonpolar alkyl chains and the charged groups aggregate separately and form interconnected nonpolar and polar regions. In addition to the heterogeneous structure, the solvation dynamics of ILs are very complex and stretch over a broad range of timescales. The solvation response of ILs can generally be divided into two time domains, a sub-picosecond ultrafast domain and a slow region that stretches over several nanoseconds.[41,42] The sub-picosecond ultrafast region accounts for roughly 50% of the relaxation within several hundred femtoseconds.[43,44] The remainder of the relaxation takes place over several nanoseconds, which is many orders of magnitude longer. The slow relaxation is complex, and is usually best-fitted with a stretched exponential function ($e^{-t^{\beta}}$), with $\beta = 0.3{\sim}0.4$.[45,46]

In addition to the complex solvation relaxation dynamics, translational and rotational motions in ILs are also heterogeneous. MD simulations have shown, using non-Gaussian parameters and van Hove functions, that the translational motion of ILs deviate from diffusive motion.[47–51] Experimentally, the intermediate scattering function of ILs show both α-relaxation and β-relaxation.[52,53,54] Due to the strong Coulombic interactions, the intermediate regime of the translational motion is dominated by caging motion, which causes the motion to become sub-diffusive.

In this thesis, we used both spectroscopic experiments and molecular dynamic simulations to study solvation in ILs. First, we examined the temperature dependence of the Stokes shift and the solvation dynamics (Chapter II) and probed whether there is a connection between structural and dynamic heterogeneity (Chapter III). We also used fluorescence correlation spectroscopy (FCS) to examine the solvation of conjugated

polymers in ILs (Chapters IV and V). To speed up MD simulations, we developed a coarse-grained description of IL and used it to study phase separation in supported polymeric ILs (Chapter VI).

Experimentally, we primarily used single-molecule fluorescence spectroscopy. The advantage of single-molecule measurements over bulk measurements is the ability to monitor subpopulations. With bulk measurements, the values obtained are ensemble averages that do not give a description of various subpopulation. The single molecule technique of choice here is confocal microscopy and fluorescence correlation spectroscopy. For confocal microscopy, excitation light is focused into a small volume of the sample using a microscope objective. The fluorescence is collected using the same objective, and a pinhole is placed between the detectors and the sample to eliminate the out-of-focus light. Fluorescence correlation spectroscopy studies the translational motion of fluorescent probes by monitoring the intensity fluctuations within the focal volume.

Molecular dynamic (MD) simulations were also performed. MD simulations model the system using classical Newtonian mechanics, and the motions of the electrons are ignored. Bonds and bond angles are modeled as harmonic springs, and dihedral angles are modeled using periodic functions. Nonbonded interactions are modeled using Lennard-Jones potentials and Coulomb potentials. All simulations were performed using the GROMACS package.

References

1. Katritzky, A. R.; Jain, R.; Lomaka, A.; Petrukhin, R.; Karelson, M.; Visser, A. E.; Rogers, R. D. Correlation of the Melting Points of Potential Ionic Liquids (Imidazolium

Bromides and Benzimidazolium Bromides) Using the CODESSA Program. *J. Chem. Inf. Comput. Sci.*, **2002**, *42*, 225–231.
2. Pinto, A. M.; Rodriguez, H. Colon, Y. J.; Arce, Jr. A.; Arce, A.; Soto, A. Absorption of Carbon Dioxide in Two Binary Mixtures of Ionic Liquids. *Ind. Eng. Chem. Res.***, 2013**, *52*, 5975–5984.
3. Ivanova, A. S.; Brinzer, T.; Roth, E. A.; Kusuma, V. A.; Watkins, J. D.; Zhou, X.; Luebke, D.; Hopkinson, D.; Washburn, N. R.; Garret-Roe, S.; Nulwala, H. B. Eutectic Ionic Liquid Mixtures and Their Effect on CO_2 Solubility and Conductivity, *RSC Adv.*, **2015**, *5*, 51407.
4. Niedermeyer, H.; Hallett, J. P.; Villar-Garcia, I. J.; Hunt, P. A. Mixtures of Ionic Liquids. *Chem. Soc. Rev.*, **2012**, *41*, 7780–7802.
5. Finotello, A.; Bara Jason, E.; Narayan, S.; Camper, D.; Noble Richard, D. J. Ideal Gas Solubilities and Solubility Selectivities in a Binary Mixture of Room-Temperature Ionic Liquids. *J. Phys. Chem. B*, **2008**, *112*, 2335.
6. Zistler, M.; Wachter, P.; Schreiner, C.; Fleischmann, M.; Gerhard, D.; Wasserscheid, P.; Hinsch, A.; Gores, H. J. J. *Electrochem. Soc.*, **2007**, *154*, B925.
7. Wang, P.; Zakeeruddin, S. M.; Humphry-Baker, R.; Graetzel, M. A Binary Ionic Liquid Electrolyte to Achieve ≥7% Power Conversion Efficiencies in Dye-Sensitized Solar Cells. *Chem. Mater.*, **2004**, *16*, 2694.
8. Hao, F.; Lin, H.; Liu. Y; Yang, G.; Wang, G.; Li, J. Evidence for Enhancing Charge Collection Efficiency with an Alternative Cost-Effective Binary Ionic Liquids Electrolyte Based Dye-Sensitized Solar Cells. *Electrochim. Acta*, **2011**, *56*, 5605.
9. Hao, F.; Lin, H.; Liu, Y.; Li, J. Anionic Structure-Dependent Photoelectroschemical Responses of Dye-Sensitized Solar Cells Based on a Binary Ionic Liquid Electrolyte. *Phys. Chem. Chem. Phys.*, **2011**, *13*, 6416.
10. Khosropour, A. R.; Mohammadpoor-Baltork, I.; Kiani, F. Green, New and Efficient Tandem Oxidation and Conversion of Aryl Alcohols to 2,4,6-Triarylpyridines Promoted by [Hmim][NO3][Bmim][BF4] as a Binary Ionic Liquid. *C. R. Chim.*, **2011**, *14*, 441.
11. Baltazar, Q. Q.; Leininger, S. K.; Anderson, J. L. Binary Ionic Liquid Mixtures as Gas Chromatography Stationary Phases for Improving the Separation of Selectivity of Alcohols and Aromatic Compounds. *J. Chromatogr. A*, **2008**, *1182*, 119.
12. Welton, T., Ionic Liquids in Catalysis. *Coordination Chemistry Reviews* **2004,** 248, 2459–2477.
13. Scholten, J. D.; Leal, B. C.; Dupont, J. Transition Metal Nanoparticle Catalysis in Ionic Liquids. *ACS Catal.*, **2011**, *2*, 184.
14. Sheldon, R. Catalytic Reactions in Ionic Liquids. *Chem. Commun*., **2001**, 2399.
15. Muldoon, M. J.; Aki, S. N. V. K.; Anderson, J. L.; Dixon, J. K.; Brennecke, J. F. Improving Carbon Dioxide Solubility in Ionic Liquids. *J. Phys. Chem. B*, **2007**, *111*,9001.
16. Heldebrant, D. J.; Witt, H. N.; Walsh, S. M.; Ellis, T.; Rauscher, J.; Jessop, P. G. Liquid Polymers as Solvents for Catalytic Reductions. *Green Chem.*, 2006, 807–815.
17. Cole, A. C.; Jensen, J. L.; Ntai, I.; Tran, K. L. T.; Weaver, K. J.; Forbes, D. C.; Davis, Jr., J. H. Novel Brønsted Acidic Ionic Liquids and Their Use as Dual Solvent-Catalysts. *J. Am. Chem. Soc.*, **2002**, *124*, 5962–5963.
18. Oliveira, F. C. C.; Effenberger, F. B.; Sousa, M. H.; Jardim, R. F.; Kiyohara, P. K.; Dupont, J.; Rubim, J. C.; Rossi, L.M. Ionic Liquids as Recycling Solvents for the Synthesis of Magnetic Nanoparticles. *Phys. Chem. Chem. Phys.*, **2001**, *13*, 13558–13564.

19. Rogers, R. D.; Seddon, K. R. Ionic Liquids – Solvents of the Future? *Science*, **2003**, 792–793.
20. Noda, A.; Susan, M. A. B. H.; Kudo, K.; Mitsushima, S.; Hayamizu, K.; Watanabe, M. Brønsted Acid-Base Ionic Liquids as Proton-Conducting Nonaqueous Electrolytes. *J. Phys. Chem. B*, **2003**, *107*, 4024–4033.
21. Xiang, H. F.; Yin, B.; Wang, H.; Lin, H. W.; Ge, X. W.; Xie, S.; Chen, C. H. Improving Electrochemical Properties of Room Temperature Ionic Liquid (RTIL) Based Electrolyte for Li-Ion Batteries. *Electrochimica Acta*, **2010**, *55*, 5204–5209.
22. Abraham, T. J.; MacFarlane, D. R.; Pringle, J. M. Seebeck Coefficients in Ionic Liquids – Prospects for Thermo-electrochemical Cells. *Chem. Commun.*, **2011**, *47*, 6260–6262.
23. MacFarlane, D. R.; Pringle, J. M.; Howlett, P. C.; Forsyth, M. Ionic Liquids and Reactions at the Electrochemical Interface. *Phys. Chem. Chem. Phys.*, **2010**, *12*, 1659–1669.
24. Lane, G. H.; Bayley, P. M.; Clare, B. R.; Best, A. S.; MacFarlane, D. R.; Forsyth, M.; Hollenkamp, A. F. Ionic Liquid Electrolyte for Lithium Melta Batteries: Physical, Electrochemical, and Interfacial Studies of N-Methyl-N-butylmorpholinium Bis(fluorosulfonyl)imide. *J. Phys. Chem. C*, **2010**, *114* 21775–21785.
25. Lane, G. H.; Best, A. S.; MacFarlane, D. R.; Forsyth, M.; Bayley, P. M.; Hollenkamp, A. F. The Electrochemistry of Lithium in Ionic Liquid/Organic Diluent Mixtures. *Electrochimica Acta*, **2010**, *55*, 8947–8952.
26. Heldebrant, D. J.; Jessop, P. G. Liquid Poly(ethylene glycol) and Supercritical Carbon Dioxide: A Begnign Biphasic Solvent System for Use and Recycling of Homogeneous Catalysis. *J. Am. Chem. Soc.*, **2003**, *125*, 5600–5601.
27. Ilconich, J.; Myers, C.; Pennline, H.; Luebke, D. Experimental Investigation of the Permeability and Selectivity of Supported Ionic Liquid Membranes for CO_2/He Separation at Temperature up to 125°C. *J. Membrane Sci.*, **2007**, *298*, 41–47.
28. Myers, C.; Pennline, H.; Luebke, D.; Ilconich, J.; Dixon, J. K.; Maginn, E. J.; Brennecke, J. F. High Temperature Separation of Carbon Dioxide/Hydrogen Mixtures Using Facilitated Supported Ionic Liquid Membranes. *J. Membrane Sci.*, **2008**, *322*, 28–31.
29. Blanchard, L. A.; Gu, Z.; Brennecke, J. F. High-Pressure Phase Behavior of Ionic Liquid/CO_2 Systems. *J. Phys. Chem. B*, **2001**, *105*, 2437–2444.
30. Yokozeki, A.; Shiflett, M. B.; Junk, C. P.; Grieco, L. M.; Foo, T. Physical and Chemical Absorptions of Carbon Dioxide in Room Temperature Ionic Liquids. *J. Phys. Chem. B*, **2008**, *112*, 16654–16663.
31. Shiflett, M. B.; Harmer, M. A.; Junk, C. P.; Yokozeki, A. Solubility and Diffusivity of Difluoromethane in Room-Temperature Ionic Liquids. *J. Chem. Eng. Data*, **2006**, *51*, 483–495.
32. Bates, E. D.; Mayton, R. D.; Ntai, I.; Davis, J. H. CO_2 Capture by a Task-Specific Ionic Liquid. *J. Am. Chem. Soc.*, **2002**, *124*, 926–927.
33. Plechkova, N. V.; Seddon, K. R., Applications of Ionic Liquids in the Chemical Industry. *Chemical Society Reviews* **2008,** 37, 125-150.
34. Mandal, P. K.; Sarkar, M.; Samanta, A., Excitation-Wavelength-Dependent Fluorescence Behavior of Some Dipolar Molecules in Room-Temperature Ionic Liquids. *Journal of Physical Chemistry A* **2004,** 108, 9048–9053.

35. Paul, A.; Mandal, P. K.; Samanta, A., On the Optical Properties of the Imidazolium Ionic Liquids. *Journal of Physical Chemistry B* **2005,** 109, 9148–9153.
36. Samanta, A., Dynamic Stokes Shift and Excitation Wavelength Dependent Fluorescence of Dipolar Molecules in Room Temperature Ionic Liquids. *Journal of Physical Chemistry B* **2006,** 110, 13704–13716.
37. Iwata, K.; Okajima, H.; Saha, S.; Hamaguchi, H.-O., Local Structure Formation in Alkyl-imidazolium-based Ionic Liquids as Revealed by Linear and Nonlinear Raman Spectroscopy. *Accounts of Chemical Research* **2007,** 40, 1174–1181.
38. Triolo, A.; Russina, O.; Bleif, H.-J.; Di Cola, E., Nanoscale Segregation in Room Temperature Ionic Liquids. *Journal of Physical Chemistry B* **2007,** 111, 4641–4644.
39. Lopes, J. N. A. C.; Padua, A. A. H., Nanostructural Organization in Ionic Liquids. *Journal of Physical Chemistry B* **2006,** 110, 3330–3335.
40. Wang, Y.; Voth, G. A., Tail Aggregation and Domain Diffusion in Ionic Liquids. *Journal of Physical Chemistry B* **2006,** 110, 18601–18608.
41. Chakrabarty, D.; Hazra, P.; Chakraborty, A.; Seth, D.; Sarkar, N. Dynamics of Solvent Relaxation in Room Temperature Ionic Liquids. *Chem. Phys. Letter* **2003**, *381*, 697-704.
42. Zhang, X.; Liang, M.; Ernsting, N. P.; Maroncelli, M. Complete Solvation Response of Coumarin 153 in Ionic Liquids. *J. Phys. Chem. B* **2013**, *117*, 4291-4304.
43. Shim, Y.; Duan, J.; Choi, M. Y.; Kim, H. J. Solvation in Molecular Ionic Liquids. *J. Chem. Phys.* **2003,** *119*, 6411-6414.
44. Shim, Y.; Choi, M. Y.; Kim, H. J. A Molecular Dynamics Computer Simulation Study of Room-Temperature Ionic Liquids. II. Equilibrium and Nonequilibrium Solvation Dynamics. *J. Chem. Phys.* **2005,** *122*, 044511.
45. Arzhantsev, S.; Jin, H.; Baker, G. A.; Maroncelli, M., Measurements fo the Complete Solvation Response in Ionic Liquids. *Journal of Physical Chemistry B* **2007,** 111, 4978-4989.
46. Funston, A. M.; Fadeeva, T. A.; Wishart, J. F.; Castner, E. W. J., Fluorescence Probing of Temperature-Dependent Dynamics and Friction in Ionic Liquid Local Environments. *Journal of Physical Chemistry B* **2007,** 111, 4963-4977.
47. Margulis, C. J.; Stern, H. A.; Berne, B. J. Computer Simulation of a "Green Chemistry" Room-Temperature Ionic Solvent. *J. Phys. Chem. B*, **2002**, *106*, 12017–12021.
48. Del Pópolo, M. G.; Voth, G. A. On the Structure and Dynamics of Ionic Liquids. *J. Phys. Chem. B*, **2004**, *108*, 1744–1752.
49. Cadena, C.; Zhao, Q.; Snurr, R. Q.; Maginn, E. J. Molecular Modeling and Experimental Studies of the Thermodynamic and Transport Properties of Pyridinium-Based Ionic Liquids. *J. Phys. Chem. B*, **2006**, *110*, 2821–2832.
50. Andreussi, O.; Marzari, N. Transport Properties of Room Temperature Ionic Liquids from Classical Molecular Dynamics. *J. Chem. Phys.*, **2012**, *137*, 044508.
51. Maginn, E. J. Atomistic Simulation of the Thermodynamic and Transport Properties of Ionic Liquids. *Acc. Chem. Res.*, **2007**, *40*, 1200–1207.
52. Inamura, Y.; Yamamuro, O.; Hayashi, S.; Hamaguchi, H. Dynamics Structure of a Room-Temperature Ionic Liquid bmimCl. *Phys. B Condens. Matter* **2006**, *385-386*, 732–734.

53. Yamamuro, O.; Yamada, T.; Kofu, M.; Nakakoshi, M.; Nagao, M. Hierarchical Structure and Dynamics of an Ionic Liquid 1-Octyl-3-Methylimidazolium Chloride. *J. Chem. Phys.* **2011**, *135*, 054508.
54. Kofu, M.; Nagao, M.; Ueki, T.; Kitazawa, Y.; Nakamura, Y.; Sawamura, S.; Watanabe, M.; Yamamuro, O. Heterogeneous Slow Dynamics of Imidazolium-Based Ionic Liquids Studied by Neutron Spin Echo. *J. Phys. Chem. B* **2013**, *117*, 2773–2781.

Chapter 2. MD Study of Stokes Shifts in Ionic Liquids: Temperature Dependence*

2.1. Introduction

ILs exhibit interesting solvation behaviors. Some aspects are shared by conventional polar solvents, but others are not. For example, solvent relaxation in imidazolium-based ILs is bi-phasic: a fast sub-picosecond component despite ILs' very high viscosity and a slow component that relaxes over a broad range of times from hundreds of picoseconds to tens or hundreds of nanoseconds.[55,56] The sub-picosecond component, responsible for nearly 50% of the entire relaxation, is mainly attributed to hindered translations of ions[57,58,59,60] though other motions[61] could contribute. This state of affairs is different from polar solvents, for which inertial reorientational dynamics play a major role. The hindered translational motions of ions play an important role in, e.g., optical Kerr effect[62–66] and tera-Hertz[67],[68] spectroscopies of ILs. The slow component, generally attributed to the diffusion of cations and anions, is characterized by non-exponential relaxation, such as a stretched exponential function.[57,58, 69] In order to effectively tailor ILs for different applications, their solvation dynamics and structures must be well understood.

One of the most studied solvent properties is polarity. For many chemical reactions involving charge shift and transfer, such as S_N1 and S_N2, the polarity of the solvent exerts a strong influence on reaction free energetics and thus the yield and rate of reaction.[70,71,72]

* Reprinted with permission from *J. Phys Chem B*, **2016**, 120, 4644–4653. Copyright 2016 American Chemical Society.

Many different parameters, such as dielectric constant ε_0 , $E_T(30)$, or Kamlet-Taft parameters have been used to quantify solvent polarity.[71,72,73] While their typical dielectric constant (ε_0= ~ 10–16) is not as high as that of conventional polar solvents,[74,75,76] the effective polarity of many ILs, measured as their ability to stabilize polar solutes, is comparable to and even in excess of highly polar aprotic solvents (e.g., acetonitrile) due to strong Coulomb interactions of IL ions and polar solutes, according to experimental[77–84] and theoretical[57,58, 85 , 86 , 87] studies. Another interesting property of ILs is that the temperature dependence of ε_0 is considerably weaker than conventional polar solvents. For $BMI^+PF_6^-$, Yao and co-workers found that ε_0 decreases from 12.3 at 300 K to 11.7 at 360K,[74] while Buchner, Hefter, and co-workers found that ε_0 decreases from 16.7 at 288 K to 13.0 at 338 K[75]. For other ILs, Weingärtner and co-workers found that ε_0 of $EMI^+Tf_2N^-$ decreases from 12.5 at 298K to 11.7 at 318 K, while ε_0 of $BMI^+Tf_2N^-$ essentially does not change over that temperature range.[76] In a recent MD study by Shim and Kim,[88] the weak temperature dependence of ε_0 is attributed to antagonistic roles played by translational and reorientational dynamics of IL ions, which tend to, respectively, raise and lower ε_0 as *T* rises.

Stokes shift, the energy difference between the absorption and steady-state emission of a probe molecule, is another important empirical parameter that gauges the polarity of the solvent environment via its strength of electrostatic interactions with the probe solute.[89,90] A recent theoretical analysis of Biswas and Kashyap indicated that as *T* increases from 278.15 K to 338.15 K, so does the magnitude of Stokes shift for most of the ILs they considered.[91] Experimentally, Nagasawa and co-workers studied the fluorescence behaviors of 9,9'-bianthryl in the charge-transferred state in imidazolium-based ILs.[92]

Above room temperature, the emission peak of 9,9'-bianthryl shifts to shorter wavelengths as *T* increases. This suggests that the Stokes shift would decrease with increasing *T*. For some ILs, however, as *T* increases in the temperature range $T < 280$ K, emission peak shifts to longer wavelengths, which was ascribed to emission from the unrelaxed solvation state.[92]

As above examples indicate, the effect of temperature on Stokes shift in ILs is not well understood; a clear understanding of even the direction of the shift (upshift or downshift) appears to be lacking. Therefore, in this article, we investigate this issue using MD to obtain an accurate picture on the temperature dependence of Stokes shift. For general insight, two different types of solutes, a model diatomic solute and coumarin 153, in three different ionic liquids, $EMI^+Tf_2N^-$, $EMI^+PF_6^-$ and $BMI^+PF_6^-$ are considered in a wide temperature range from 350 K to 500 K. (The melting point temperatures of these ILs are 258, 335 and 283 K, respectively.)[93] For $EMI^+Tf_2N^-$ with a relatively low melting point, its solvation properties at 300 K are also investigated. For a qualitative understanding of the MD results, dielectric continuum perspective on Stokes shift is given. The influence of temperature on solvation dynamics is also analyzed. Their short-time inertial and long-time dissipative components show rather different behaviors with *T*.

2.2. Simulation Methods

The simulation cell is composed of a solute immersed in 128 pairs of IL ions. Two different solutes are considered: a rigid diatomic solute and Coumarin 153. As for ILs, $EMI^+Tf_2N^-$, $EMI^+PF_6^-$, and $BMI^+PF_6^-$ were studied. The molecular structures of coumarin 153 and the ILs we studied are displayed in Scheme 2.1. For the rigid diatomic solute, the

solute atoms are separated by 3.5 Å, and they interact with solvent through both Lennard-Jones (LJ) and Coulomb potentials. The LJ parameters, $\sigma = 4$ Å and $\epsilon = 0.82890$ kJ/mol, and mass, 100 amu, are identical for both atoms.[57,58,85] Two charge distributions are considered: neutral pair (NP) with no dipole moment as the S_0 state, and ion pair (IP) with a dipole moment of 16.8 D as the S_1 state. All other molecules are described with the fully flexible all atom description. Specifically, the LJ and bonded parameters of the GROMACS OPLS-AA force field [94] and the charge distributions developed by Maroncelli[69,95] were employed for coumarin 153. The resulting dipole moment of the coumarin 153 model is 6.24 D for the S_0 state and 13.59 D for the S_1 state. For EMI^+, BMI^+, and Tf_2N^-, the OPLS-based force fields of refs. 96, 97, and 98 were used. For PF_6^-, the LJ parameters and charge assignment of ref. 99 and the bonded parameters of ref. 100 were used as in ref 85.

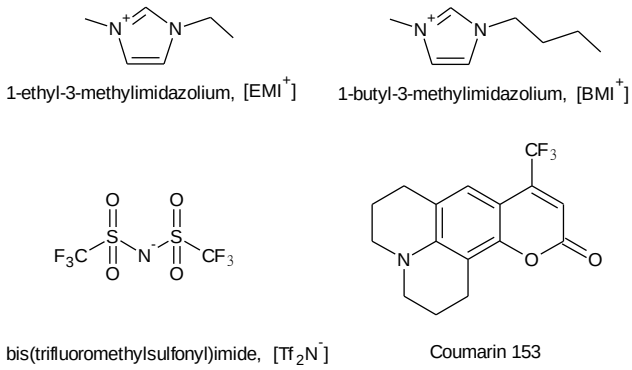

Scheme 2.1. Structure of ionic liquids and coumarin 153.

Table 2.1. Densities (g cm^{-3}) of $EMI^+Tf_2N^-$, $EMI^+PF_6^-$, and $BMI^+PF_6^-$

Solute	ILs	300 K	350 K	400 K	450 K	500 K
Diatomic Solute	$EMI^+Tf_2N^-$	22.29	22.05	21.82	21.58	21.34
	$EMI^+PF_6^-$	–	16.14	15.97	15.80	15.63
	$BMI^+PF_6^-$	–	16.90	16.78	16.54	16.36
Coumarin 153	$EMI^+Tf_2N^-$	22.28	22.04	21.80	21.57	21.33
	$EMI^+PF_6^-$	–	16.13	15.96	15.79	15.61
	$BMI^+PF_6^-$	–	16.90	16.72	16.54	16.35

All simulations were performed using the GROMACS program. [101] *NPT* simulations were first performed to determine the densities at different temperatures. The results are compiled in Table 2.1. Using these densities, *NVT* simulations were carried out. Prior to each production run, the system was annealed from 700 K to the target temperature, followed by a 10ns equilibration. Each production run was 20 ns with configurations saved every 10 fs.

Solvation of the diatomic solute and coumarin 153 in the three different ILs was simulated at five different temperatures, T = 300, 350, 400, 450 and 500 K, for $EMI^+Tf_2N^-$ and at four different temperatures, T = 350, 400, 450, and 500 K, for $EMI^+PF_6^-$ and $BMI^+PF_6^-$. Five trajectories starting from different initial configurations were simulated for each system at each temperature.

Absorption, emission and Stokes shifts ($\Delta\Delta E$) were computed by calculating the difference in the Franck-Condon (FC) energies, $\Delta E = E_{ES} - E_{GS}$, between the less dipolar ground and more dipolar excited states. For the diatomic solute, NP and IP---which

represent, respectively, the ground and excited state charge distributions---are assumed to be degenerate in energy, i.e., $E_{GS} = E_{ES}$, in vacuum. For coumarin 153, the S_0 and S_1 states have an energy gap of 64 kJ/mol in vacuum. The absorption energy ΔE_{abs} was computed by averaging ΔE over the IL configurations in equilibrium with the ground state solute charge distribution, viz., $\Delta E_{abs} = \langle \Delta E \rangle$ with IL equilibrated to the solute S_0 state. This was calculated by rerunning the ground state equilibrium trajectories with the excited state solute charge distribution. The steady-state emission energy ΔE_{ems} was determined similarly by rerunning the excited state equilibrium trajectory with the ground state solute charge distribution; i.e., $\Delta E_{ems} = \langle \Delta E \rangle$ with IL in equilibrium with the solute S_1 state. The difference between ΔE_{abs} and ΔE_{ems} defines the Stokes shift $\Delta\Delta E$ $(= \Delta E_{abs} - \Delta E_{ems})$.

Solvation dynamics were studied via the time correlation function

$$C(t) = \frac{\langle \delta\Delta E(t) \delta\Delta E \rangle}{\langle (\delta\Delta E)^2 \rangle} \tag{2.1}$$

where $\delta\Delta E(t) (= \Delta E(t) - \langle \Delta E \rangle)$ is the deviation of $\Delta E(t)$ from its equilibrium average. We note that $\delta\Delta E(t)$ is a microscopic quantity, widely used to gauge solvent dynamics.[102] 1 ns of the time correlation function, calculated for each trajectory, was averaged over 5 different trajectories. The tail of the time correlation function, where $C(t) < 0.25$, is fitted to a stretched exponential function, $a \exp\left[-(t/\tau)^{\beta}\right]$.[57, 103, 104] Solvation time, τ_s, was calculated by integrating $C(t)$

$$\tau_s = \int_0^{t_0} C(\tau)\, d\tau + \int_{t_0}^{\infty} a \exp\left[-(t/\tau)^{\beta}\right]\, d\tau \tag{2.2}$$

where the stretched exponential fitting function is used for $C(t)$ for $t > t_0$. To gain insight into the short-time inertial solvation dynamics, we have also analyzed the solvent frequency ω_s via[57,58]

$$\omega_s^2 = \frac{\langle (\Delta\dot{E})^2 \rangle}{\langle (\delta\Delta E)^2 \rangle} \tag{2.3}$$

where $\Delta\dot{E}(t)$ $(= d\Delta E/dt)$ is the time derivative of $\Delta E(t)$.

2.3. Results and Discussions

MD results are presented in Tables 2.2–2.5 and Figures 2.1–2.9. We begin with the results for Stokes shifts.

2.3.1. Stokes Shift

We first consider the diatomic solute case. In all three ILs we studied (Table 2.2), the FC energy from the equilibrated NP state to the IP state, i.e., ΔE_{abs}, is essentially the same as its gas-phase value $\Delta E_{abs} = 0$ and varies little with *T*. Since the NP state is non-dipolar (in fact, all of its electric multipole moments vanish), the solvent environment equilibrated to the NP state charge distribution neither stabilizes nor destabilizes the IP state, compared to NP. ΔE_{ems}, the FC energy from the equilibrated IP state to the NP state, on the other hand, generally increases with *T*. As a result, the Stokes shift, $\Delta\Delta E (= \Delta E_{abs} - \Delta E_{ems})$, for the diatomic solute tends to decrease as *T* increases (Figure 2). The Stokes shift in all three ILs exhibits a nearly linear dependence on *T*.

Table 2.2. $\Delta E_{abs}, \Delta E_{ems}$, and $\Delta\Delta E$ for the diatomic solute in $EMI^+Tf_2N^-$, $EMI^+PF_6^-$, and $BMI^+PF_6^-$

	ΔE_{abs}	ΔE_{ems}	$\Delta\Delta E$
$EMI^+Tf_2N^-$			
300	-1.04	-382.30	381.26
350	-0.30	-371.11	370.81
400	-0.64	-361.21	360.57
450	-0.85	-350.08	349.23
500	-0.75	-340.14	339.40
$EMI^+PF_6^-$			
350	-0.88	-384.77	383.89
400	-1.53	-374.17	372.64
450	-0.64	-363.18	362.54
500	-1.19	-355.00	353.81
$BMI^+PF_6^-$			
350	-1.74	-372.27	370.53
400	-0.52	-364.32	363.81
450	-1.03	-356.24	355.20
500	-0.65	-350.68	350.04

Since the NP and IP states are degenerate in energy in vacuum and $\Delta E = E_{IP} - E_{NP}$, the emission energy in ILs is given by a negative number of a large magnitude. All values reported are in units of kJ/mol.

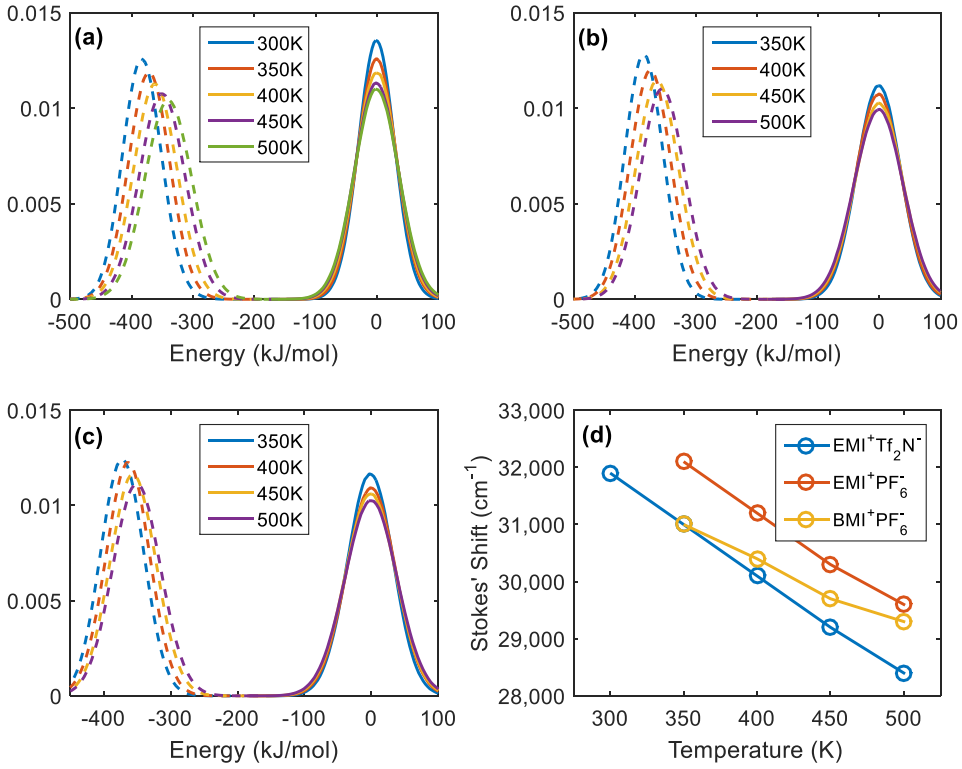

Figure 2.1. ΔE_{abs} (–) and ΔE_{ems} (- -) of diatomic solute in (a) $EMI^+Tf_2N^-$, (b) $EMI^+PF_6^-$ and (c) $BMI^+PF_6^-$, and (d) corresponding Stokes shifts

Table 2.3. $\Delta E_{abs}, \Delta E_{ems}$, and $\Delta\Delta E$ for coumarin 153 in $EMI^+Tf_2N^-$, $EMI^+PF_6^-$, and $BMI^+PF_6^-$. All values reported are in units of kJ/mol.

	ΔE_{abs}	ΔE_{ems}	$\Delta\Delta E$
$EMI^+Tf_2N^-$			
300	56.45	26.78	29.67
350	55.07	28.02	27.05
400	54.86	28.78	26.08
450	54.55	29.35	25.20
500	54.64	30.31	24.34
$EMI^+PF_6^-$			
350	55.24	23.11	32.14
400	54.16	24.58	29.58
450	54.33	25.09	29.24
500	53.86	26.30	27.56
$BMI^+PF_6^-$			
350	54.98	26.10	28.88
400	53.52	26.22	27.30
450	53.37	26.95	26.43
500	53.67	27.78	25.90

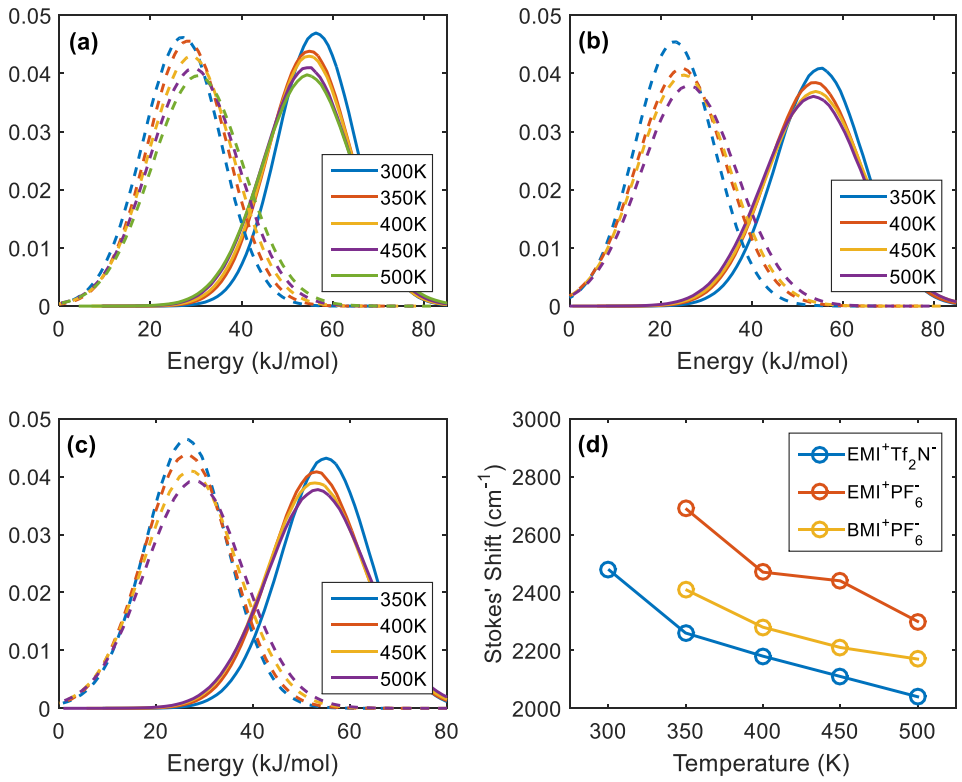

Figure 2.2. ΔE_{abs} (–) and ΔE_{ems} (- -) of coumarin 153 in (a) $EMI^+Tf_2N^-$, (b) $EMI^+PF_6^-$ and (c) $BMI^+PF_6^-$, and (d) corresponding Stokes Shifts.

Turning to coumarin 153, we found that ΔE_{abs} and ΔE_{ems} decreases and increases, respectively, as T grows (Table 2.3 and Figure 2.2). As a result, its Stokes shift tends to decrease just like the diatomic solute case. In all three ILs, a large decrease in Stokes shifts is observed from 300 K to 350 K ($EMI^+Tf_2N^-$) or from 350 K to 400 K ($EMI^+PF_6^-$ and $BMI^+PF_6^-$). Above 400 K, the T-dependence of Stokes shift becomes weaker (Figure 3). It is worthy of note that the FC energy for $BMI^+PF_6^-$ varies significantly among the 5 trajectories we simulated for both the S_0 and S_1 states at 350 K. Specifically, for the S_0 state, the MD results for the standard deviation of ΔE_{abs} is 2.29 kJ/mol at 350 K. The corresponding results for the S_1 state, i.e., ΔE_{ems}, is 1.48 kJ/mol. For comparison, the standard deviations of ΔE_{abs} in at higher temperatures 400 K, 450 K and 500 K are much

smaller, viz., 0.73, 0.41, and 0.22 kJ/mol, respectively. For other ILs, the standard deviations for ΔE_{abs} at 350 K are 1.50 and 0.28 kJ/mol in $EMI^+PF_6^-$ and $EMI^+Tf_2N^-$, respectively. Thus the standard deviation for the $BMI^+PF_6^-$ is considerably larger at 350K than that at other temperatures and for other ionic liquids. This is ascribed to high viscosity of $BMI^+PF_6^-$, compared to the other two ILs we studied. (The viscosities of $BMI^+PF_6^-$, $EMI^+PF_6^-$, and $EMI^+Tf_2N^-$ are 28.8 mPa s, 18.6 mPa s, and 8.7 mPa s at 350 K, respectively.[105,106]) Therefore the $BMI^+PF_6^-$ system at 350 K is more likely to be trapped in local minima than at higher temperatures or other IL systems. Nonetheless, in view of the agreement with the other two ILs on the *T*-trend of Stokes shifts, our MD statistics employed for $BMI^+PF_6^-$ appear to be reasonable.

The Stokes shift of the solute with the more polar S_1 and less polar S_0 states decreases as *T* increases in all six systems we studied. This indicates that the effective polarity of ILs measured as their solvating power decreases with increasing *T*. The trend obtained here, though at variance with the results of ref 91, agrees with the behavior of dielectric constants observed in simulations[88] and experiments[74,75,76] as well as with the Stokes shift results for $T > 280$ K.[92]

For additional insight, we consider dipole solvation in a dielectric continuum. If the effect of solute polarizability is neglected, the solvent dependence of Stokes shift is given by the well-known Lippert-Mataga relation[89,90,107]

$$\langle \Delta\Delta E \rangle = 6\left[\frac{(\varepsilon_0 - n^2)}{(2n^2-1)(2\varepsilon_0+1)}\frac{1}{a^3}\right](\vec{\mu}_{ES} - \vec{\mu}_{GS})^2 \tag{2.4}$$

where μ_{ES} and μ_{GS} are the solute dipole moments of the excited and ground states, ε_0 and n are the static dielectric constant and index of refraction of the solvent, and a is the cavity size. Although this equation may not apply to ILs in a strict sense due to their ionic nature,

it can be used to make qualitative observations. Since nonpolarizable solvent descriptions are used in the present study, viz., $n = 1$, Eq. 2.4 becomes

$$\langle \Delta\Delta E \rangle = 6 \left[\frac{(\varepsilon_0 - 1)}{(2\varepsilon_0 + 1)} \frac{1}{a^3} \right] (\vec{\mu}_{ES} - \vec{\mu}_{GS})^2 \tag{2.5}$$

Therefore, for the systems studied in this paper, the Stokes shift $\langle \Delta\Delta E \rangle_{solv}$ depends only on the static dielectric constant ε_0; i.e., it is a monotonically increasing function of ε_0. According to a recent MD study,[88] the static dielectric constant of $BMI^+PF_6^-$ decreases with increasing *T*. As a result, the continuum model predicts that the Stokes shift would decrease with *T*. For real solvents which are polarizable (i.e., $n > 1$), one also needs to take into account variations of *n* and *a* as *T* grows. The cavity size *a* generally increases[108] but *n* decreases with *T*. According to a theoretical analysis in ref 109, proper inclusion of *n* and *a* in the continuum description yields the decreasing solvent reorganization energy with increasing *T*. In the linear response regime, Stokes shift is given by twice the solvent reorganization energy.[57] Therefore the monotonically decreasing nature of the Stokes shift will not be affected by the inclusion of *n* and *a*. Though qualitative, this is in agreement with simulation results.

Next we consider the temperature dependence of solvation structure, and how the change in Stokes shift is related to solvation structure.

2.3.2. Solvation Structures

MD results for the radial distribution functions (RDFs) for the cations and anions around the solute are shown in Figures 2.3 (for the diatomic solute) and 2.4 (for coumarin 153). The center of mass of cations, anions, and solutes are employed to represent their locations.

One general feature of RDFs regardless of the solute model or charge distribution is that as *T* increases, both cations and anions become less structured around the solute. The increase in thermal fluctuations and thus structural fluctuations reduces the average solvation structure of the solute as expected. The position of the first peak or shoulder structure around the diatomic solute tends to shift to slightly larger *r* values (*r* = solute-to-solvent distance) with the exception of the cation distribution around NP in $BMI^+PF_6^-$ in Figure 4(e). This could be due to the size of the BMI^+ ions and the packing of PF_6^- ions around the solute. At 350 K, PF_6^- ions in the first solvation shell prevent BMI^+ ions from approaching the solute. At higher temperature, PF_6^- ions are less structured and less dense around the solute, therefore BMI^+ ions can approach the solute. For the other two ILs, this is not observed, because EMI^+ is smaller than BMI^+ (and Tf_2N^- is bigger than PF_6^-). Coumarin 153 exhibits a similar trend, i.e., reduction in the solvation structure and increase in the peak position with rising *T* (Figure 2.4). This suggests that solvation structure becomes somewhat looser as *T* increases. This is in line with the aforementioned cavity size increase with *T*.

Comparison of the NP and IP results of the diatomic solute in Figure 2.3 shows that RDF peak heights for the latter are considerably higher than those for the former. Also the *r* values of the peak positions for IP are smaller than those for NP. This is due to the strong Coulomb interactions of IP with the IL ions, which in turn increase the local IL density near IP, compared to NP. Such an enhancement in solvent density in the region of a large electric field is referred to as electrostriction. Since the electrostriction effect and the resulting solvent density around IP decrease with *T*, solvation stabilization of the IP state

with respect to NP also decreases. This is responsible for the increase in ΔE_{ems} and thus in Stokes shift with increasing T as ΔE_{abs} remains essentially unaffected (Figure 2.1).

Turning to coumarin 153, we notice that its solvation structure is much more complicated than the diatomic solute. Coumarin 153 is larger and has a more complex shape than diatomic solute. As a result, the solvation structure for coumarin 153 is not as orderly as that for diatomic solute. Furthermore, RDFs for its S_0 and S_1 states show similar characteristics, especially in peak positions, in contrast to the diatomic solute case. This is because both S_0 and S_1 states of coumarin 153 are dipolar and their dipole moment difference (7.35D) is not as big as the difference for the diatomic solute (16.8D). Another difference from the diatomic solute is the relative locations of the IL cations and anions. In the case of the diatomic solute, the first peak of the anion center-of-mass is higher, sharper and closer to the solute, especially in the IP state, than that of the cation center-of-mass. For coumarin 153, on the other hand, the center of mass of the cations are closer to the solute except for the S_0 state in $EMI^+Tf_2N^-$. For $EMI^+Tf_2N^-$, the center of mass of the closest anions and cations are roughly the same distance away from the solute.

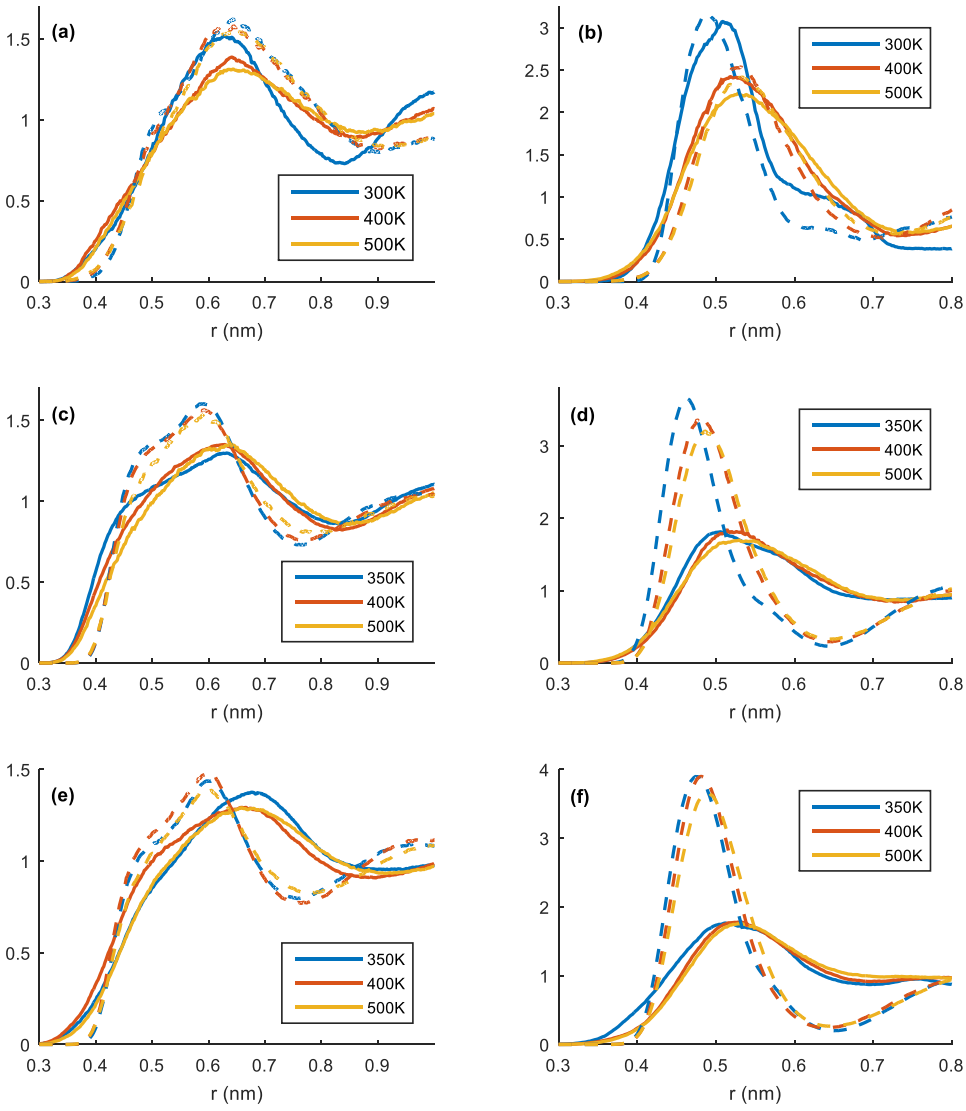

Figure 2.3. RDFs of cations (–) and anions (- -) around the diatomic solute: (a) NP in $EMI^+Tf_2N^-$, (b) IP in $EMI^+Tf_2N^-$, (c) NP in EMI^+ PF_6^-, (d) IP in $EMI^+PF_6^-$, (e) NP in $BMI^+PF_6^-$, and (f) IP in $BMI^+PF_6^-$. The center of mass is used to represent solute and ion positions.

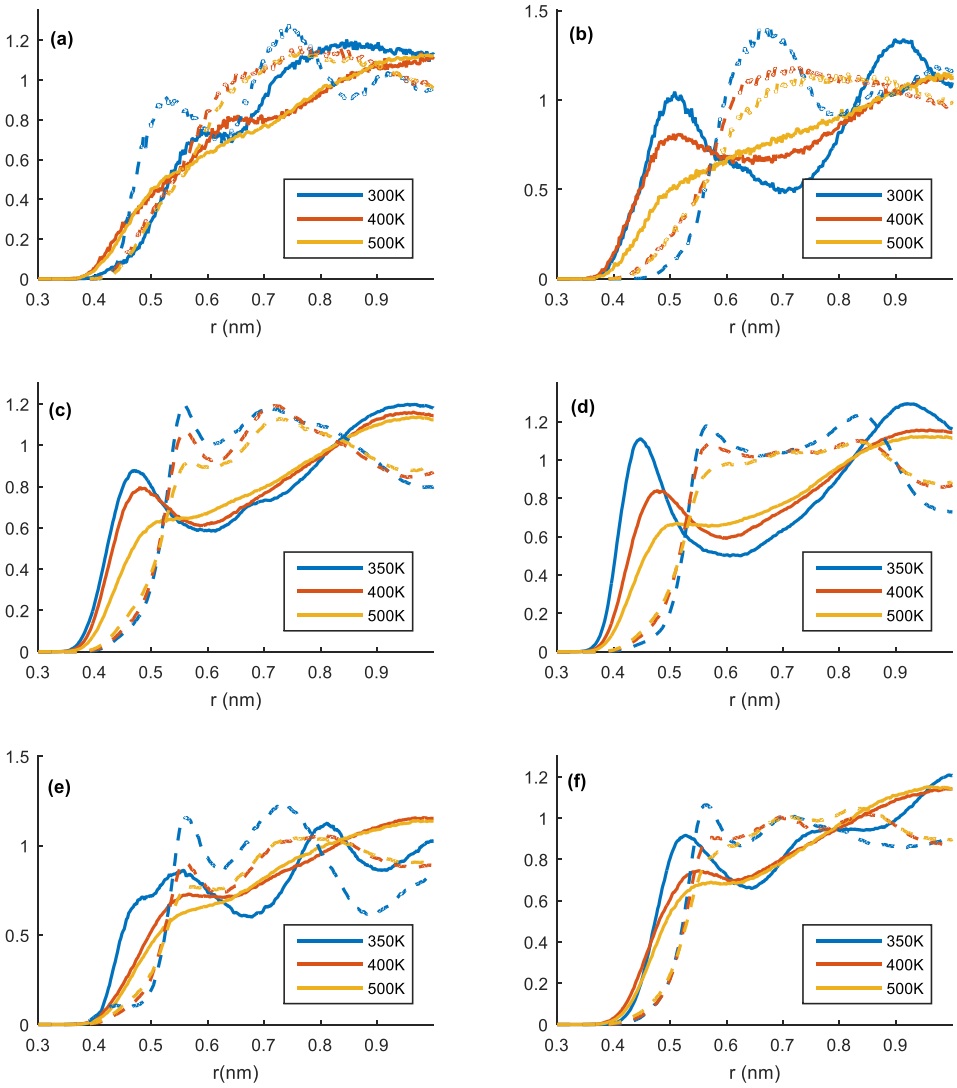

Figure 2.4. RDFs of cations (–) and anions (- -) around coumarin 153: (a) S_0 in $EMI^+Tf_2N^-$, (b) S_1 in $EMI^+Tf_2N^-$, (c) S_0 in EMI^+ PF_6^-, (d) S_1 in $EMI^+PF_6^-$, (e) S_0 in $BMI^+PF_6^-$, and (f) S_1 in $BMI^+PF_6^-$. The center of mass is used to represent solute and ion positions.

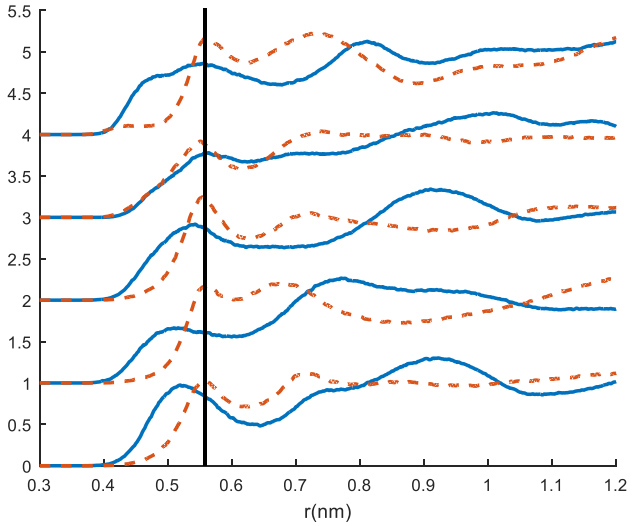

Figure 2.5. RDFs of BMI^+ (–) and PF_6^- (- -) around coumarin 153 in the S_0 state at 350K for 5 individual trajectories. The vertical line marks the average location of the first peak of PF_6^-.

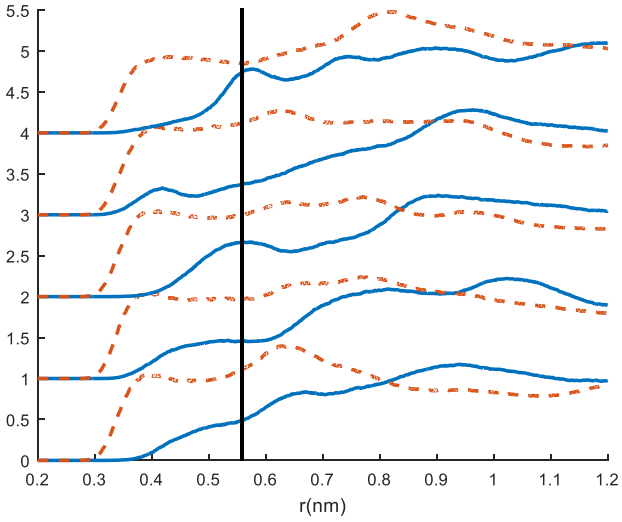

Figure 2.6. RDFs of C2 carbon of the imidazolium ring (–) and the terminal carbon of the butyl chain (- -) around coumarin153 in the S_0 state at 350 K for the five trajectories in Figure 2.5. The vertical line marks the average location of the first peak of the PF_6^-.

In the above discussion, a large standard deviation observed for ΔE_{abs} and ΔE_{ems} for coumarin 153 in $BMI^{+}PF_6^{-}$ at 350 K was attributed to potential trapping of the system in local energy minima. For additional insight, RDFs around coumarin 153 in the S_0 state, determined from individual trajectories at 350K, are compared in Figure 2.5. While the anion distribution, in particular, main peak position, does not vary significantly, the cation RDF shows significant variations. For example, the location of the first cation peak varies by 0.10 nm from 0.45 nm to 0.55 nm among five different trajectories we simulated. In four of the trajectories, the cations are closer to the solute than the anions; in other trajectory, the anions and the cations are at the same distance from the solute. A further analysis presented in Figure 2.6 indicates the large variation in cationic structure is caused mainly by the location of the imidazolium ring of cations. While the RDF of the terminal carbon of the alkyl chain is similar for all five trajectories considered there, a pronounced variation is observed for the RDF of the C2 carbon on the imidazolium ring, where C2 is the carbon atom directly bonded to two nitrogen atoms of the ring (see Scheme 2.1). In all five trajectories considered in Figure 2.6, the terminal carbon of the alkyl chain is closer to the solute than the average center-of-mass location of the anions. By contrast, the C2 carbon position relative to the anion location varies rather significantly with the trajectories. While the variations of ΔE_{abs} are not directly related to the variations of the first peak location of cations according to our analysis, this example nonetheless shows that proper sampling effected via multiple MD trajectories of long duration is needed to accurately capture properties of ILs at room temperature, especially those with high viscosity.

2.3.3. Solvation Dynamics

Here we consider solvation dynamics. The results for equilibrium solvation dynamics *C(t)* (Eq. 2.1) are presented in Figures 2.7 and 2.8. Regardless of the solute model or *T*, *C(t)* shows bi-phasic relaxation, viz., short-time inertial dynamics in the sub-picosecond time scale, followed by long-time non-exponential decay.[57,58,59,69,110–118] The solvent frequency ω_s (Eq. 2.3), which characterizes the inertial solvation dynamics occurring primarily via hindered ion translations of librational character,[57,58] varies little with temperature for both the diatomic solute and coumarin 153 (Tables 2.3 and 2.4). In ref 88, this behavior was attributed to the potential of mean force (PMF) *w(r)* (= $-k_BT\ ln\ g(r)$) that does not vary significantly with *T* because reduction in solvation structure is relatively mild (see sec 3B above). The weak temperature dependence of ω_s was also briefly discussed in ref 119. In the case of the diatomic solute, ω_s for the IP state is considerably higher than that for NP. As discussed above, solvent structure around IP is more pronounced than that around NP due to electrostriction. This leads to tighter PMF associated with the first solvation shell and thus a higher solvent frequency for the IP state than for NP.[58] Though lesser in degree, coumarin 153 shows the same trend; ω_s for the more dipolar S_1 state is higher than that for the less dipolar S_0.

Table 2.4. ω_s, τ, β, and τ_s for diatomic solute in $EMI^+Tf_2N^-$, $EMI^+PF_6^-$, and $BMI^+PF_6^-$.

	NP				IP			
	ω_s (1/ps)	τ (ps)	β	τ_s (ps)	ω_s (1/ps)	τ (ps)	β	τ_s (ps)
$EMI^+Tf_2N^-$								
300	23.14	31.32	0.48	32.54	29.61	680.7	0.58	499.2
350	22.29	1.78	0.42	4.37	29.43	45.23	0.42	74.92
400	22.96	1.34	0.48	2.28	29.32	14.16	0.43	23.10
450	22.60	0.60	0.47	1.37	29.16	7.71	0.47	11.31
500	22.44	0.21	0.43	0.93	28.94	4.75	0.53	4.87
$EMI^+PF_6^-$								
350	22.91	8.41	0.49	7.81	32.14	180.2	0.33	428.8
400	22.88	3.80	0.59	2.33	31.37	30.76	0.36	53.65
450	22.56	0.95	0.50	1.22	30.98	11.14	0.45	10.18
500	22.45	0.81	0.57	0.81	30.64	5.25	0.47	4.59
$BMI^+PF_6^-$								
350	21.13	5.72	0.43	9.36	31.17	534.8	0.67	250.3
400	21.38	3.91	0.52	3.96	30.87	44.55	0.36	92.30
450	20.86	0.90	0.48	1.43	30.47	13.87	0.46	13.57
500	20.70	0.98	0.63	0.88	30.04	5.46	0.45	6.10

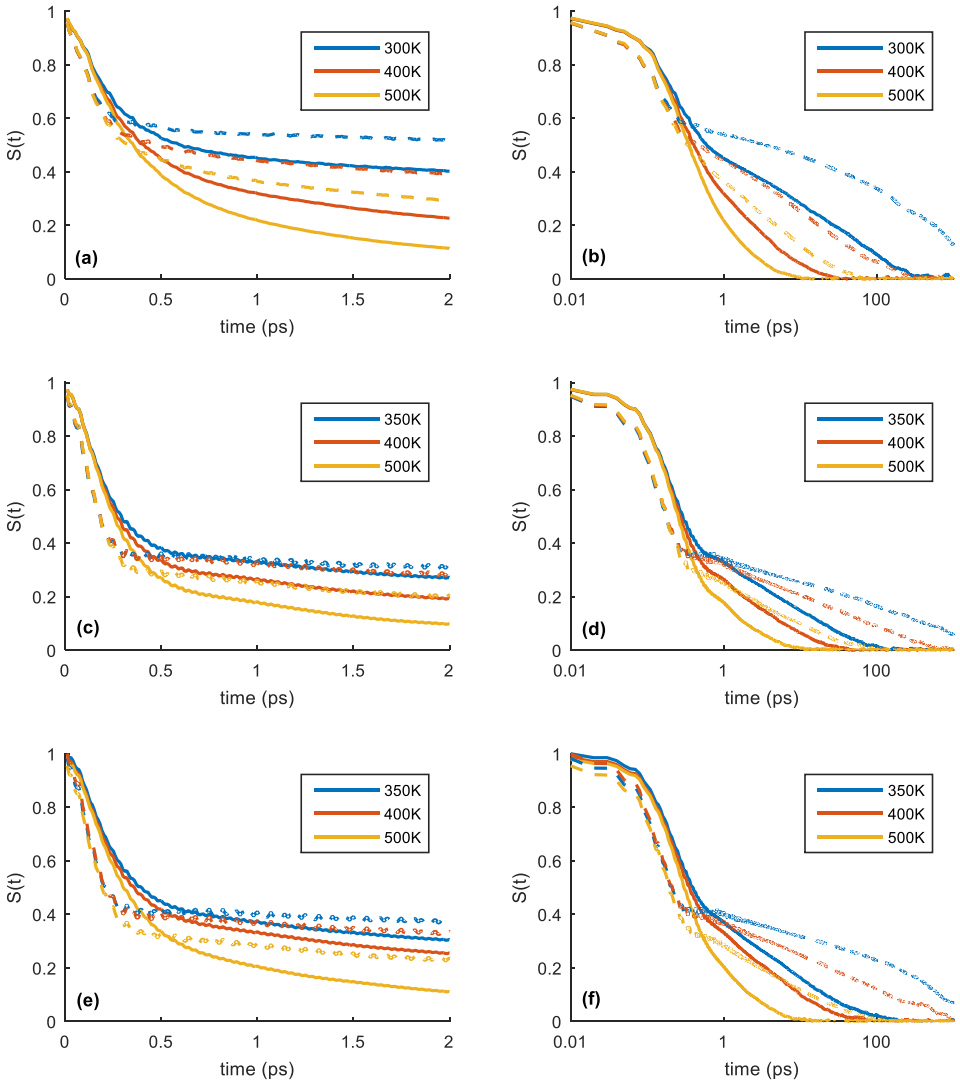

Figure 2.7. $C(t)$ for diatomic solute NP (–) and IP (- -) in $EMI^{+}Tf_2N^{-}$ in (a) and (b), $EMI^{+}PF_6^{-}$ in (c) and (d), and $BMI^{+}PF_6^{-}$ in (e) and (f).

Table 2.5. ω_s, τ, β, and τ_s for coumarin 153 in $EMI^+Tf_2N^-$, $EMI^+PF_6^-$, and $BMI^+PF_6^-$

	S_0				S_1			
	ω_s (1/ps)	τ (ps)	β	τ_s (ps)	ω_s (1/ps)	τ (ps)	β	τ_s (ps)
$EMI^+Tf_2N^-$								
300	32.46	193.1	0.51	184.1	33.45	391.1	0.49	369.4
350	32.12	33.39	0.45	51.59	33.57	13.62	0.36	42.23
400	33.09	6.74	0.43	11.78	33.48	6.65	0.39	14.62
450	32.93	1.45	0.34	7.61	33.44	3.36	0.42	6.94
500	33.26	1.92	0.46	3.24	33.50	1.96	0.45	3.46
$EMI^+PF_6^-$								
350	31.53	226.6	0.48	177.4	34.67	144.1	0.40	151.3
400	31.14	41.72	0.46	41.64	32.79	70.94	0.57	34.13
450	31.08	11.84	0.50	10.50	33.40	12.77	0.53	9.04
500	31.66	4.48	0.51	3.98	33.21	9.79	0.65	3.65
$BMI^+PF_6^-$								
350	31.76	389.9	0.65	198.6	33.14	454.3	0.60	251.2
400	30.56	56.82	0.56	43.70	33.10	40.46	0.54	29.93
450	30.79	13.18	0.47	15.93	32.72	9.54	0.43	12.79
500	31.11	8.13	0.62	5.32	32.59	6.61	0.53	5.57

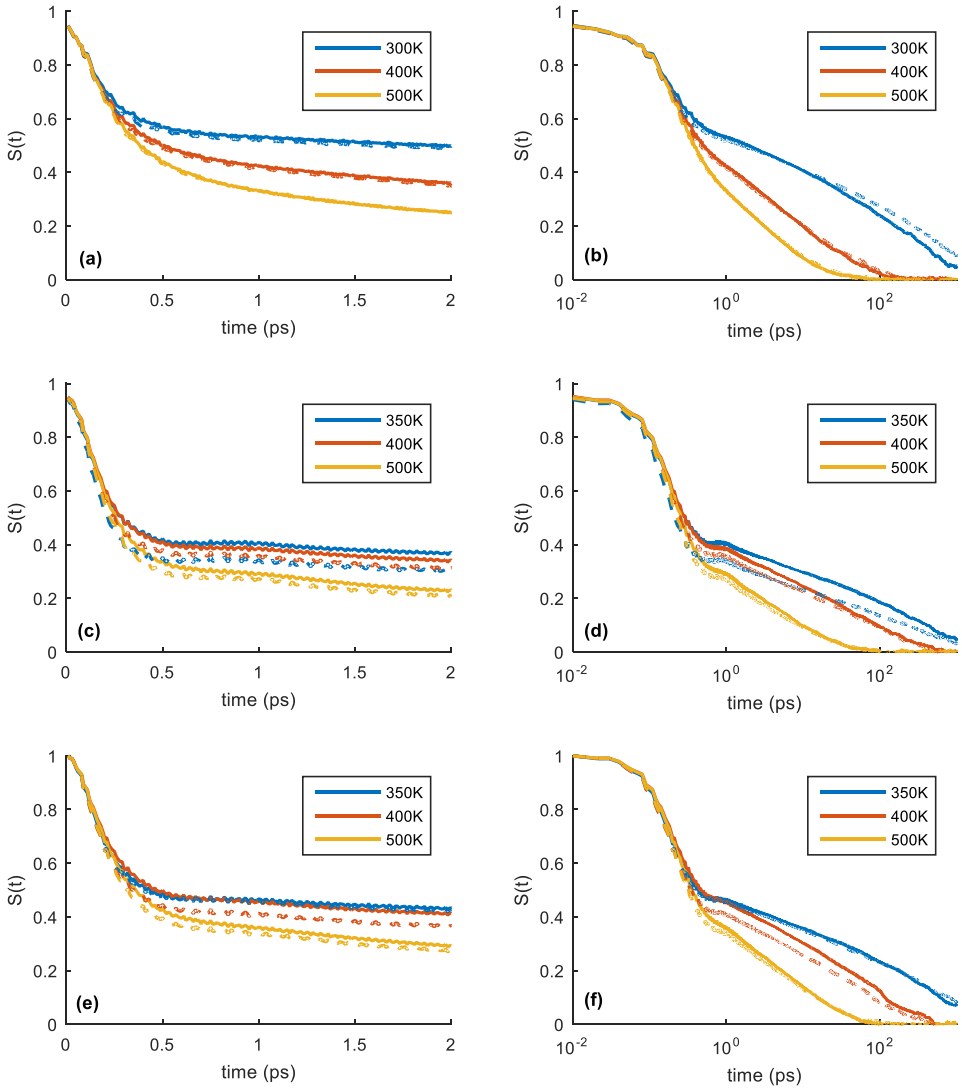

Figure 2.8. $C(t)$ for coumarin 153 S_0 (–) and S_1 (- -) in $EMI^+Tf_2N^-$ in (a) and (b), $EMI^+PF_6^-$ in (c) and (d), and $BMI^+PF_6^-$ in (e) and (f).

In contrast to sub-picosecond inertial dynamics, long-time dissipative dynamics show strong temperature dependence. Specifically, long-time solvation dynamics become accelerated with T as the time scale τ of their stretched exponential decay becomes shorter. The other parameter β that characterizes the degree of heterogeneity in the relaxation dynamics mostly falls between 0.4 to 0.6, though it varies from as low as 0.2 to as high as

0.9. Based on the current simulation results, however, it would be difficult to conclude whether β has any temperature dependence. Significantly improved MD statistics through more and longer simulations will be needed to draw a definite conclusion on this issue.

One direct consequence of the *T*-dependent dissipative dynamics is that the solvation time τ_s (Eq 2.2) decreases with increasing *T*.[103,110] In the case of the diatomic solute, τ_s for NP is much shorter than that for IP. In ref 58, this was attributed to rugged solvation structure of the latter; as noted above, RDF is more structured for IP than NP. This yields high barriers for solvent transport on the PMF surface in the presence of IP, compared to NP. Interestingly, this trend of τ_s is not shared by coumarin 153. Since the RDF peak heights for its S_0 and S_1 states are comparable, especially in $EMI^+PF_6^-$ and $BMI^+PF_6^-$ (Figure 5), we would expect that the time scale for barrier crossing dynamics on the PMF surface would not differ significantly between the two.

For further insight into dissipative solvation dynamics, we investigate how the viscosity and solvation time are related. The temperature dependence of viscosity η of ILs can be described by the Vogel-Fulcher-Tamman (VFT) equation[105,106]

$$\eta = AT^{0.5} \exp\left(\frac{k}{T - T_0}\right) \tag{2.6}$$

where $A, k,$ and T_0 are the fitting parameters. Using the parameters from Refs 105 and 106, the viscosity of the three ILs studied are calculated and plotted against the solvation time for the two different solutes in the ground and excited states in Figure 10. The results show that there is a strong correlation between solvation time and viscosity irrespective of the IL species; solvation time increases with the IL viscosity. The coefficients of determination (R^2) for the linear ln τ_s-ln η relationship are 0.86, 0.89, 0.92, and 0.93 for NP, IP, S_0, and S_1, respectively. Since the subpicosecond component of solvation dynamics varies little

with temperature, the T-dependence of τ_s is governed essentially by their long time component. The strong correlation between τ_s and η indicates that viscosity plays a major role in slow dissipative solvation dynamics.

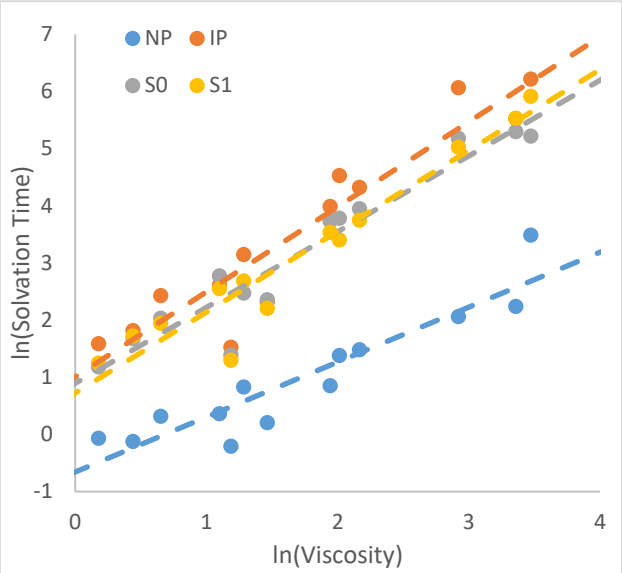

Figure 2.9. ln τ_s (ps) versus ln η (mPa s) for all three ILs.

In view of the results in Figure 2.9, we consider the Arrhenius equation for the temperature variation of the solvation time

$$\frac{1}{\tau_s} = \frac{1}{\tau_{s,\infty}} \exp\left(\frac{-E_a}{RT}\right) \tag{2.7}$$

The results for activation energy, E_a, are compiled in Table 2.6. The coefficients of determination for the fitting of the Arrhenius equation are above 0.95 for all 12 cases we studied, i.e., four solute electronic states in three different ILs.

Table 2.6. Activation energy (kJ/mol) for solvation time for the diatomic solute and coumarin 153 in $EMI^+Tf_2N^-$, $EMI^+PF_6^-$, and $BMI^+PF_6^-$

	NP	IP	S_0	S_1
$EMI^+Tf_2N^-$	21.4	28.3	25.2	28.5
$EMI^+PF_6^-$	22.0	44.9	37.2	36.5
$BMI^+PF_6^-$	23.6	37.8	34.5	36.3
Average	22.4	37.0	32.3	33.8

Among the four solute electronic states, IP has the highest activation energy for solvation time, while the S_0 and S_1 states are characterized by similar E_a values. As mentioned earlier, the IP state shows the most pronounced solvation shell structure and therefore its relaxation—which governs long-time dissipative dynamics[58]—has the highest E_a. The S_0 and S_1 states on the other hand have similar solvation shell structure and thus comparable E_a.

For a given electronic state, $EMI^+PF_6^-$ and $BMI^+PF_6^-$ yield similar activation energies for τ_s due to their comparable solvation structure. Additionally, their E_a value is larger than that of $EMI^+Tf_2N^-$. This is ascribed to a more compact solvation structure in $EMI^+PF_6^-$ and $BMI^+PF_6^-$ than in $EMI^+Tf_2N^-$.

2.4. Conclusion

In this article, we have studied solvation of a simple diatomic model solute and realistic coumarin 153 in ionic liquids, $EMI^+Tf_2N^-$, $EMI^+PF_6^-$, and $BMI^+PF_6^-$, in the temperature range 350 K $\leq T \leq$ 500 K using MD simulations. For both solutes, the S_1 state

is more dipolar than the S_0 state. It was found that as *T* increases, the Stokes shift decreases. In the case of the diatomic solute, the Stokes shift shows a fairly linear behavior in *T* in all three ionic liquids we studied. The trend in Stokes shift indicates that the effective polarity of ionic liquids decreases with increasing *T*. This finding is in agreement with the MD[88] and experimental[74,75,76] results for the static dielectric constant of ILs though care should be taken in relating the empirical polarity to static dielectric constant for ILs.

The influence of temperature on equilibrium solvation dynamics was also studied. As *T* increases, their long-time dissipative relaxation becomes faster, while sub-picosecond inertial dynamics remain nearly unchanged. The latter trend was attributed to the weak temperature dependence of the solvation structure of the solute and thus its PMF. For the diatomic solute, the solvation time, τ_s, and its activation energy, E_a, were found to be much smaller for the non-dipolar NP state than for the highly dipolar IP state. This is attributed to the pronounced difference in solvation structure between NP and IP; RDF peaks are considerably higher for IP than for NP. By contrast, the S_0 and S_1 states of coumarin 153 are characterized by similar RDF peak heights and thus comparable solvation time and activation energy.

References

55. Chakrabarty, D.; Hazra, P.; Chakraborty, A.; Seth, D.; Sarkar, N. Dynamics of Solvent Relaxation in Room Temperature Ionic Liquids. *Chem. Phys. Letter* **2003**, *381*, 697-704.
56. Zhang, X.; Liang, M.; Ernsting, N. P.; Maroncelli, M. Complete Solvation Response of Coumarin 153 in Ionic Liquids. *J. Phys. Chem. B* **2013**, *117*, 4291-4304.
57. Shim, Y.; Duan, J.; Choi, M. Y.; Kim, H. J. Solvation in Molecular Ionic Liquids. *J. Chem. Phys.* **2003,** *119*, 6411-6414.

58. Shim, Y.; Choi, M. Y.; Kim, H. J. A Molecular Dynamics Computer Simulation Study of Room-Temperature Ionic Liquids. II. Equilibrium and Nonequilibrium Solvation Dynamics. *J. Chem. Phys.* **2005,** *122*, 044511.
59. Kobrak, M. N. Characterization of the Solvation Dynamics of an Ionic Liquid via Molecular Dynamics Simulation. *J. Chem. Phys.* **2006,** *125*, 064502.
60. Schmollngruber, M.; Schröder, C.; Steinhauser, O. Polarization Effects on the Solvation Dynamics of Coumarin C153 in Ionic Liquids: Components and Their Cross-Correlations. *J. Chem. Phys.* **2013,** *138*, 204504.
61. Daschakraborty, S.; Biswas, R. Ultrafast Solvation Response in Room Temperature Ionic Liquids: Possible Origin and Importance of the Collective and the Nearest Neighbour Solvent Modes. *J. Chem. Phys.* **2012,** *137*, 114501.
62. Giraud, G.; Gordon. C. M.; Dunkin, I. R.; Wynne, K., The effects of anion and cation substitution on the ultrafast solvent dynamics of ionic liquids: A time-resolved optical Kerr-effect spectroscopic study. *J. Chem. Phys*. **2003**, *119*, 464-477.
63. Rajian, J. R.; Li, S.; Bartsch, R. A.; Quitevis, E. L. Temperature-Dependence of the Low-Frequency Spectrum of 1-Pentyl-3-Methylimidazolium Bis(trifluoromethanesulfonyl)-imide Studied by Optical Kerr Effect Spectroscopy. *Chem. Phys. Lett.* **2004**, *393*, 372-377.
64. Shirota, H.; Castner, E. W., Jr. Physical Properties and Intermolecular Dynamics of an Ionic Liquid Compared with Its Isoelectronic Neutral Binary Solution. *J. Phys. Chem. A* **2005**, *109*, 9388-9392.
65. Shirota, H.; Castner, E. W., Jr. Why Are Viscosities Lower for Ionic Liquids with –CH2Si(CH3)3 vs –CH2C(CH3)3 Substitutions on the Imidazolium Cations? *J. Phys. Chem. B* **2005**, *109*, 21576-21585.
66. Hu, Z.; Huang, X.; Annapureddy, H. V. R.; Margulis, C. J. J. Molecular Dynamics Study of the Temperature-Dependent Optical Kerr Effect Spectra and Intermolecular Dynamics of Room Temperature Ionic Liquid 1-Methoxyethylpyridinium Dicyanamide. *J. Phys. Chem. B* **2008**, *112*, 7837-7849.
67. Stoppa, A.; Hunger, J.; Buchner, R.; Hefter, G.; Thoman, A.; Helm, H. Interactions and Dynamics in Ionic Liquids. *J. Phys. Chem. B* **2008**, *112*, 4854-4858.
68. Yamamoto, K.; Tani, M.; Hangyo, M. Terahertz Time-Domain Spectroscopy of Imidazolium Ionic Liquids. *J. Phys. Chem. B* **2007**, *111*, 4854-4859.
69. Roy, D.; Maroncelli, M. Simulations of Solvation and Solvation Dynamics in an Idealized Ionic Liquid Model. *J. Phys. Chem. B* **2012,** *116*, 5951-5970.
70. Hynes, J.T. *In The Theory of Chemical Reaction Dynamics*; Baer, M., Ed.; Chemical Rubber: Boca Raton, 1985.
71. Kosower, E. M. *An Introduction to Physical Organic Chemistry;* Wiley: New York, 1968.
72. Reichardt, C. *Solvents and Solvent Effects in Organic Chemistry*, 2nd ed.; VCH: Weinheim, 1988.
73. Reichardt, C. Solvatochromic Dyes as Solvent Polarity Indicators. *Chem. Rev*. **1994**, *94*, 2319-2358.
74. Mizoshiri, M.; Nagao, T.; Mizoguchi, Y.; Yao, M. Dielectric Permittivity of Room Temperature Ionic Liquids: A Relation to the Polar and Nonpolar Domain Structures. *J. Chem. Phys.* **2010**, *132*, 164510.

75. Hunger, J.; Stoppa, A.; Schrödle, S.; Hefter, G.; Buchner, R. Temperature Dependence of the Dielectric Properties and Dynamics of Ionic Liquids. *ChemPhysChem.* **2009**, *10*, 723-733.
76. Krossing, I.; Slattery, J. M.; Daguenet, C.; Dyson, P. J.; Oleinikova, A.; Weingärtner, H. Why Are Ionic Liquids Liquid? A Simple Explanation Based on Lattice and Solvation Energies. *J. Am. Chem. Soc.* **2006**, *128*, 13427-13434.
77. Carmichael, A. J.; Seddon, K. R. Polarity Study of Some 1-Alkyl-3-Methylimidazolium Ambient-Temperature Ionic Liquids with the Solvatochromic Dye, Nile Red. *J. Phys. Org. Chem.* **2000**, *13*, 591-595.
78. Aki, S. N. V. K.; Brennecke, J. F.; Samanta, A. How Polar are Room-Temperature Ionic Liquids? *Chem. Commun.* **2001**, 413-414.
79. Muldoon, M. J.; Gordon, C. M.; Dunkin, I. R. Investigations of Solvent-Solute Interactions in Room Temperature Ionic Liquids Using Solvatochromic Dyes. *J. Chem. Soc., Perkin Trans. 2* **2001,** 433-435.
80. Baker, S. N.; Baker, G. A.; Bright, F. V. Temperature-Dependent Microscopic Solvent Properties of 'Dry' and 'Wet' 1-Butyl-3-Methylimidazolium Hexafluorophosphate: Correlation with ET(30) and Kamlet-Taft Polarity Scales. *Green Chem.* **2002**, *4*, 165-169.
81. Fletcher, K. A.; Storey, I. K.; Hendricks, A. E.; Pandey, S.; Pandey, S. Behavior of the Solvatochromic Probes Reichardt's Dye, Pyrene, Dansylamide, Nile Red and 1-Pyrenecarbaldehyde within the Room-Temperature Ionic Liquid BmimPF6. *Green Chem.* **2001**, *3*, 210-215.
82. Karmakar, R.; Samanta, A. Solvation Dynamics of Coumarin-153 in a Room-Temperature Ionic Liquid. *J. Phys. Chem. A* **2002**, *106*, 4447-4452.
83. Lu, J.; Liott, C. L.; Eckert, C. A. Spectroscopically Probing Microscopic Solvent Properties of Room-Temperature Ionic Liquids with the Addition of Carbon Dioxide. *J. Phys. Chem. A* **2003**, *107*, 3995-4000.
84. Reichardt, C. Polarity of Ionic Liquids Determined Empirically by Means of Solvatochromic Pyridinium N-Phenolate Betaine Dyes. *Green Chem.* **2005**, *7*, 339-351.
85. Shim, Y.; Kim, H. J. MD Study of Solvation in the Mixture of a Room-Temperature Ionic Liquid and CO2. *J. Phys. Chem. B* **2010,** *114*, 10160-10170.
86. Shim, Y.; Jeong, D.; Manjari, S. R.; Choi, M. Y.; Kim, H. J. Solvation, Solute Rotation and Vibration Relaxation, and Electron-Transfer Reactions in Room-Temperature Ionic Liquids. *Acc. Chem. Res.* **2007**, *40*, 1130-1137.
87. Kashyap, H.; Biswas, R. Solvation Dynamics of Dipolar Probes in Dipolar Room Temperature Ionic Liquids: Separation of Ion-Dipole and Dipole-Dipole Interaction Contributions. *J. Phys. Chem. B* **2010,** *114*, 254-268.
88. Shim, Y.; Kim, H. J. Dielectric Relaxation and Solvation Dynamics in a Room-Temperature Ionic Liquid: Temperature Dependence. *J. Phys. Chem. B* **2013**, *117*, 11743-11752.
89. Lippert E. Z. The Solvent Effect on the Spectral Shift. *Zeitschrift für Naturforschung A* **1955**, 541-545.
90. Mataga, N.; Kaifu, Y.; Koizumi, M. The Solvent Effect on Fluorescence Spectrum, Change of Solute-Solvent Interaction During the Lifetime of Excited Solute Molecule. *Bulletin of the Chemical Society of Japan* **1955**, *28*, 690-691.

91. Kashyap, H. K.; Biswas, R. Stokes Shift Dynamics in Ionic Liquids: Temperature Dependence. *J. Phys. Chem.* **2010,** *114*, 16811-16823.
92. Nagasawa, Y.; Oishi, A.; Itoh, T.; Yasuda, M.; Muramatsu, M.; Ishibashi, Y.; Ito, S.; Miyasaka, H. Dynamic Stokes Shift of 9, 9′-Bianthryl in Ionic Liquids : A Temperature Dependence Study. *J. Phys. Chem. C* **2009,** *113*, 11868-11876.
93. Zhang, S.; Sun, N.; He, X.; Lu, X.; Zhang, X. Physical Properties of Ionic Liquids: Database and Evaluation. *J. Phys. Chem. Ref. Data.* **2006,** *35*, 1475–1517
94. Jorgensen, W. L.; Maxwell, D. S.; Tirado-Rives, J. Development and Testing of the OPLS All-Atom Force Field on Conformational Energetics and Properties of Organic Liquids. *J. Am. Chem. Soc.* **1996,** *118*, 11225-11236.
95. Li, H.; Arzhantsev, S.; Maroncelli, M. Solvation and Solvatochromism in CO2-Expanded Liquids. 2. Experiment-Simulation Comparisons of Preferential Solvation in Three Prototypical Mixtures. *J. Phys. Chem. B* **2007,** *111*, 3208-3221.
96. Canongia Lopes, J. N.; Deschamps, J.; Pádua, A. A. H. Modeling Ionic Liquids Using a Systematic All-Atom Force Field. *J. Phys. Chem. B* **2004**, *108*, 2038-2047.
97. Canongia Lopes, J. N.; Deschamps, J.; Pádua, A. A. H. Modeling Ionic Liquids Using a Systematic All-Atom Force Field. *J. Phys. Chem. B* **2004**, *108*, 11250.
98. Lopes, J. N. C.; Padua, A. A. H. Molecular Force Field for Ionic Liquids Composed of Triflate or Bistriflylimide Anions. *J. Phys. Chem. B* **2004,** *108*, 16893-16898.
99. Kaminski, G. A.; Jorgensen, W. L. Host–guest Chemistry of Rotaxanes and Catenanes: Application of a Polarizable All-Atom Force Field to Cyclobis(paraquat-P-Phenylene) Complexes with Disubstituted Benzenes and Biphenyls. *J. Chem. Soc. Perkin Trans. 2* **1999,** 2365-2375.
100. Liu, Z. P.; Huang, S. P.; Wang, W. C. A Refined Force Field for Molecular Simulation of Imidazolium-Based Ionic Liquids. *J. Phys. Chem. B* **2004,** *108*, 12978-12989.
101. Pronk, S.; Páll, S.; Schulz, R.; Larsson, P.; Bjelkmar, P.; Apostolov, R.; Shirts, M. R.; Smith, J. C.; Kasson, P. M.; Van Der Spoel, D.; et al. GROMACS 4.5: A High-Throughput and Highly Parallel Open Source Molecular Simulation Toolkit. *Bioinformatics* **2013**, *29*, 845-854.
102. Warshel, A. Dynamics of Reactions in Polar Solvents. Semiclassical Trajectory Studies of Electron-Transfer and Proton-Transfer Reactions. *J. Phy. Chem.* **1982**, *86*, 2218-2224.
103. Ito, N.; Arzhantsev, S.; Heitz, M.; Maroncelli, M. Solvation Dynamics and Rotation of Coumarin 153 in Alkylphosphonium Ionic Liquids. *J. Phys. Chem. B* **2004**, *108*, 5771-5777.
104. Jin, H.; Baker, G. A.; Arzhantsev, S.; Dong, J.; Maroncelli, M. Solvation and Rotational Dynamics of Coumarin 153 in Ionic Liquids: Comparisons to Conventional Solvent. *J. Phys. Chem. B* **2007**, *111*, 7291-7302.
105. Jacquemin, J.; Husson, P.; Padua, A. A. H.; Majer, V. Density and Viscosity of Several Pure and Water-Saturated Ionic Liquids. *Green Chem.* **2006,** *8*, 172-180.
106. Seddon, K.R.; Stark, A.; Torres, M.-J. Clean Solvents; American Chemiscal Society:, Washington, DC, 2002.
107. Kim, H. J. Electronically Adiabatic Reaction Field Approach to Solvation. II. Solvent Effects on Electronic Spectra. *J. Chem. Phys.* **1996**, *105*, 6833.
108. Manjari, S. R.; Kim, H. J. On the Temperature and Pressure Dependences of Cavities in the Dielectric Continuum Picture. *J. Chem. Phys.* **2005**, 014504.

109. Manjari, S. R.; Kim, H. J. Temperature- and Pressure-Dependence of the Outer-Sphere Reorganization Free Energy for Electron Transfer Reactions: A Continuum Approach. *J. Phys. Chem. B* **2006**, *110*, 494-500.
110. Arzhantsev, S.; Ito, N.; Heitz, M.; Maroncelli, M. Solvation Dynamics of Coumarin 153 in Several Classes of Ionic Liquids: Cation Dependence of the Ultrafast Component. *Chem. Phys. Lett.* **2003**, *381*, 278-286.
111. Margulis, C. J. Computational Study of Imidazolium-Based Ionic Solvents with Alkyl Substituents of Different Lengths. *Mol. Phys.* **2004**, *102*, 829-838.
112. Kobrak, M. N.; Znamenskiy, V. Solvation Dynamics of Room-Temperature Ionic Liquids: Evidence for Collective Solvent Motion on Sub-Picosecond Timescales. *Chem. Phys. Lett.* **2004**, *395*, 127-132.
113. Bhargava, B .L.; Balasubramanian, S. J. Dynamics in a Room-Temperature Ionic Liquid: A Computer Simulation Study of 1,3-dimethylimidazolium Chloride. *J. Chem. Phys.* **2005**, *123*, 144505.
114. Hu, Z.; Margulis, C. J. Heterogeneity in a Room-Temperature Ionic Liquid: Persistent Local Environments and the Red-Edge Effect. *Proc. Natl. Acad. Sci. U.S.A.* **2006**, *103*, 831-836.
115. Kobrak, M. N. A Comparative Study of Solvation Dynamics in Room-Temperature Ionic Liquids. *J. Chem. Phys.* **2007**, *127*, 184507.
116. Jeong, D.; Shim, Y.; Choi, M. Y.; Kim, H. J. Effects of Solute Electronic Polarizability on Solvation in a Room-Temperature Ionic Liquid. *J. Phys. Chem. B* **2007**, *111*, 4920-4925.
117. Jeong, D.; Choi, M. Y.; Jung, Y.; Kim, H. J. 1/f Spectrum and Memory Function Analysis of Solvation Dynamics in a Room-Temperature Ionic Liquid. *J. Chem. Phys.* **2008**, *128*, 174504.
118. Huang, M.; Jiang, Y.; Sasisanker, P.; Driver, G. W.; Weingartner, H.J. Static Relative Dielectric Permittivities of Ionic Liquid at 25°. *J. Chem. Eng. Data* **2011**, *56*, 1494-1499.
119. Pal, T.; Biswas, R. Slow Solvation in Ionic Liquids: Connections to non-Gaussian Moves and Multi-Point Correlations. *J. Chem. Phys*. **2014**, *141*, 104501.

Chapter 3. Structural and Dynamical Heterogeneities in Ionic Liquids Revealed by MD Simulations and Single-Molecule Fluorescence*

3.1. Introduction

There are many classes of cations for ILs, but most can be described as nonpolar alkyl chains attached to different polar charged groups. Compton was first to hypothesized that ILs should not be regarded as a homogeneous solvent but as a liquid with polar and nonpolar regions.[120] Using molecular dynamics (MD) simulations, Voth and Wang demonstrated with a coarse-grained model that, for imidazolium ILs, the non-polar alkyl chains aggregate while the charged groups distribute uniformly throughout the liquid.[121] Lopes and Padua repeated the simulations with all-atom force field based on OPLS-AA. Their simulations showed that, for imidazolium with alkyl chains longer than or equal to butyl, aggregation of the alkyl chains is observed. The charged groups, on the other hand, form a network of ionic channels that is permeated by the nonpolar aggregates.[122,123] Margulis, using simulations, showed that the three peaks in the structure factor $S(q)$ of ILs can be assigned to alternating regions of polar/nonpolar groups (around 0.5 Å^{-1}), positive/negative charges (around 0.8 Å^{-1}), and adjacency correlations of atoms (around 1.5 Å^{-1}).[124] Lastly, Lopes and Padua calculated that the length scale of the polar/nonpolar regions ranges from 11 Å for [C_2mim][PF_6] to 20 Å for [C_{12}mim][PF_6].[123]

Experimentally, X-ray and neutron scattering techniques mirrored the results found in simulations in that the the first sharp diffraction peak was observed at $q = 0.2 - 0.5\ \text{Å}^{-1}$ for ILs.[125–130] Likewise, a second technique, FCS, was utilized to study the solvation

* Partially reprinted from *J. Phys. Chem. B*. Copyright 2017 American Chemical Society.

dynamics of a fluorescence probe. FCS is a single-molecule based technique that monitors the motions of fluorescence probe across a femtoliter focal volume using a confocal microscope.[131–138] Shaw and coworkers[139] and Patra and Samanta[140] both found bimodal diffusion behavior for various fluorescence probes in imidazolium and pyrrolidinium based ILs. Both attributed the bimodal diffusion behavior as diffusion in polar and nonpolar regions. This interpretation would imply that the fluorescence probes do not switch between these two regions while passing through the focal volume, a process that takes milliseconds. Given the length scale of the polar/nonpolar regions (10 ~ 20 Å) and the size of the fluorescence probes (5 ~ 10 Å), this would require that the molecules diffuse through a very narrow channel for a significantly long time. In contrast to this bimodal picture of local heterogeneity, neutron scattering[125,126,141] and simulations[142–146] have shown that ILs are glassy. In a glassy environment, the diffusion of probes is non-Gaussian, the mean square displacement (MSD) is best expressed as a power law,[146] and the intermediate scattering function exhibits a stretched exponential behavior. [125,126,141,144,145] Another indication of slowly-relaxing heterogeneity in IL solvation structures is the reported fluorescence red-edge effect in dye emission spectra.[142,143]

The goal of this work is to determine whether there is a correlation between the diffusion rate of a solvatochromic dye (Nile Red, NR Scheme 1)[147–150] and local polarity of its environment using MD simulations and spectroscopy. Such a connection would be expected if the polar/non-polar regions identified in refs. 121–124 have different local densities and if ILs behave as conventional solvents that follow the Stokes-Einstein relation. In contrast, if ILs are best described as glassy, there is decoupling of structural

relaxation and transport dynamics[144] and no simple correlation between polarity and diffusion is expected.

3.2. Experimental and Simulation Methods

3.2.1. Ionic Liquids

All ILs are purchased from Iolitec, USA. The ILs studied in this chapter were N-methyl-N-butylpyrrolidinium bis(trifluoromethylsulfonyl)imide [$Pyrr_{14}$] [Tf_2N^-], 1-ethyl-3-methylimidazolium bis(trifluoromethylsulfonyl)imide [Emim][Tf_2N^-], and 1-butyl-3-methylimidazolium bis(trifluoromethylsulfonyl)imide [Bmim][Tf_2N^-], (Scheme 3.1). Most experiments were performed with the pyrrolidinium ILs rather than the imidazolium ILs, because of their higher purity and the lack of absorption. As purchased, imidazolium ILs have absorption from UV to 500 nm which introduces significant background to the single-molecule experiments. Pyrrolidinium ionic liquids, on the other hand, have absorption from UV to 400 nm. The ILs were stored in a glove box to prevent moisture and oxygen from degrading them.

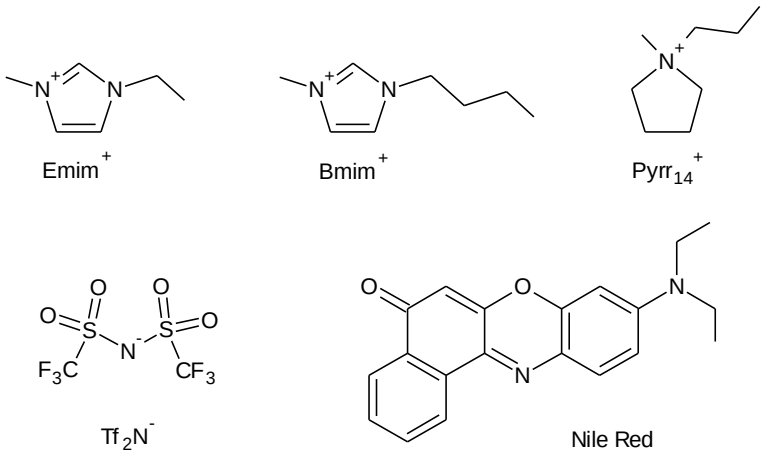

Scheme 3.1. Structures of the ionic liquid ions and the fluorescence probe, Nile Red

Nile Red (NR) was used as the fluorescent probe due to its solvatochromic behavior (Fig. 3.1). NR absorbs around 500-550 nm, a region where pyrrolidinium ILs do not show any absorption. NR is strongly positively solvatochromic.[151] In nonpolar solvent, such as isopantane, NR absorbs at 514 nm and emits at 574 nm. In polar solvents, such as ethylene glycol, NR absorbs at 570 nm and emits at 654 nm. NR in $Pyrr_{14}^{+}Tf_2N^{-}$ absorbs at 550 nm (Fig. 3.1) and emits at 626 nm, intermediary between acetonitrile and n-butanol, confirming previous observations that ILs have similar polarity as those solvents.[150]

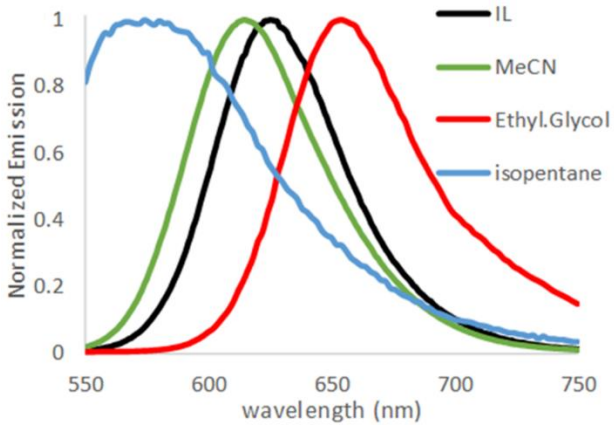

Figure 3.1. Normalized emission spectra of NR in different solvents (IL = $Pyrr_{14}^{+}Tf_2N^{-}$, MeCN = acetonitrile)

3.2.2. Instrumentations

For the confocal microscope, a 532 nm diode laser (Thorlab) was the excitation source. A 1.4 NA 100x oil objective (Olympus UPlanSAPO 100x 1.4 oil) was mounted on an inverted microscope (Olympus IX-71). The pinhole placed after the microscope was 100-μm. A 50-50 beam splitter (Semrock) was placed after the pinhole to split the emission onto two single photon avalanche diodes (Micro Photon Devices PDM50). Time-tagging

of the photons was done with a stand-alone time correlated single photon counting (TCSPC) module (Picoquant PicoHarp 300) and a detector router (Picoquant PHR 800). All the data were collected and analyzed using the SymPhoTime software package (Picoquant).

3.2.3. Fluorescence Correlation Spectroscopy (FCS)

FCS monitors the Brownian motions of the fluorescent probes in the femtoliter focal volume of a confocal microscope, and records the photon intensity over time, $I(t)$. The random fluctuations of the photon intensity caused by molecules diffusing in and out of the focal volume are used to calculate the diffusion constants of the molecules across the focal volume. The FCS curve, $G(\tau)$, is calculated by cross-correlating the photon intensity of the two detectors.[131–138]

$$G(\tau) = \frac{\langle \delta I(t) \delta I(t+\tau) \rangle}{\langle I(t) \rangle^2} \tag{3.1}$$

where $\langle \ \ \rangle$ denotes average over the entire trajectory, and $\delta I(t)$ is the deviation from the mean photon intensity at time t.

$$\delta I(t) = I(t) - \langle I(t) \rangle \tag{3.2}$$

If the focal volume is assumed to be described by a three-dimensional Gaussian function, $G(\tau)$ can be fitted to calculate the diffusion constant. If there are multiple difference local environments with different diffusion constants, $G(\tau)$ is described by[139]

$$G(\tau) = \frac{1}{N} \sum_{i=1}^{n} a_i \left(1 + \frac{\tau}{\tau_{D_i}}\right)^{-1} \left(1 + \frac{1}{\omega^2}\left(\frac{\tau}{\tau_{D_i}}\right)\right)^{-\frac{1}{2}} \tag{3.3}$$

where N is the average number of molecules in the focal volume, a_i is the contribution of the ith local environment, τ_{D_i} is the characteristic diffusion time for the ith local environment, and ω $(= z_0/r_0)$ is the dimension of the focal volume, where z_0 and r_0 are

the axial and radial dimensions of the focal volume. The diffusion coefficient, D, can be calculated from τ_D by[139]

$$\tau_D = r_0/4D \tag{3.4}$$

On the other hand, if the molecule is experiencing anomalous diffusion, where the mean square displacement of the molecule follows a power law, $\langle r(t)^2 \rangle \propto t^\alpha$. $G(\tau)$ is described by[139]

$$G(\tau) = \frac{1}{N}\left(1 + \left(\frac{\tau}{\tau_D}\right)^\alpha\right)^{-1}\left(1 + \frac{1}{\omega^2}\left(\frac{\tau}{\tau_D}\right)^\alpha\right)^{-\frac{1}{2}} \tag{3.5}$$

3.2.4. Burst Analysis

For burst analysis, the intensity time trace, $I(t)$, is analyzed using the photon-by-photon determination of emission burst scheme developed by Yang.[152] Instead of binning and setting a threshold, the waiting time between consecutive photon detection events are analyzed using the sequential probability ratio test (SPRT) by Wald[153] and the cumulative sum (CUSUM) scheme by Page.[154] The waiting time between consecutive photons are tested using statistical hypothesis testing to determine whether the photon is more likely part of a burst signal or background signal.

For the burst measurements performed in this study, the emission from the sample is split onto two detectors using a 50/50 beam splitter. Two different filters are placed in front of each detector to monitor the emission at the red edge versus emission at the blue edge simultaneously. The combined inter-photon duration sequence from both channels are analyzed using the scheme described above to determine the start and the end of a burst.

3.2.5. Simulation Models

All simulations were done using GROMACS.[155,156,157,158,159] To speed up the simulations, coarse-grained forcefield parameters for ILs were built based on OPLS-AA[160] and IL force field parameters developed by Lopes and Padua.[161,162] In the coarse-grained model, hydrogen atoms and fluorine atoms are combined with the nearest atom such that PF_6, $–CF_3$, $–CH_3$, $–CH_2–$, and –CH– are modeled as spheres. The charges of the spheres are the sum of the partial charges of the individual atoms. (For detail of the coarse-grained model, refer to Chapter 6). The Lennard-Jones parameters of the central atom are used as the first guess for the Lennard-Jones parameters of the spheres, then σ and ϵ are adjusted until the structure of the coarse-grained model closely matches the structure produced by all-atom model. For OPLS, dihedral potentials are modeled as Ryckaert-Bellemans functions:

$$V_{RB}(\phi_{ijkl}) = \sum_{n=0}^{5} C_n[\cos(\psi)]^n \tag{3.6}$$

The dihedral parameters are adjusted so that the distribution of dihedrals angels for coarse-grained model matches that of the all-atom model. The charges, non-bonding parameters, and the dihedral angle parameters are summarized in Table 3.1.

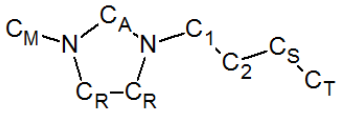

Figure 3.2. Atom names for the coarse-grain model

Table 3.1. Forcefield parameters for the coarse-grained imidazolium cation.

Lennard-Jones Potential and Charges

Atom	Charge (e)	σ (nm)	ϵ (kJ mol^{-1})
C_R	0.08	0.355	0.292880
N	0.15	0.325	0.711280
C_A	0.10	0.350	0.292880
C_M	0.2	0.380	0.276114
C_1	0.09	0.365	0.276114
C_2	0.13	0.365	0.276114
C_S	0.00	0.365	0.276114
C_T	0.00	0.380	0.276114

Dihedral Potential

Dihedral	C_0	C_1	C_2	C_3	C_4	C_5
C-C-C-C	-30	0	60	-60	0	0
N-C-C-C	-80	0	15	-15	0	0

The anion, PF_6, is modeled as a single sphere with $\sigma = 0.560$ nm and $\epsilon = 0.255200$ kJ mol^{-1}, and a charge of –1 e.[144] The dynamics for the coarse-grained model were faster than that for the all-atom model at the same temperature. Therefore, the temperature for the coarse-grained atom were scaled by a factor of 0.71 to make the dynamics the same.

$$T_{\text{coarse-grain}} = 0.71 \times T_{\text{all-atom}}$$

Coumarin 153, Hmim-like, benzene-like, and rhodamine 6G are the fluorescent probe used in the simulations. Coumarin 153 is described using the LJ and bonded parameters in the GROMACS OPLS-AA forcefield[160] and the charge distributions developed by Maroncelli. [163,164] The dipole moment of the coumarin 153 model is 6.24 D in the S_0 state and 13.59 D in the S_1 state. In addition to the charge distributions developed by Maroncelli, three other different charge distributions are studied: cationic coumarin 153, neutral coumarin 153, and quadrupolar coumarin 153. For the cationic coumarin 153, $+1/36$ e charge is added to each atom to give coumarin 153 an overall charge of +1 e with the same dipole moment. For the neutral coumarin 153, all the atoms have partial charges of 0. For the quadrupolar coumarin 153, the partial charges on 4 atoms (Figure 3.3) are changed so the dipole moment is 0, and the quadrupole moment tensor, Q, is

$$Q = \begin{bmatrix} 2.1583 & 7.0201 & -0.2750 \\ 7.0201 & -5.2709 & -0.3181 \\ -0.2750 & -0.3181 & 3.1126 \end{bmatrix}$$

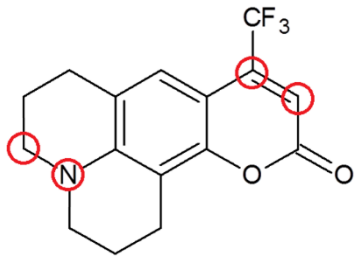

Figure 3.3. Structure of coumarin 153. The circled atoms are the atoms whose charges are altered in the quadrupolar coumarin 153.

Two different charge distributions of Hmim-like probe are employed. For the neutral Hmim-like probe, all the partial charges for atoms are set to zero. For the dipolar Hmim-like probe, first, the partial charges of all atoms are subtracted by a constant such

that the overall charge is zero. Then the partial charges of all atoms are scaled by a different constant such that the dipole moment with respect to the center of mass is similar to that for dipolar coumarin 153.

For the dipolar-benzene like solute, the LJ parameters for carbon are $\sigma = 3.5$ Å and $\epsilon/k_B = 40.3$ K and for hydrogen are $\sigma = 2.5$ Å and $\epsilon/k_B = 25.2$ K.[165] The partial charges are $+0.1350$ e and $-0.1350\ e$ for hydrogen and carbon, respectively. To make the benzene-like solute dipolar, $\pm e$ partial charges are added to the 2 carbon atoms in the para positions, while the remaining four carbon and six hydrogen atoms have the same partial charges. This results in a benzene-like solute with a dipole moment of 13.5 D.

The force field parameters for rhodamine 6G were developed by Popov, Steinkerchner, and Mann,[166] following the methods described in Smith et al.[167] and Vaiana et al.[168] The rhodamine 6G has an overall charge of $+1$ e and a dipole moment of 1.80 D.

Two different types of simulation were performed: isoconfigurational and non-isoconfigurational. For the isoconfigurational simulations, 2 Coumarin 153 molecules were placed in 128 $HMI^+PF_6^-$ ion pairs. Ten initial configurations were generated for S_1 state. For each initial configurations, 20 20ns-trajectories were calculated at 350K. For the non-isoconfigurational simulations, eight different systems were studied:

1. 2 dipolar coumarin 153 in 128 HMI^+PF_6– ion pairs
2. 2 cationic coumarin 153 in 128 HMI^+PF_6– ion pairs
3. 2 quadrupolar coumarin 153 in 128 $HMI^+PF_6^-$ ion pairs
4. 2 neutral coumarin 153 in 128 $HMI^+PF_6^-$ ion pairs
5. 2 dipolar benzene in 128 $HMI^+PF_6^-$ ion pairs
6. 2 cationic rhodamine 6G in 128 $HMI^+PF_6^-$ ion pairs

7. 6 dipolar Hmim-like solute in 122 $HMI^+PF_6^-$ ion pairs

8. 6 neutral Hmim-like solute in 122 $HMI^+PF_6^-$ ion pairs

For each system, 100 50ns-trajectories were simulated from 100 different initial configurations.

3.3. Results and Discussions

3.3.1. Wavelength-Dependent FCS of Nile Red in ILs

To study the connection between local polarity and diffusion, FCS was performed with NR as the probe. As NR has a strong positive solvatochromism, its translational motion through environments of differing polarities can be followed by measuring FCS curves at the red edge and the blue edge of its emission spectrum. Three different combinations of long pass (LP), short pass (SP) and band pass (BP) filters were used to obtain wavelength-selected FCS curves at the blue and red edges of the NR emission spectrum. The three pairs differ from one another by the bandwidth of the spectrum collected: (1) 605±28-nm BP (blue) and 650±20-nm BP (red), (2) 570-nm LP combined with 600-nm SP (blue) and 645-nm LP (red) (3) 580±5-nm BP (blue) and 650±5-nm BP (red). As a control, the entire emission spectrum was collected using a 570-nm LP filter. The normalized FCS curves fit to two diffusion components α_1 and α_2 with different characteristic residence times, τ_1 and τ_2[139]

$$G(\tau) = G(0)\left\{\frac{\alpha_1}{\left[1+\left(\frac{\tau}{\tau_1}\right)\right]\left[1+\omega^2\left(\frac{\tau}{\tau_1}\right)\right]^{\frac{1}{2}}} + \frac{\alpha_2}{\left[1+\left(\frac{\tau}{\tau_2}\right)\right]\left[1+\omega^2\left(\frac{\tau}{\tau_2}\right)\right]^{\frac{1}{2}}}\right\} \quad (3.7)$$

are shown in Figure 3.4.

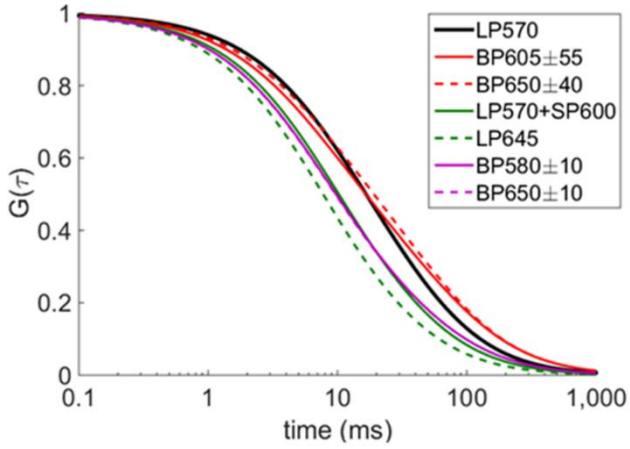

Figure 3.4. Normalized and fitted FCS curves of NR in $Pyrr_{14}^{+}Tf_2N^{-}$ with various filter sets. Residual plots for the fitting can be found in Appendix Figure A3.2–A3.8.

Table 3.2. Fitted FCS parameter for the various filter sets used.

	Filter	α_1	τ_1 (ms)	α_2	τ_2 (ms)	α_1'*	α_2'*
Control	LP570	0.46	12.8	0.54	47.9	0.46	0.54
1	BP605±55	0.51	9.1	0.49	83.2	0.39	0.59
	BP650±40	0.43	9.0	0.57	74.5	0.31	0.67
2	LP570+SP600	0.69	10.4	0.31	46.3	0.78	0.21
	LP645	0.80	9.2	0.20	41.9	0.97	0.02
3	BP580±10	0.70	9.0	0.30	63.1	0.77	0.22
	BP650±10	0.71	9.3	0.29	65.7	0.76	0.22

*α_1' and α_2' are the fitted FCS parameters for different filters where τ_1 and τ_2 values are fixed at 12.8 ms and 47.9 ms, the τ values for LP570.

While the parameters obtained vary with the filter set chosen (*cf.* sets 1 and 2, Table 3.2), similar results are obtained using the red and blue edge filters within any given set.

This means that the FCS curves, fitting parameters, and therefore the diffusion constants are insensitive to whether the probe is emitting predominantly from a polar (red) or a non-polar (blue) environment. The differences seen between different filter sets (1-3) are likely due to the bandwidth of filters and the specific wavelengths collected. Similar variations are observed for NR in methanol and acetonitrile which are fast-relaxing solvents that should not exhibit local heterogeneous domains on the timescale of FCS measurements.

Alternatively, the FCS curves can be fitted by using the τ values of the control (570nm LP collection, see above), $\tau_1 = 12.8$ ms and $\tau_2 = 47.9$ ms,

$$G(\tau) = G(0)\left\{\frac{\alpha'_1}{\left[1+\left(\frac{\tau}{12.8}\right)\right]\left[1+\omega^2\left(\frac{\tau}{12.8}\right)\right]^{\frac{1}{2}}} + \frac{\alpha'_2}{\left[1+\left(\frac{\tau}{47.9}\right)\right]\left[1+\omega^2\left(\frac{\tau}{47.9}\right)\right]^{\frac{1}{2}}}\right\} \quad (3.8)$$

If there are only two subpopulations that correspond to probes in the nonpolar and polar regions and the two τ values represent their respective characteristic residence times, changing the wavelengths should only affect their relative contributions, α'_1 and α'_2, and not their residence times, τ_1 and τ_2. Though not perfect, the residual plots (Appendix Figures A3.3–A3.8) show that all FCS curves are reasonably fitted with the τ values from LP570. With the exception of filter pair (2), the amplitudes remain largely unchanged when a blue filter is replaced with a red filter. This points to the same conclusion as above, *i.e.*, the solute diffusion rate does not vary with local polarity. Thus the origin of bimodal diffusion observed in ILs cannot be ascribed to transport of probes exclusively in polar or nonpolar regions.

3.3.2. Burst analysis with Confocal Microscopy

To determine whether fluorescent probes partition into two different regions in ILs, burst analysis with two different bandpasses, red edge vs. blue edge, were placed in front of the detectors to monitor the emission from each burst simultaneously. Experiments have shown that the polarity of ILs are similar to that of acetonitrile or a short-chained alcohol.[150] The emission spectra of NR indicate that the polarity of $Pyrr_{14}^{+}Tf_2N^{-}$ is similar to that of acetonitrile or acetone. (Fig. 3.5)

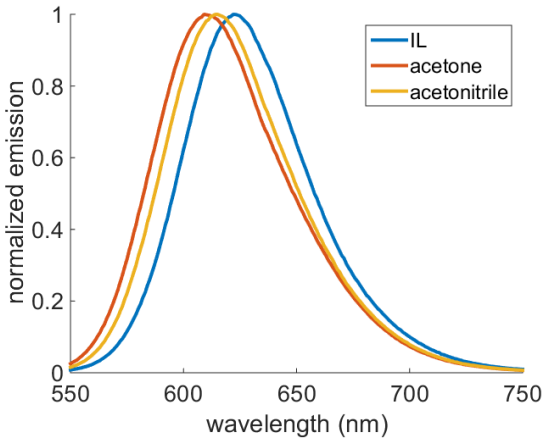

Figure 3.5. Emission spectra of Nile Red in $Pyrr_{14}^{+}Tf_2N^{-}$, acetone, and acetonitrile.

To examine the solvation environments, burst analysis was performed with a set of filters that only collects the edges of the emission spectra. A 645 nm longpass was used for the polar channel, and a combination of a 570nm longpass and a 600 nm shortpass was used for the nonpolar channel. The number of photons collected from each detector was normalized by the bandwidth of the filters and the percentage of photons from the polar (red) channel was calculated for each burst. The distribution of the percentages was analyzed and plotted in Figure 3.7. For example, over a 5-minute trajectory, hundreds of

bursts are collected. For each burst, the number of photon detected in the polar/nonpolar channels are totaled and normalized by dividing each total by the area of the filtered emission spectra. Then, the percentage of polar photons is calculated by dividing the number of polar photons by the total number of photons during the burst. As a result, each burst is characterized by a single percentage. Finally, the distribution of this percentage is plotted.

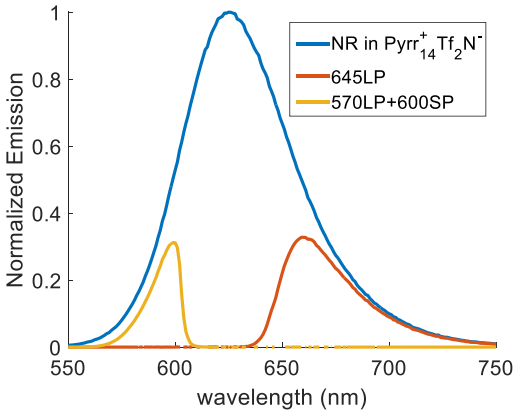

Figure 3.6. Emission spectra of Nile Red in $Pyrr_{14}^{+}Tf_2N^{-}$ with different filters.

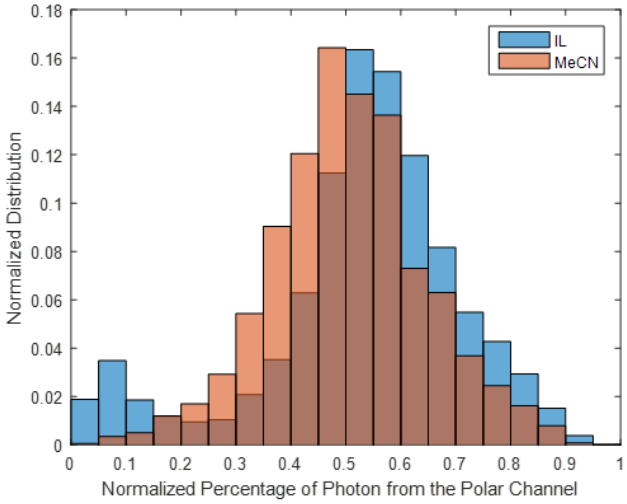

Figure 3.7. Normalized percentage of photons from the polar channel for NR in IL and acetonitrile. Polar channel: LP645; nonpolar channel: LP570 and SP600.

If the solvent environment surrounding the solute relaxes quickly and the solute samples differing solvent configurations sufficiently, the emission spectrum of each burst should be similar to that of the bulk. The resulting photon distribution from the polar channel should be a Gaussian, as in the case with acetonitrile. Remarkably, the distribution for the IL is bimodal, indicating that the probe is unable to sample solvent configurations sufficiently while passing through the focal volume. While majority of the bursts have similar emission spectra, roughly 15% of the bursts emit bluer wavelengths. The distributions of the burst durations are similar between the two peaks (Appendix Figure A3.1), which rules out the possibility that the bluer emission is a result of insufficient sampling due to shorter bursts. These results indicate that a rather long-lived structural heterogeneity does exist in ILs though the heterogeneity is *not* characterized by differing solute diffusion rates.

3.3.3. Comparison between Simulation and Experiments

To look at the local polarity around the probes in more detail, molecular dynamics simulations were performed.

Table 3.3. Comparison between confocal microscopy and molecular dynamics

	Confocal Microscopy	Molecular Dynamics
Length of Bursts	1μs ~ 1ms	50 ns
Length Scale	~1 μm	~4 nm
Sampling frequency	~4 ns	1 ps
Fluorescent probe	Nile red	Coumarin 153
Electronic state		S_1
Ionic Liquids	$Pyrr_{14}^{+}Tf_2N^{-}$	$Hmim^{+}Tf_2N^{-}$

The length of trajectories for confocal microscopy is the length of time that a probe is in the focal volume. The length scale for confocal microscopy is the size of the axis of the focal volume, and the length scale for the molecule dynamics is the periodic box size used in simulations. For confocal microscopy, the sampling frequency is the fluorescent lifetime of the probe; for molecule dynamics, the sampling frequency is how often the coordinates are saved during the simulation. For molecule dynamics, equilibrium simulation with the S_1 charge distribution was performed.

The comparison between experiment and simulation necessitated several adjustments. First, simulations were performed on C153 because its force field parameters are readily available.[163,164,169] However, C153 proved unsuitable for FCS measurements and yielded high background fluorescence so Nile Red was used instead. As simulations correctly reproduced the width of the emission spectra of NR (Figure 3.8), C153 and NR experience similar solvation environments. This validates the comparison of simulation and experiment. Second, a pyrrolidinium IL was used in experiments because, unlike

imidazolium ILs, it is not fluorescent in the visible range. Finally, to ensure that the formation of non-polar regions is captured in simulation, a long-chain IL was used for modeling.[170,171] However, shorter-chain ILs were used in experiment as these have been shown experimentally to also form non-polar regions.[172–178] Finally, to reduce the number of atoms in simulation, a smaller anion was used.

To gain insight into the experimental results, MD simulations of C153 were performed. We simulated 200 different trajectories, each for 50 ns, and analyzed the change in the Franck-Condon (FC) energy of the probe that is induced by solvation[142,143,179,180,181]

$$Z = \left[V_e^s(r,R) - V_g^s(r,R)\right] - \left[V_e^0(r) - V_g^o(r)\right] \tag{3.9}$$

here $V_g^0(r)$ and $V_e^0(r)$ are the ground- and excited-state electronic energies of the isolated probe, $V_g^s(r,R)$ and $V_e^s(r,R)$ are the corresponding energies in solution, and r and R are the solute and solvent coordinates, respectively. Z is a collective (solvent) coordinate, widely employed to describe solvation effects.[182] With the solvent in equilibrium with the excited-state solute charge distribution, the emission spectrum can be calculated from the distribution of *Z via*

$$\Delta E_{ems} = \left[V_e^0(r) - V_g^0(r)\right] + Z \tag{3.10}$$

To compare with the NR spectra, $\left[V_e^0(r) - V_g^0(r)\right]$ of the probe was adjusted such that MD yields the correct NR emission maxima. Simulation reproduces the width of the experimental NR emission spectra $\left[V_e^0(r) - V_g^0(r)\right]$ for Nile red is 221 kJ/mol.

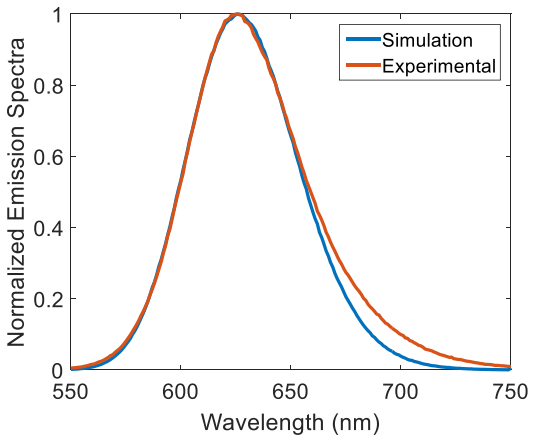

Figure 3.8. Simulated and experimental emission spectra of Nile Red in ionic liquid

3.3.4. Local Polarity and Structure Simulated by MD

To look at the distribution of local polarity, the emission spectra for each individual trajectory and the distribution of the spectra are plotted in Figure 3.9. The distribution is plotted in log-scale to show the features of the distribution more clearly.

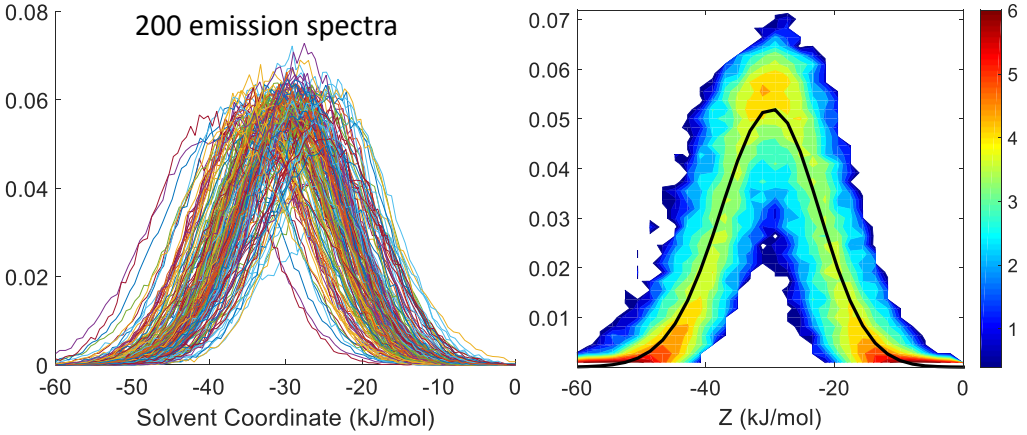

Figure 3.9. Distribution of emission spectra from 200 trajectories. The distribution is plotted in log scale, and the black line is the averaged emission spectra of 200 trajectories.

Emission spectra calculated from individual trajectories show a large variation in both width and peak position. This indicates that there are more than simply two (viz., polar and nonpolar) local environments, and the solute is not able to sample different environments sufficiently within each trajectory of 50ns. Out of the 200 trajectories, one trajectory showed a bimodal emission spectra (Figure 3.10). The bimodal emission spectrum suggests that the probes do switch between environments with different polarities. Since only one trajectory has a bimodal spectrum, this suggests that either the swtiching between environments is rapid with a timescale shorter than the length of the trajectories, 50 ns or the switching is an extremely rare event.

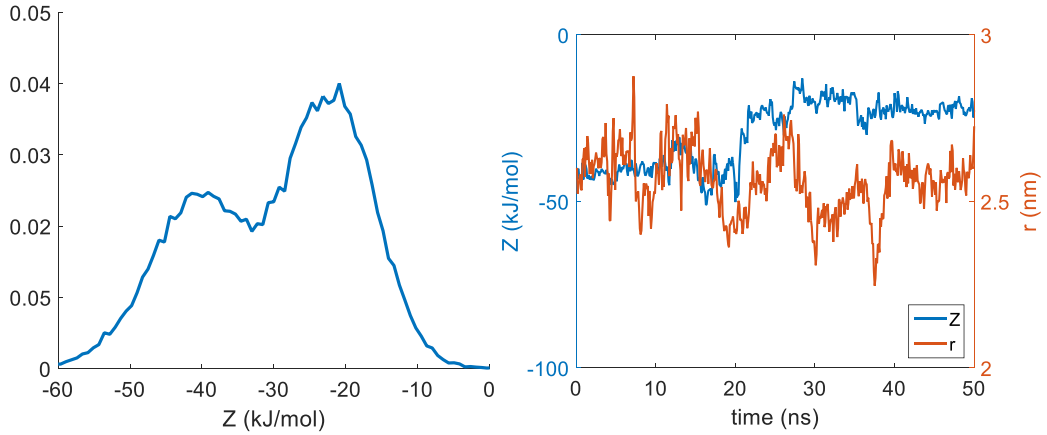

Figure 3.10. (left) The only bimodel emission spectra out of 200 trajectories (right) Z and r vs. time for the trajectory with bimodal trajectories. Z and r are averaged over 100 ps to eliminate fast component of the motion.

To examine the local environment around the probe as a function of time, Z as a function of time is plotted for the trajectory exhibiting bimodal emission spectra. (Figure 3.10). Z is averaged over 100 ps to eliminate fast component of the motion. The plot

showed that there is a large jump in Z as Z increased over 20 kJ/mol within a span of 2 ns at $t = 20$ ns. Analysis of other trajectories also showed large jumps in Z over a span of a couple ns. (Figure 3.11).These large amplitude changes in Z suggest the existence of multiple local environments with different polarities, and their switching between these environments is not gradual.

Past simluations have shown there to be large amplitude changes in position for ILs and solute in ILs.[144] To see whether the large jumps in position are related to the large changes in local polarity, a plot of the the center of mass position vs. time is superimposed on the Z vs. time graphs. The overlayed graphs show that the large jumps in center of mass of the probe do not correlate with large changes in local polarities. Specifically, large changes in r could occur without large changes in Z, and *vice versa*. The overlaid graphs suggest that the large changes in polarity are not due to probes jumping from one environment to another environment, but rather that they are likely due to motions of the solvent ions.

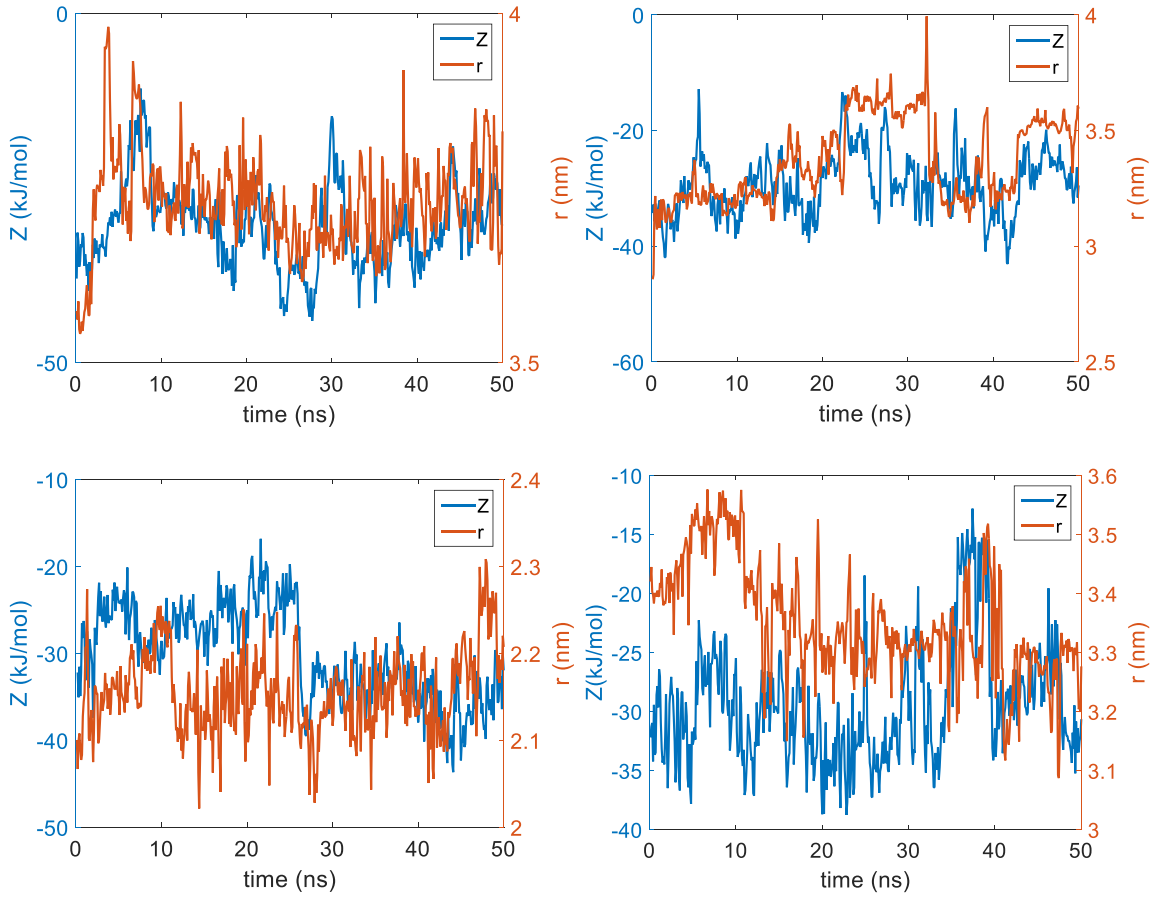

Figure 3.11. Z vs. time for other trajectories that exhibits a large jump in Z but do not exhibit bimodal emission spectra. Z is averaged over 100 ps to eliminate the fast component of the motion.

The presence of multiple local polarities in simulation does not contradict the earlier experimental observations. These large amplitude changes occur frequently in simulation which means in experiments, where the timescale is orders of magnitude larger, these large jumps would be averaged out and the probe would appear to only exist in two distinct local environments.

Next, we will examine the local solvent structure around the probe using equilibrium MD simulations. Nonpolar and polar atoms were defined using the definitions

from ref 123, which assigned the atoms using the partial charges on the atoms. The cation atoms in the imidazolium ring or attached to the ring are considered polar. All anion atoms are also assigned as polar. The atoms in the hexyl group of the cation, excepting that attached to the ring, are considered to be nonpolar. To examine the effects of solute charge distribution on local structure, the local structure of cationic C153 and quadrupolar C153 (two model solute) were also examined along with the local structure of dipolar C153.

The radial distribution functions (RDFs) of nonpolar and polar atoms around the center of mass of coumarin follows the range of coulombic interaction. Their interactions decrease from cationic to dipolar to quadrupolar. As the range of coulombic interaction decreases, the polar atoms move father away from the solute and becomes less structured. On the other hand, the nonpolar atoms move closer to the solute as the range of coulombic interaction decreases. Interestingly, the nonpolar atoms are closer to the solute than the polar atoms for all three charge distributions. This is because the nonpolar atoms can get closer to the solute than the polar atoms. Due to their structure and shape, the nonpolar alkyl chain can get closer to the solute than can the polar imidazolium ring or PF_6^-.

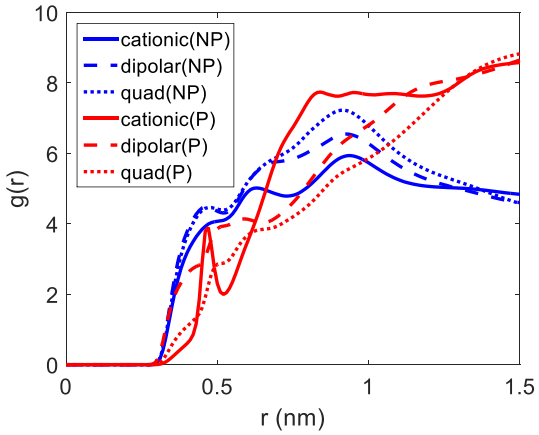

Figure 3.12. RDFs of nonpolar (NP) or polar (P) atoms around the center of mass of coumarin 153 with different charge distributions (cationic, dipolar, and quadrupolar) The RDFs are normalized with respect to overall density, *i.e.* at $r \to \infty$, $g_{\text{nonpolar}}(r)/g_{\text{polar}}(r)$ equals to the ratio of nonpolar atoms to polar atoms

RDFs, while informative, can only give information on the averaged equilibrium structure. To study the distribution of structures, a 2-D distribution of coordination number is plotted. For each trajectory, the RDFs for each nanosecond is calculated. For example, for a 50-ns trajectory, 50 RDFs of nonpolar and polar atoms around the solute are calculated for 0 ns to 1ns, 1 ns to 2ns, …, etc. Then, from the RDFs, the coordination number up to 5Å, 6Å, and 7Å is calculated using

$$n = 4\pi \int_0^{r'} r^2 g(r) \rho dr \tag{3.11}$$

where r' is 5Å, 6Å, or 7Å, $g(r)$ is the RDF, and ρ is the number density. To visualize the distribution, the coordination numbers of each the polar and nonpolar atoms are converted to a coordinate system (x, y), where x is the coordination number of the polar atoms and y is the coordinate of the nonpolar atoms. Therefore, for a 50-ns trajectory, 50 (x, y)-

coordinates are generated. The distribution of the coordinates for 100 trajectories are plotted below in Figure 3.13.

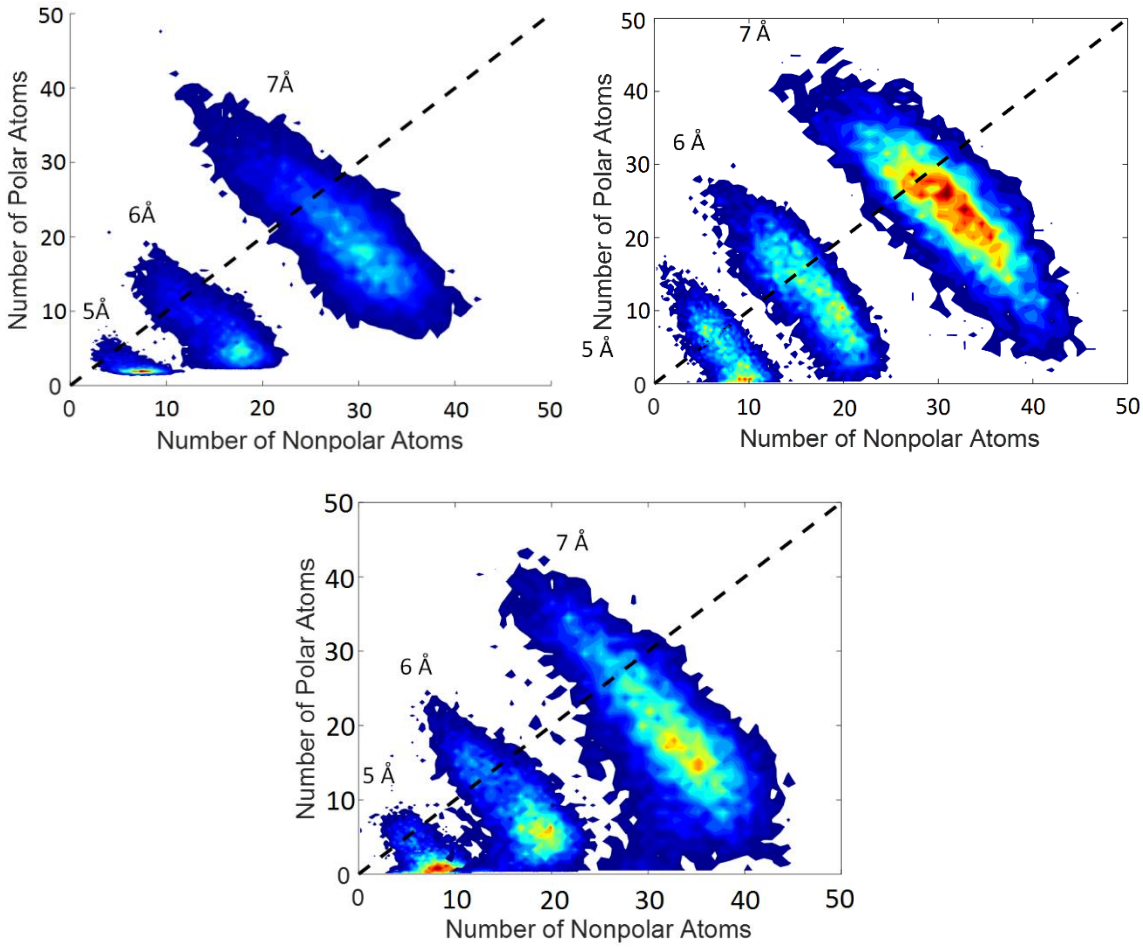

Figure 3.13. 2D density plot of coordination number of polar vs. nonpolar atoms for three different charge distribution: (top left) cationic, (top right) dipolar, and (bottom) quadrupolar. The black dash line is where number of polar atoms equal to the number of nonpolar atoms. Three different distances are used for the calculation of coordination number: 5Å, 6Å and 7Å.

Similar to the RDFs, the density plots show that C153 is surrounded by mostly nonpolar atoms for all three charge distributions. Even though the probes sometimes are surrounded by mostly polar atoms, all three density plots have only a single peak and the distributions are either 2-D Gaussian or skewed 2-D Gaussian. If there are only two environments (polar and nonpolar) and there is a significant barrier for crossing from nonpolar to polar, the distribution should be bimodal. The lack of a bimodal distribution is another evidence that, even though IL partition into nonpolar and polar regions, the local environments around the solute cannot be simply categorized as polar or nonpolar.

Even though there is only one peak, the density plots are not symmetric, especially for $r = 5$ Å and 6 Å. If there is only one stable local environment, the density distribution should be symmetric. The skewed distribution suggests there is more than one stable local environment. Specifically, there must be some stable local environments in which the solute is surrounded by mostly polar atoms which makes the distribution skew toward the top left corner. In the next section, the time evolution of the local structure is examined more closely using isoconfigurational simulation.

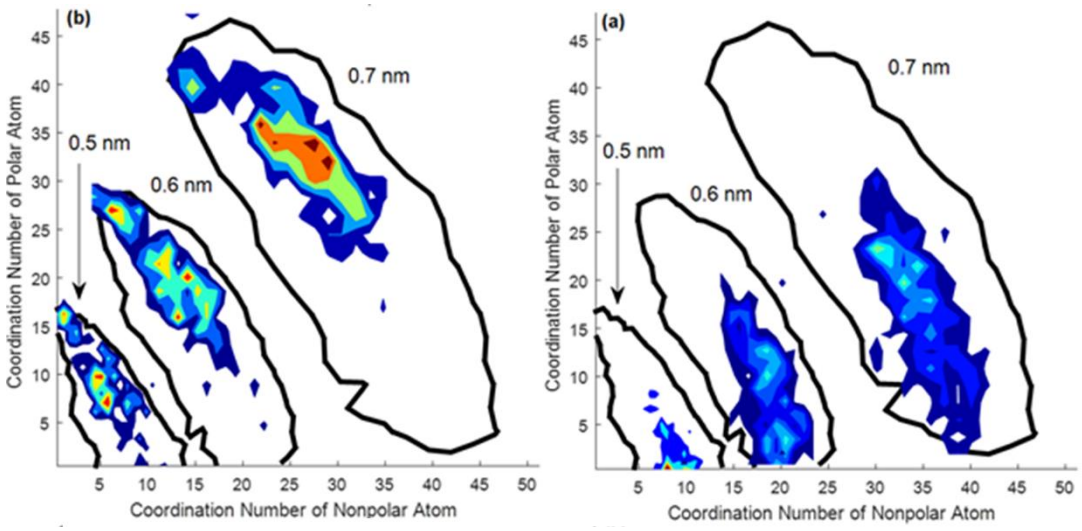

Figure 3.14. 2D density plots of coordination number of polar vs. nonpolar atoms around dipolar coumarin 153 for the trajectories with most red-shifted spectra (left) and the trajectories with most blue-shifted emission spectra (right). The black outline are the outline for the density plot for all trajectories. Three different distance is used for the calculation of coordination number: 5Å, 6Å and 7Å.

Before examining the time evolution of the local environments and local polarities, the relationship between structure and vertical energies is examined. To validate the assignment of polar versus nonpolar atoms, the density plots of extreme vertical energies are examined. If a probe is surrounded by mostly nonpolar or polar atoms, it should have the most blue-shifted or red-shifted emission spectrum, respectively. The averaged Z for each trajectory is calculated and the results obtained that are in the top and bottom 5 percentiles of the average Z value are compared with the equilibrium results in Figure 3.14. For trajectories with the bluest emission (top 5%), the solute is surrounded by more nonpolar than polar atoms, as expected. The opposite is true for trajectories with the reddest

emission (bottom 5%). The density plots showed that the assignment of nonpolar and polar atoms by partial charges is appropriate.

Figure 3.14 can also be used to examine the importance of distance in determining the local polarity. As the distance analyzed increases from 5 to 7 Å, the 2D structural distributions of the top and bottom 5 percentiles overlap more extensively and move away from the edges of the equilibrium distribution. This indicates that the atoms close to the solute play the most important role in determining the local polarity.

3.3.5. Time Evolution of the Local Structure

To study the dynamics of the local environments, isoconfigurational simulations were performed. Two sets of ten initial configurations were generated from equilibrium trajectories. The solute is surrounded mainly by nonpolar atoms in one set and by polar atoms in the other. For each initial configuration, 20 trajectories with different initial velocities were simulated. Figure 3.15 show the evolution of the solvation structure over 20 ns.

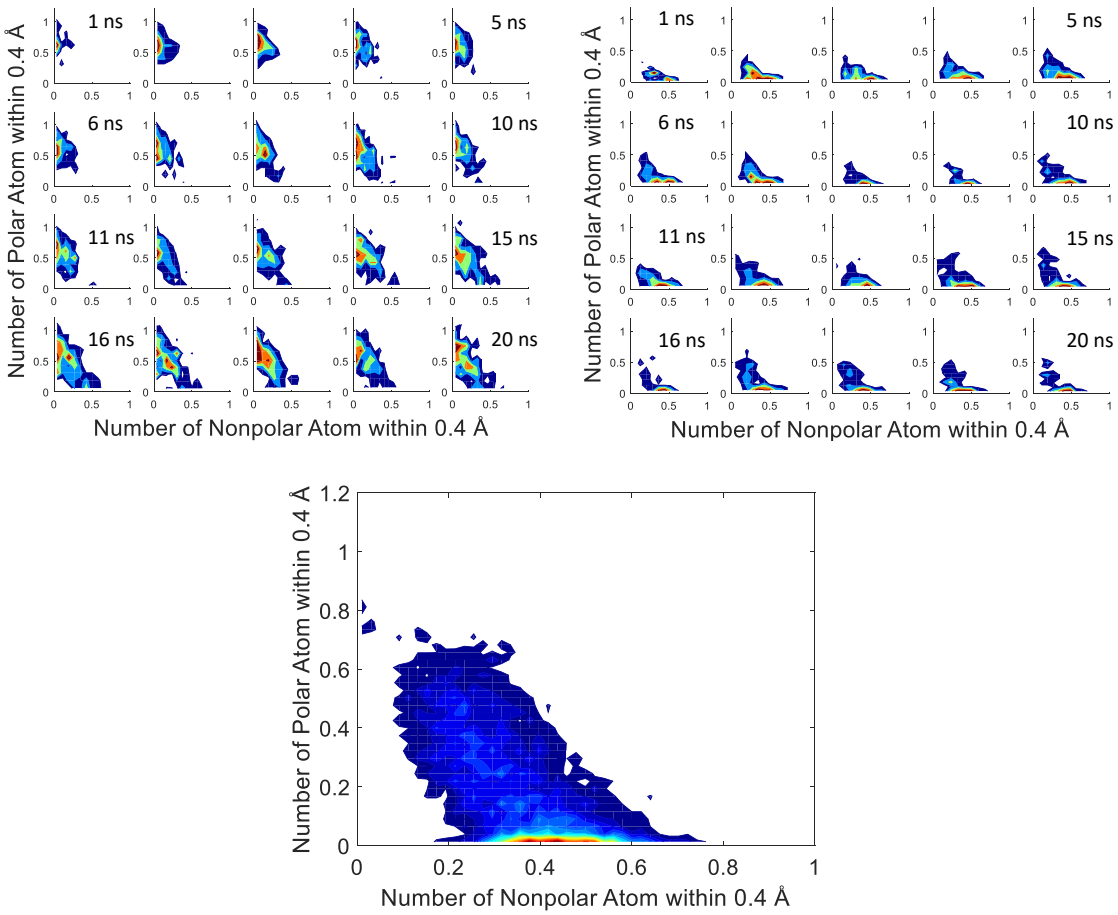

Figure 3.15. Time evolution of the density plot with an initially polar (top left) or nonpolar environment (top right). The equilibrium density plot for dipolar coumarin 153 sampled from 100 trajectories with random initial configurations.

Initially, the environment around the probe is composed entirely of nonpolar or polar atoms depending on the initial structure. For both sets of initial configurations, some trajectories cross over to regions of opposite polarity after 10 ns. For nonpolar initial configurations, the density map becomes similar to the equilibrium density after 10 ns. By contrast, the density map evolving from polar initial configurations, though significantly relaxed, shows deviations from the equilibrium distribution. Since C153 is surrounded

mainly by nonpolar atoms at equilibrium, the nonpolar initial configurations will reach the equilibrium distribution faster than will the polar initial configurations.

It is noteworthy that some polar configurations show very slow relaxation despite their large deviations from the equilibrium structure. For example, the peaks at (0,12) and (5,12) at t = 1 and 2ns are still present after 20ns (Figure 16). Even though the solute is surrounded by nonpolar atoms most of the time, due to fluctuations in the solvent structure and diffusion of the solute, the solute could go to an environment that contain mostly polar atoms. Once there, it might switch back to nonpolar environment or it might be trapped in the polar environment for more than 20 ns. The slow structural relaxation of the IL, attributed to its high viscosity, explains the large variation observed in the simulated emission spectra, the bimodal distribution in the burst analysis, and the skewed distributions in the density plots.

3.3.6. Heterogeneous Translational Dynamics in ILs

Both experiments and simulations show that the IL structure around the solute is heterogeneous and that the structural heterogeneity can be long-lived. The solute transport dynamics at a given polarity are also heterogeneous as evidenced by the fact that the FCS curves cannot be fit with the simple diffusion model. Instead, the FCS curves are better fitted with the two-diffusion constant model or the anomalous diffusion model. Since structural heterogeneity cannot explain the two-diffusion constant model, the anomalous diffusion model provides an alternative interpretation to the complex diffusion observed in ILs. With the anomalous diffusion model, the MSD follows a power law

$$\langle r(t)^2 \rangle \propto t^{\beta} \tag{3.12}$$

If $\beta > 1$, dynamics is considered to be super-diffusive, and if $\beta < 1$, dynamics is considered to be sub-diffusive. For anomalous diffusion, the FCS curve becomes[139]

$$G(\tau) = \frac{1}{N}\left(1 + \left(\frac{\tau}{\tau_D}\right)^{\beta}\right)^{-1}\left(1 + \frac{1}{\omega^2}\left(\frac{\tau}{\tau_D}\right)^{\beta}\right)^{-\frac{1}{2}} \tag{3.13}$$

Table 3.4. Fitted FCS parameters with bimodal diffusion or anomalous diffusion

Probe	IL	Anomalous		Bimodal		
		β	τ	α_1	τ_1	τ_2
Nile red	$Emim^+Tf_2N^-$	0.83	16.3	0.70	9.24	60.4
	$Bmim^+Tf_2N^-$	0.83	21.9	0.68	11.8	77.2
	$Pyrr_{14}^+Tf_2N^-$	0.76	30.8	0.54	10.5	98.2
Rhodamine 6G	$Emim^+Tf_2N^-$	0.81	23.6	0.62	11.2	77.8
	$Bmim^+Tf_2N^-$	0.73	40.1	0.53	11.9	134
	$Pyrr_{14}^+Tf_2N^-$	0.70	44.3	0.47	9.64	139

FCS of NR, a dipolar probe, and rhodamine 6G, a cationic probe, in three different ionic liquids are fitted with bimodal diffusion and anomalous diffusion. Both anomalous diffusion and bimodal diffusion fit the FCS curve well. The results from the fitting is tabulated in Table 3.4, and the residual plots can be found in the Appendix.

Numerous experimental and simulation studies have shown that dynamics in ionic liquid can be considered glassy, meaning that the dynamics are sub-diffusive.[183–187] Yamamuro studied C_8mim^+ with various anions using neutron diffraction and neutron spin echo techniques.[125,126,141] The intermediate scattering functions are best-fitted with a

stretched exponential (Kohlrausch-Williams-Watts) function with $\beta = 0.5$.[125,126,141] In simulations, self-inetermediate scattering function of $Emim^{+}PF_6^{-}$ is best-fitted with $\beta = 0.64$ and 0.59 for cations and anions, respectively.[144] A deviation of β from unity is a good indicator of glassy dynamics in ILs.

For a non-reactive system, the FCS curve $C(\tau)$ is[131]

$$C(\tau) = [geQ(\lambda)]^2 \sum_{\alpha} \varphi_{\alpha\alpha}(\tau) \tag{3.14}$$

where g and $Q(\lambda)$ are the gain and quantum efficiencies of the detectors, and $\varphi_{\alpha\alpha}(\tau)$ is the photon flux correlation function associated with a given molecular species α. For our system, only the solute dyes contribute to $C(\tau)$. If neither the excitation nor the emission is polarized, $\varphi_{\alpha\alpha}(\tau)$ becomes

$$\varphi_{\alpha\alpha}(\tau) = NK \int d^3r \int d^3r' \int \frac{d^3\hat{k}_f}{4\pi} \int \frac{d^3\hat{k}'_f}{4\pi} P(r)P(r')G_s(r - r', t) \tag{3.15}$$

where N is the number of molecules, K is a constant that contains the extinction coefficient, quantum yield and laser intensity, $P(r)$ is the laser profile, and the integrations $d^3\hat{k}_f/4\pi$ and $d^3\hat{k}'_f/4\pi$ are over the collection solid angle. $G_s(R,t)$ is the self-part of the van Hove function for α.[143, 188, 189, 190] The Fourier transform of the van Hove function is the incoherent intermediate scattering function, $F_s(R,t)$.[144,188,191] Both $G_s(R,t)$ and $F_s(R,t)$ can be studied using MD simulation. $F_s(q,t)$ can be fitted using a stretched exponential function with the stretching exponent β that appears in the fitting of the FCS data (Eq. 3.13).

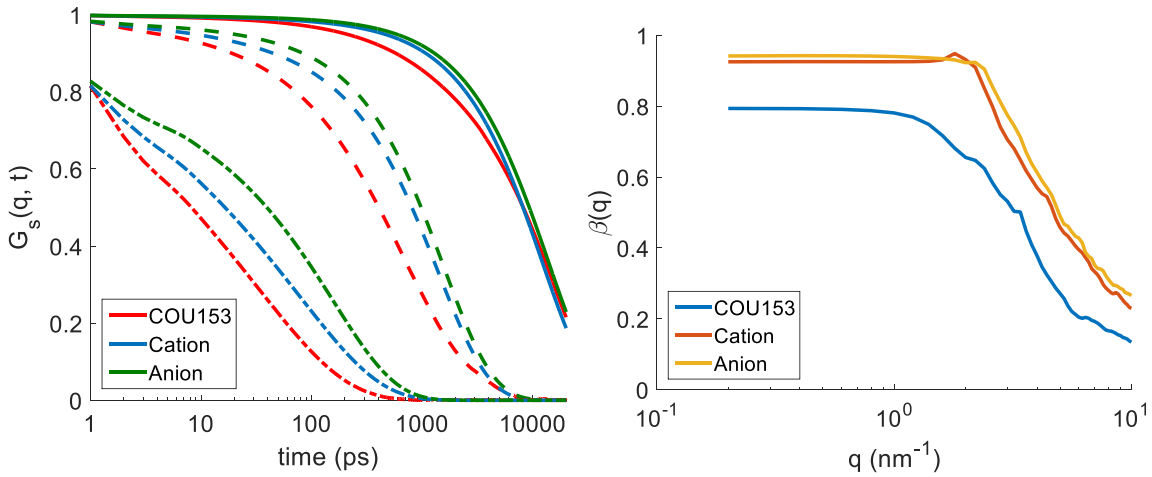

Figure 3.16. (left) Incoherent intermediate scattering function, $F_s(R,t)$ of coumarin 153, $Hmim^+$, and PF_6^- for $q = 0.1$ $nm^{-1}(-)$, 1 $nm^{-1}(--)$, and 10 $nm^{-1}(-$ -). (right) The stretch exponent, β, for the Kohlrausch-Williams-Watts function as a function of q for coumarin 153, $Hmim^+$, and PF_6^-.

Both α and β relaxations are observed in $G_s(q,t)$ for $q = 0.1$ nm^{-1} and 1 nm^{-1} but not for $q = 10$ nm^{-1}. For all three values of q, coumarin 153 has the fastest relaxation while the anion, PF_6^-, has the slowest relaxation. The MD results for $F_s(q,t)$ were fitted to a stretched exponential function. The resulting values of β are displayed as a function of q in Figure 18. $Hmim^+$, Tf_2N^-, and dipolar C153 have β values less than unity at all q and β plateaus when q is less than 1 nm^{-1}. The value of β as q approaches zero determines the value of β obtained from experiment since the lengthscale of the FCS experiment is large. Interestingly, the β value for C153 is lower than that for the IL cations and anions which means the relaxation dynamics of C153 are more heterogeneous than those of the IL ions. In addition to the glassy dynamics of the solvent, there are other factors that make the dynamics of coumarin 153 more heterogeneous than those of the solvent.

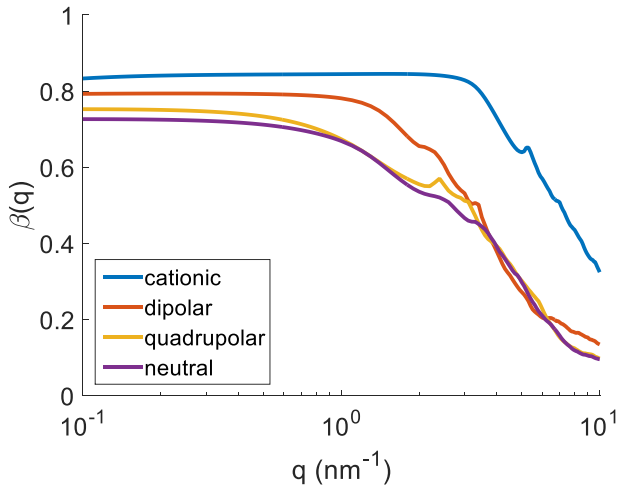

Figure 3.17. The stretch exponent, β, as a function of q for cationic, dipolar, quadrupolar, and neutral coumarin 153

To understand why C153 shows more heterogeneous dynamics than do the ions, various C153 models with different electric multipole moments were examined. (Figure 3.17). The dynamics of cationic C153 were found to be the least heterogeneous while those of neutral C153 are the most heterogeneous. Overall, the degree of heterogeneity in the dynamics tracks the length scale of the relevant electrostatic interactions. The monopole forms have the longest-range electrostatic interactions with the surrounding ions while these are absent for the neutral form. For longer-range interactions, the differences among solvation environments are diminished due to interactions with a greater number of IL ions and therefore better averaging of influence of differing local environments. As a result, the dynamics are least heterogeneous for cationic coumarin and most heterogeneous for the neutral and quadrupolar forms.

This trend is not observed in experiments, however, for all three ILs tested, the stretch exponent for rhodamine 6G, a cationic probe, is similar to that for NR, a dipolar

probe. Unlike in MD simulations, where only the electrostatic multipole moments are different for the probes, comparison of NR and rhodamine 6G introduces other factors such as size and shape of the probe. To examine the effect of size and shape on the degree of dynamic heterogeneity, MD simulations with a benzene-like probe, a Hmim-like probe, and rhodamine 6G were performed.

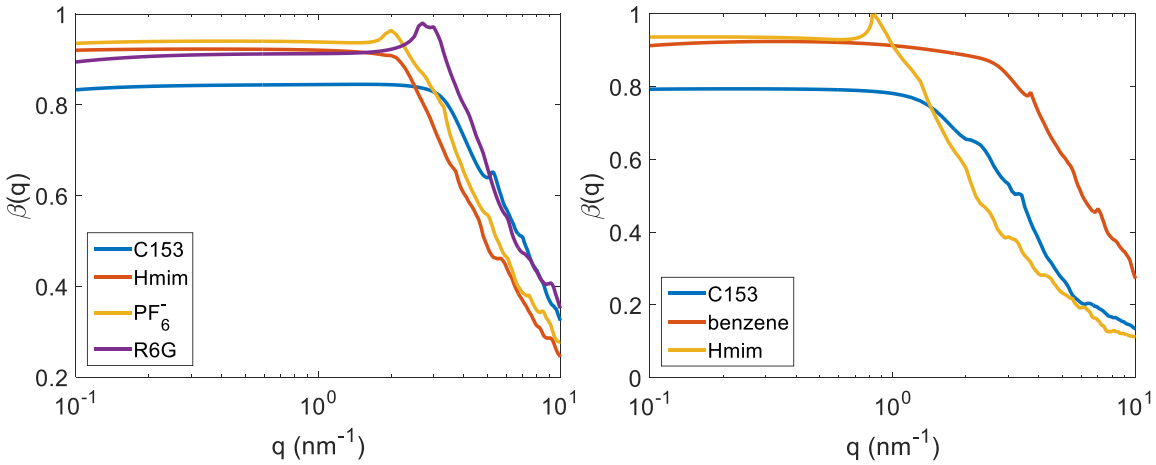

Figure 3.18. (left) $\beta(q)$ for charged probes (right) $\beta(q)$ for dipolar probes

To look at the effect of size on degree of heterogeneity, the $\beta(q)$ for all charged species and dipolar species were plotted in Figure 3.18. In both plot, the smallest probe, the dipolar benzene-like probe and anionic PF6-, showed the least heterogeneous behavior, and the largest probe, coumarin 153 for both cases, showed the most. The only species that does not follow the trend is rhodamine 6G. Rhodamine 6G, even though it is the largest species simulated, exhibited similar degrees of heterogeneity as a dipolar benzene-like probe. With a smaller probe, the diffusion is faster and the probe will be able to sample more environments within a given amount of time. On the other hand, a larger probe is more likely to be trapped within a given environment for a longer amount of time and not

sample the environment as sufficiently as a smaller probe. As a result, the larger probe is expected to exhibit a more heterogeneous dynamic.

In order to determine whether there is a relationship between size and degree of dynamic heterogeneity, a more systematic approach will be required. With only 3 different solutes, it is difficult to determine whether there is a strong correlation between size and degree of dynamic heterogeneity. A possible approach would be to use a family of aromatic model solute. (Scheme 3.2). With the molecules in the aromatic family, the correlation between radius of gyration and degree of dynamic heterogeneity can be determined.

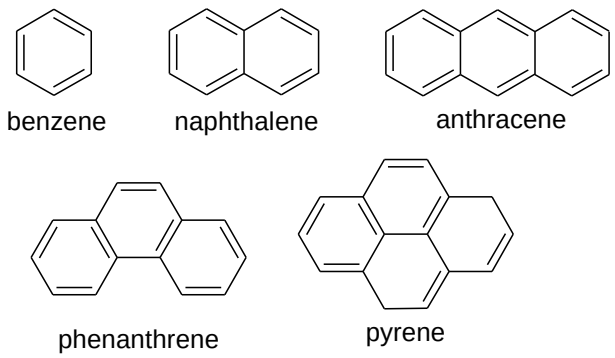

Scheme 3.2. Examples of aromatic solute that can be used to test correlation between radius of gyration and degree of dynamic heterogeneity.

To test the correlation between electric multipole moment and degrees of dynamic heterogeneity experimentally, a family of dyes having similar sizes but different electric multipole moment will be needed. One possible family is the oxazine dyes. (Scheme 3.3). Oxazine 1, Oxazine 170, and Nile Blue are all cationic, while Nile Red and resorufin are neutral. In addition to having different electric multipole moment, these dyes have

absorption maxima ranging from 532 nm to 644 nm, therefore, background from IL will not be an issue.

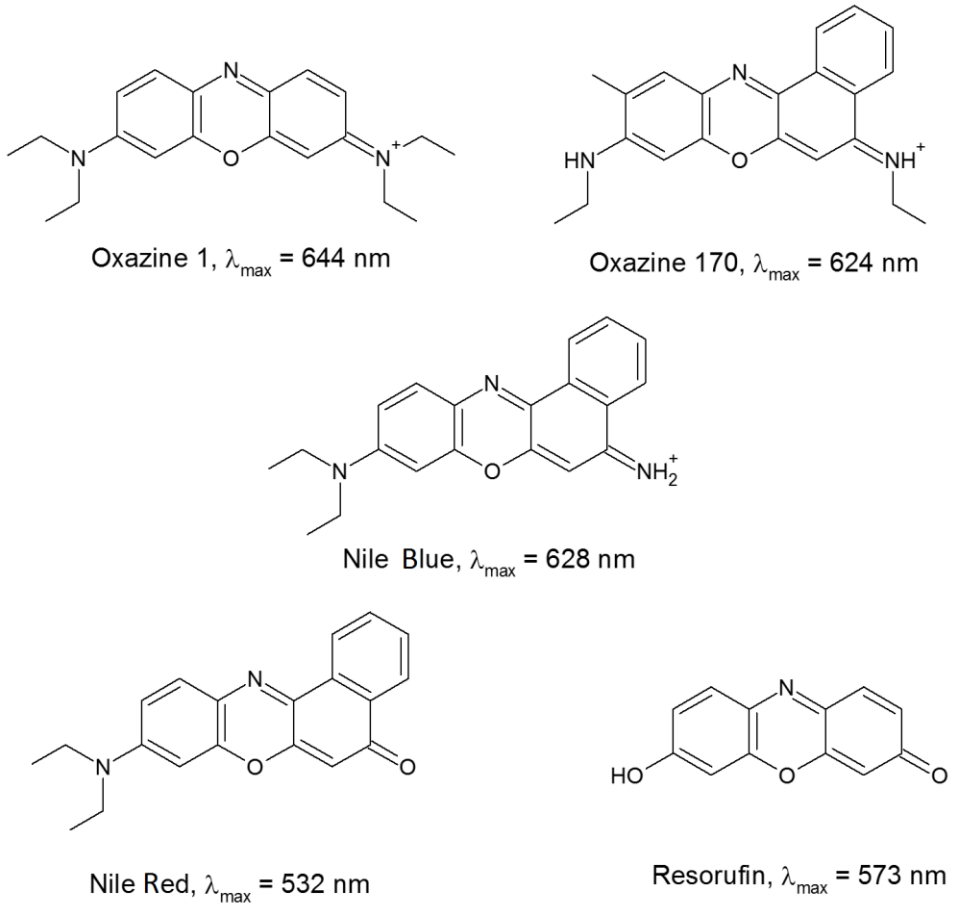

Scheme 3.3. Family of Oxazine dyes with different electric multipole moment. The absorption maxima, λ_{max} is also listed.

3.4. Conclusion

The bimodal distributions observed from dual color burst analysis indicate that ILs form structures around solutes that are heterogeneous and slow to relax. Though the FCS results can also be fit to a bimodal diffusion model, the translational dynamics of the probe

are uncorrelated to the polarity of its local environment. These two observations can be reconciled if ILs are viewed as a glassy environment in which the Stokes-Einstein relation breaks down and there is a decoupling of structural relaxation and translational dynamics.

3.5. Appendix

3.5.1. Distribution of Burst Durations

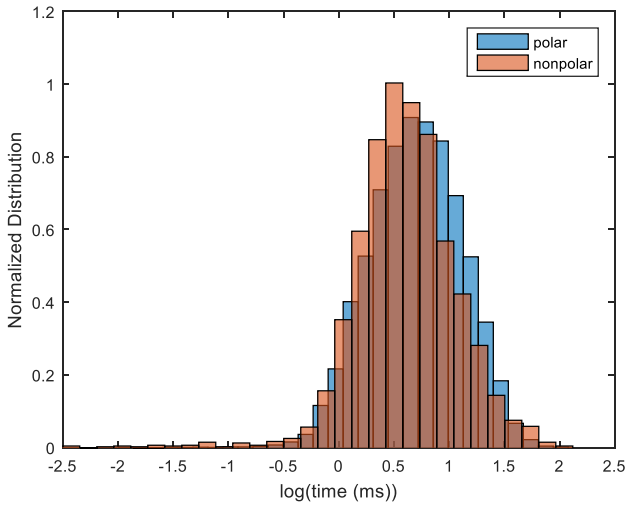

Figure A3.1. Distribution of nonpolar and polar burst durations

3.5.2. Residual Plots for FCS fitting

Figures A2 – A10 show the residual plots from FCS fitting. The residual plots show that the two-diffusion model and the anomalous diffusion model fit the FCS curves better than the simple diffusion (one-component) model. The oscillation observed in the residuals of the two-component fit and anomalous fit are from vibrations in the apparatus.

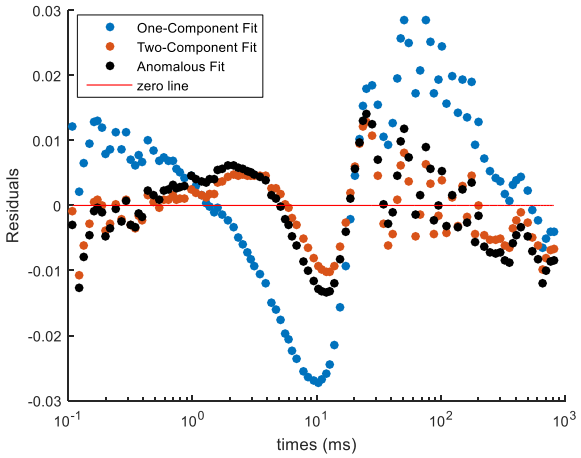

Figure A3.2. Residual plot for Nile Red in $Py_{14}^{+}Tf_2N^{-}$ with LP570.

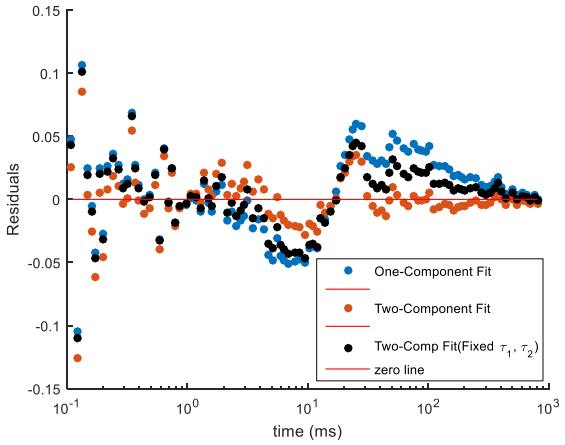

Figure A3.3. Residual plot for Nile Red in $Py_{14}^{+}Tf_2N^{-}$ with BP580±10.

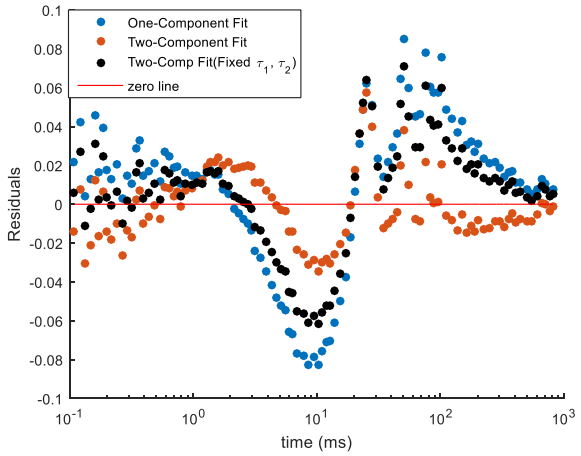

Figure A3.4. Residual plot for Nile Red in $Py_{14}^{+}Tf_2N^{-}$ with BP605±50.

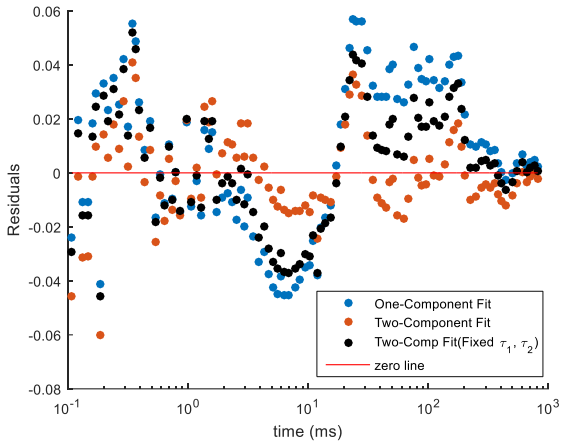

Figure A3.5. Residual plot for Nile Red in $Py_{14}^{+}Tf_2N^{-}$ with BP650±10.

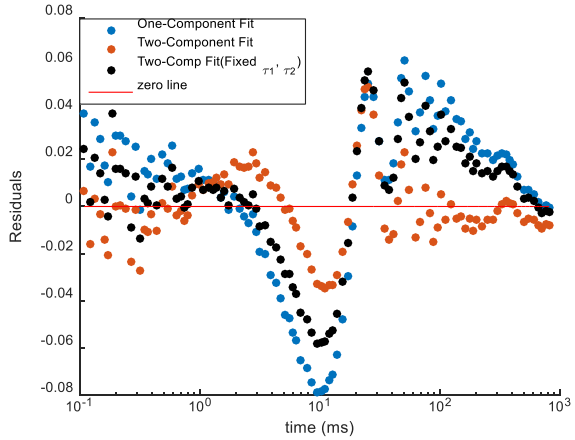

Figure A3.6. Residual plot for Nile Red in $Py_{14}^{+}Tf_2N^{-}$ with BP650±40.

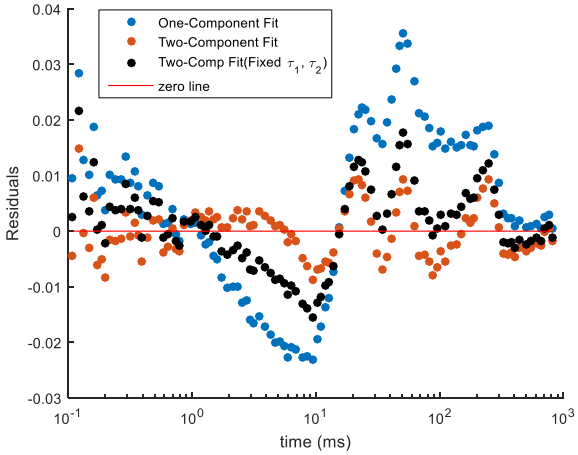

Figure A3.7. Residual plot for Nile Red in $Py_{14}^{+}Tf_2N^{-}$ with LP570+SP600.

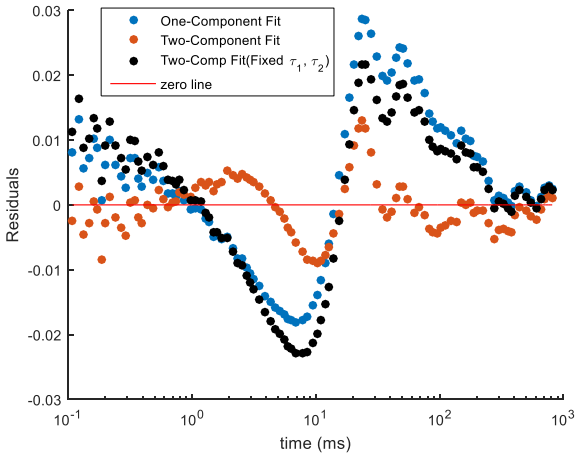

Figure A3.8. Residual plot for Nile Red in $Py_{14}^{+}Tf_2N^{-}$ with LP645.

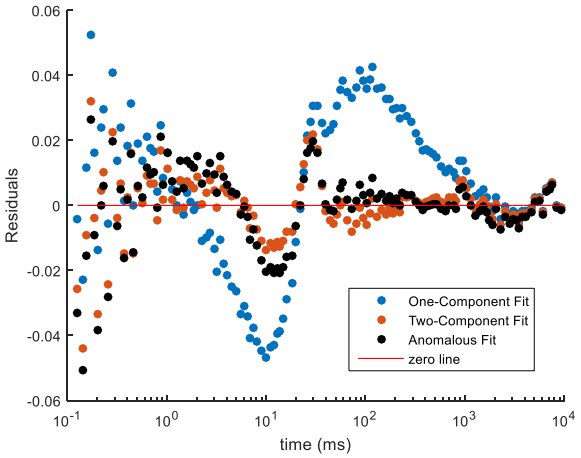

Figure A3.9. Residual plot for Nile Red in $Bmim^{+}Tf_2N^{-}$ with LP590.

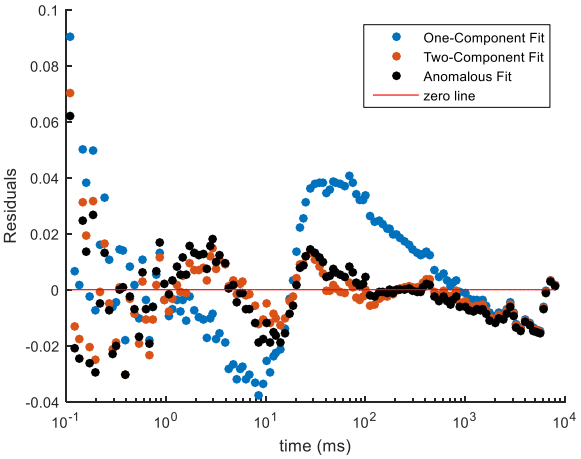

Figure A3.10. Residual plot for Nile Red in $Emim^{+}Tf_2N^{-}$ with LP590.

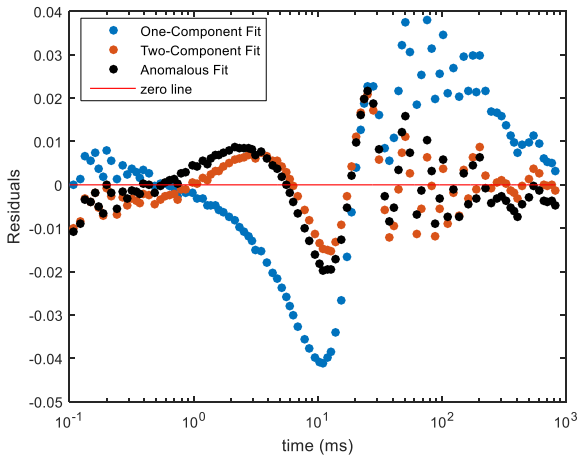

Figure A3.11. Residual plot for Rhodamine 6G in $Py_{14}^{+}Tf_2N^{-}$

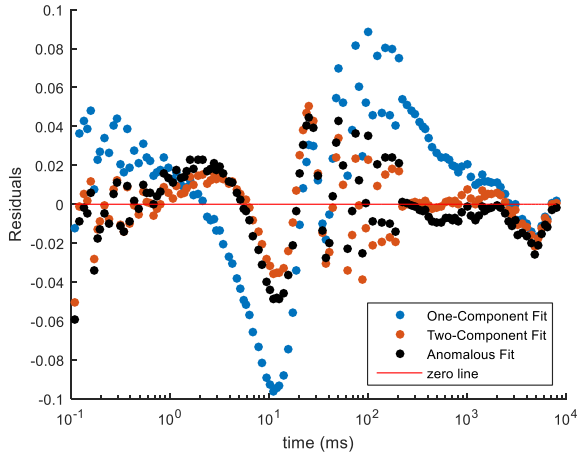

Figure A3.12. Residual plot for Rhodamine 6G in $Bmim^{+}Tf_2N^{-}$

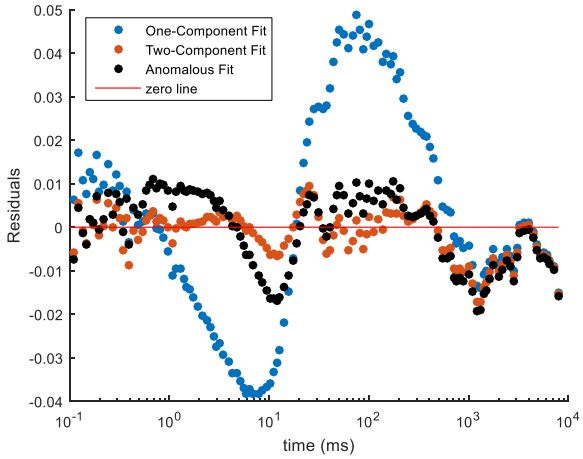

Figure A3.13. Residual plot for Rhodamine 6G in $Emim^{+}Tf_2N^{-}$

References

120. Schröder, U.; Wadhawan, J. D.; Compton, R. G.; Marken, F.; Suarez, P. A. Z.; Consorti, C. S.; de Souza, R. F.; Dupont, J. Water-Induced Accelerated Ion Diffusion: Voltammetric Studies in 1-methyl-3-[2,6-(S)-dimethylocten-2-yl]imidazolium Tetrafluoroborate, 1-butyl-3-methylimidazolium Tetrafluoroborate and Hexafluorophosphate Ionic Liquids, *New J. Chem.*, **2000**, *24*, 1009–1005.

121. Wang, Y.; Voth, G. A. Unique Spatial Heterogeneity in Ionic Liquids. *J. Am. Chem. Soc.* **2005**, *127*, 12192–12193.

122. Lopes, J. N. A. C.; Gomes, M. F. C.; Pádua, A. A. H. Nonpolar, Polar, and Associating Solutes in Ionic Liquids. *J. Phys. Chem. B*, **2006**, *110*, 16816–16818.

123. Lopes, J. N. A. C.; Pádua, A. A. H. Nanostructural Organization in Ionic Liquids. *J. Phys. Chem. B* **2006**, *110*, 3330–3335.

124. Hettige, J. J.; Kashyap, H. K.; Annapureddy, H. V. R.; Margulis, C. J. Anions, the Reporters of Structure in Ionic Liquids. *J. Phys. Chem. Lett.* **2013**, *4*, 105–110.

125. Inamura, Y.; Yamamuro, O.; Hayashi, S.; Hamaguchi, H. Dynamics Structure of a Room-Temperature Ionic Liquid bmimCl. *Phys. B Condens. Matter* **2006**, *385-386*, 732–734.

126. Yamamuro, O.; Yamada, T.; Kofu, M.; Nakakoshi, M.; Nagao, M. Hierarchical Structure and Dynamics of an Ionic Liquid 1-Octyl-3-Methylimidazolium Chloride. *J. Chem. Phys.* **2011**, *135*, 054508.

127. Triolo, A.; Russina, O.; Fazio, B.; Triolo, R.; Di Cola, E. Morphology of 1-Alkyl-3-Methylimidazolium Hexafluorophosphate Room Temperature Ionic Liquids. *Chem. Phys. Lett.*, **2008**, *457*, 362–365.

128. Annapureddy, H. V. R.; Kashyap, H, K.; De Biase, P. M.; Margulis, C. J. What is the Origin of the Prepeak in the X-ray Scattering of Imidazolium-Based Room-Temperature Ionic Liquids? *J. Phys. Chem. B*, **2010**, *114*, 16838–16846.

129. Castner Jr., E. W.; Margulis, C. J.; Maroncelli, M.; Wishart, J. F. Ionic Liquids: Structure and Photochemical Reactions. *Annu. Rev. Phys. Chem.*, **2011**, *62*, 85–105.

130. Santos, C. S.; Sanjeeva Murthy, N.; Baker, G. A.; Castner Jr., E. W. Communication: X-Ray Scattering from Ionic Liquids with Pyrrolidinium Cations. *J. Chem. Phys.*, **2011**, *134*, 121101.

131. Aragón, S.R.; Pecora, R. Fluorescence Correlation Spectroscopy as a Probe of Molecular Dynamics. *J. Chem. Phys.* **1976**, *64*, 1791–1803.

132. Rigler, R.; Mets, Ü.; Widengren, J.; Kask, P. Fluorescence Correlation Spectroscopy with High Count Rate and Low Background: Analysis of Translational Diffusion. *Eur. Biophys. J.* **1993**, *22*, 169–175.

133. Gell, C.; Brockwell, D. J.; Beddard, G. S.; Radford, S. E.; Kalverda, A. P.; Smith, D. A. Accurate Use of Single Molecule Fluorescence Correlation Spectroscopy to Determine Molecular Diffusion Times. *Single Mol.* **2001**, *2*, 177–181.

134. Moerner, W. E.; Fromm, D. P.; Methods of Single-Molecule Fluorescence Spectroscopy and Microscopy. *Rev. Sci. Instrum.* **2003**, *74*, 3597–3619.

135. Enderlein, J.; Gregor, I.; Patra, D.; Fitter, J. Art and Artefacts of Fluorescence Correlation Spectroscopy. *Current Pharmaceutical Biotechnology* **2004**, *5*, 155–161.

136. Enderlein, J.; Gregor, I.; Patra, D.; Dertinger, T.; Kaupp, U. B. Performance of Fluorescence Correlation Spectroscopy for Measuring Diffusion and Concentration. *Chem. Phys. Chem*. **2005**, *6*, 2324–2336.
137. Tcherniak, A.; Reznik, C.; Link, S.; Landes, C. F. Fluorescence Correlation Spectroscopy: Criteria for Analysis in Complex Systems. *Anal. Chem.* **2009**, *81*, 746–754.
138. Elson, E. L. Fluorescence Correlation Spectroscopy: Past, Present, Future. *Biophys. J.* **2011**, *101*, 2855–2870.
139. Guo, J.; Baker, G. A.; Hillesheim, P. C.; Dai, S.; Shaw, R. W.; Mahurin, S. M. Fluorescence Correlation Spectroscopy Evidence for Structural Heterogeneity in Ionic Liquids. *Phys. Chem. Chem. Phys.* **2011**, *13*, 12395–12398.
140. Patra, S.; Samanta, A. Microheterogeneity of Some Imidazolium Ionic Liquids as Revealed by Fluorescence Correlation Spectroscopy and Lifetime Studies. *J. Phys. Chem. B* **2012**, *116*, 12275–12283.
141. Kofu, M.; Nagao, M.; Ueki, T.; Kitazawa, Y.; Nakamura, Y.; Sawamura, S.; Watanabe, M.; Yamamuro, O. Heterogeneous Slow Dynamics of Imidazolium-Based Ionic Liquids Studied by Neutron Spin Echo. *J. Phys. Chem. B* **2013**, *117*, 2773–2781.
142. Hu, Z.; Margulis, C. J. Heterogeneity in a Room-Temperature Ionic Liquid: Persistent Local Environments and the Red-Edge Effect. *PNAS* **2006**, *103*, 831–836.
143. Hu, Z.; Margulis, C. J. Room-Temperature Ionic Liquids: Slow Dynamics, Viscosity, and the Red Edge Effect. *Acc. Chem. Res.* **2007**, *40*, 1097–1105.
144. Jeong, D.; Choi, M. Y.; Kim, H. J.; Jung, Y. J. Fragility, Stokes-Einstein Violation, and Correlated Local Excitations in a Coarse-Grained model of an Ionic Liquid. *Phys. Chem. Chem. Phys.* **2010**, *12*, 2001–2010.
145. Jeong, D.; Kim, D.; Choi, M. Y.; Kim, H. J.; Jung, Y. J. Dynamic Heterogeneity in Room-Temperature Ionic Liquids, *Ionic Liquids: Theory, Properties, New Approaches.* Kokorin, A., Ed.; InTech: China, 2011.
146. Willcox, J. A. L.; Kim, H.; Kim, H. J. A Molecular Dynamics Study of the Ionic Liquid, Choline Acetate. *Phys. Chem. Chem. Phys.* **2016**, *18*, 14850–14858.
147. Golini, C. M.; Williams, B. W.; Foresman, J. B. Further Solvatochromic, Thermochromic, and Theoretical Studies on Nile Red. *J. Fluorescence* **1998**, *8*, 395–404.
148. Carmichael, A. J.; Seddon, K. R. Polarity Study of Some 1-Alkyl-3-Methylimidazolium Ambient-Temperature Ionic Liquids with the Solvatochromic Dye, Nile Red. *J. Phys. Org. Chem.* **2000**, *13*, 591–595.
149. Fletcher, K. A.; Storey, I. A.; Hendricks, A. E.; Pandey, S.; Pandey, S. Behavior of the Solvatochromic Probes Reichardt's Dye, Pyrene, Dansylamide, Nile Red and 1-Pyrenecarbaldehyde within the Room-Temperature Ionic Liquid BmimPF6. *Green Chem.*, **2001**, *3*, 210–215.
150. Jessop, P. G.; Jessop, D. A.; Fu, D.; Phan, L. Solvatochromic Parameters for Solvents of Interest in Green Chemistry. *Green Chem.* **2012**, *14*, 1245–1259.
151. Reichardt, C. Solvatochromic Dyes as Solvent Polarity Indicators. *Chem. Rev*. **1994**, *94*, 2319–2358.
152. Zhang, K.; Yang, H. Photon-by-Photon Determination of Emission Bursts from Diffusion Single Chromophores. *J. Phys. Chem. B* **2005**, *109*, 21930–21937.
153. Wald, A. *Sequential Analysis*; John Wiley & Sons: New York, **1947**.
154. Page, E. S. Continuous Inspection Schemes. *Biometrika*, **1954**, *41*, 100–115.

155. Berendsen, H. J. C.; van der Spoel, D.; van Drunen, R. GROMACS: a Message-Passing Parallel Molecular Dynamics Implementation. *Comput. Phys. Commun.* **1995**, *91*, 43–56.
156. Lindahl, E.; Hess, B.; van der Spoel, D. GROMACS 3.0: A Package for Molecular Simulation and Trajectory Analysis. *J. Mol. Model* **2001**, *7*, 306–317.
157. Van der Spoel, D.; Lindahl, E.; Hess, B.; Groenhof, G.; Mar, A. E.; Berendsen, H. J. C. GROMACS: Fast, Flexible, and Free. *J. Comput. Chem.* **2005**, *26*, 1701–1718.
158. Hess, B.; Kutzner, C.; van der Spoel, D.; Lindahl, E. GROMACS 4: Algorithms for Highly Efficient, Load-Balanced, and Scalable Molecular Simulation. *J. Chem. Theory Comput.* **2008**, *4*, 435–447.
159. Pronk, S.; Páll, S.; Schulz, R.; Larsson, P.; Bjelkmar, P.; Apostolov, R.; Shirts, M. R.; Smith, J. C.; Kasson, P. M.; van der Spoel, D.; et al. GROMACS 4.5: A High-Throughput and Highly Parallel Open Source Molecular Simulation Toolkit. *Bioinformatics* **2013**, *29*, 845−854.
160. Jorgensen, W. L.; Maxwell, D. S.; Tirado-Rives, J. Development and Testing of the OPLS All-Atom Force Field on Conformational Energetics and Properties of Organic Liquids. *J. Am. Chem. Soc.*, **1996**, *118*, 11225–11236.
161. Canongia Lopes, J. N.; Deschamps, J.; Pádua, A. A. H. Modeling Ionic Liquids Using a Systematic All-Atom Force Field. *J. Phys. Chem. B* **2004**, *108*, 2038−2047.
162. Canongia Lopes, J. N.; Deschamps, J.; Pádua, A. A. H. Modeling Ionic Liquids Using a Systematic All-Atom Force Field. *J. Phys. Chem. B* **2004**, *108*, 11250.
163. Roy, D; Maroncelli, M. Simulations of Solvation and Solvation Dynamics in an Idealized Ionic Liquid Model. *J. Phys. Chem. B*, **2012**, *116*, 5951–5970.
164. Li, H.; Arzhantsev, S.; Maroncelli, M. Solvation and Solvatochromism in CO2-Expanded Liquids. 2. Experiment-Simulation Comparisons of Preferential Solvation in Three Prototypical Mixtures. *J. Phys. Chem. B*, **2007**, *111*, 3208–3221.
165. Shim, Y.; Choi, M. Y.; Kim, H. J. A Molecular Dynamics Computer Simulation Study of Room-Temperature Ionic Liquids. I. Equilibrium Solvation Structure and Free Energetics. *J. Chem. Phys.***, 2005**, *122*, 044510.
166. Popov, P. Steinkerchner, L. Mann, E. K. Molecular Dynamics Study of Rhodamine 6G Diffusion at *n*-Decane-Water Interfaces. *Physical Review E,* **2015**, *91*, 053308.
167. Smith, T. J.; Iglesias, W.; Mann, E. K.; Jákil, A.; Lacks, D. J. Alignment of Nematic Liquid Crystals by a Bent-Core Substrate. *Liq. Cryst.*, **2013,** *40*, 159–164.
168. Vaiana, A. C.; Schulz, A.; Wolfrum, J.; Sauer, M.; Smith, J. C. Molecular Mechanics Force Field Parameterization of the Fluorescent Probe Rhodamine 6G Using Automated Frequency Matching. *J. Comput. Chem.*, **2003,** *24*, 632–639.
169. Jorgensen, W. L.; Maxwell, D. S.; Tirado-Rives, J. Development and Testing of the OPLS All-Atom Force Field on Conformational Energetics and Properties of Organic Liquids. *J. Am. Chem. Soc.* **1996**, *118*, 11225–11236.
170. Lopes, J. N. C.; Gomes, M. F. C.; Pádua, A. A. H. Nonpolar, Polar, and Associating Solutes in Ionic Liquids. *J. Phys. Chem. B*, **2006**, *110*, 16816–16818.
171. Wang, Y.; Voth, G. A. Tail Aggregation and Domain Diffusion in Ionic Liquids. *J. Phys. Chem. B*, **2006**, *110*, 18601–18608.
172. Triolo, A.; Russina, O.; Blef, H.-J.; Di Cola, E. Nanoscale Segregation in Room Temperature Ionic Liquids, *J. Phys. Chem. B* **2007**, *111*, 4641–4644.

173. Atkin, R.; Warr, G. G. The Smallest Amphiphiles: Nanostructure in Protic Room-Temperature Ionic Liquids with Short Alkyl Groups. *J Phys Chem B* **2008**, *112*, 4164–4166.
174. Triolo. A.; Russina, O.; Fazio, B.; Triolo, R.; Di Cola, E. Morphology of 1-Alkyl-3-Methylimidazolium Hexafluorophosphate Room Temperature Ionic Liquids. *Chem. Phys. Lett.* **2008**, *457*, 362–365.
175. Turton, D. A.; Hunger, J.; Stoppa, A.; Hefter, G.; Thoman, A.; Walther, M.; Buchner, R.; Wynne, K. Dynamics of Imidazolium Ionic Liquids from a Combined Dielectric Relaxation and Optical Kerr Effect Study: Evidence for Mesoscopic Aggregation. *J. Am. Chem. Soc.* **2009**, *131*, 11140–11146.
176. Russina, O.; Triolo, A.; Gontrani, L.; Caminiti, R.; Xiao, D.; Hines Jr., L. G.; Bartsch, R. A.; Quitevis, E. L.; Plechkova, N.; Seddon, K. R. Morphology and Intermolecular Dynamics of 1-Alkyl-3-Methylimidazolium Bis{[trifluoromethane]sulfonyl}amide Ionic Liquids: Structural and Dynamic Evidence of Nanoscale Segregation. *J. Phys.: Condens. Matter*, **2009**, *21*, 424121.
177. Mizoshiri, M.; Nagao, T.; Mizoguchi, Y.; Yao, M. Dielectric Permittivity of Room Temperature Ionic Liquids: A Relation to the Polar and Nonpolar Domain Structures. *J. Chem. Phys.* **2010**, *132*, 164510.
178. Hayes, R.; Imberti, S.; Warr, G. G.; Atkin, R. Amphiphilicity Determines Nanostructure in Protic Ionic Liquids. *Phys. Chem. Chem. Phys.* **2011**, *13*, 3237–3247.
179. Znamenskiy, V.; Kobrak, M. N. Molecular Dynamics Study of Polarity in Room-Temperature Ionic Liquids. *J. Phys. Chem. B* **2004,** *108*, 1072–1079.
180. Wu, E. C.; Kim, H. J. MD Study of Stokes Shifts in Ionic Liquids: Temperature Dependence. *J. Phys. Chem. B*, **2016**, *120*, 4644–4653.
181. Shim, Y.; Duan, J.; Choi, M. Y.; Kim, H. J. Solvation in Molecular Ionic Liquids. *J. Chem. Phys.*, **2003**, *119*, 6411–6414.
182. Warshel, A. Dynamics of Reactions in Polar Solvents. Semiclassical Trajectory Studies of Electron-Transfer and Proton-Transfer Reactions. *J. Phys. Chem.* **1982,** *86*, 2218–2224.
183. Margulis, C. J.; Stern, H. A.; Berne, B. J. Computer Simulation of a "Green Chemsitry" Room-Temperature Ionic Solvent. *J. Phys. Chem. B* **2002**, *106*, 12017–12021.
184. Del Pópolo M. G.; Voth, G. A. On the Structure and Dynamics of Ionic Liquids. *J. Phys. Chem. B* **2004**, *108*, 1744–1752.
185. Cadena, C.; Zhao, Q.; Snurr, R. Q.; Maginn, E. J. Molecular Modeling and Experimental Studies of the Thermodynamic and Transport Properties of Pyridinium-Based Ionic Liquids. *J. Phys. Chem. B* **2006**, *110*, 2821–2832.
186. Maginn, E. J. Atomistic Simulation of the Thermodynamic and Transport Properties of Ionic Liquids. *Acc. Chem. Res.* **2007**, *40*, 1200–1207.
187. Andreussi, O.; Marzari, N. Transport Properties of Room-Temperature Ionic Liquids from Classical Molecular Dynamics. *J. Chem. Phys.* **2012**, *137*, 044508.
188. van Hove, L. Correlations in Space and Time and Born Approximation Scattering in Sysmtes of Interacting Particles. *Phys. Rev.* **1954**, *95*, 249–262.
189. Del Pópolo M. G.; Voth, G. A. On the Structure and Dynamics of Ionic Liquids. *J. Phys. Chem. B* **2004**, *108*, 1744–1752.
190. Araque, J. C.; Yadav, S. K.; Shadeck, M.; Maroncelli, M.; Margulis, C. J. How is Diffusion of Neutral and Charged Tracers Related to the Structure and Dynamics of a

Room-Temperature Ionic Liquid? Large Deviations from Stokes-Einstein Behavior Explained. *J. Phys. Chem. B* **2015**, *119*, 7015–7029.
191. Habasaki, J.; Ngai, K. L. Heterogeneous Dynamics of Ionic Liquids from Molecular Dynamics Simulations. *J. Chem. Phys.* **2008**, *129*, 194501.

Chapter 4. Detection of Conjugated Polymer Aggregates using Fluorescence Correlation Spectroscopy

4.1. Introduction

Due to their ability to serve as charge conductors and fluorescence emitters, conjugated polymers have found applications in organic electronics,[192] photovoltaics,[193] and electroluminescent devices.[194] The performance of devices made from conjugated polymers is critically dependent on the packing of the polymers because the optical and electronic properties are altered significantly by interchain and intrachain interactions. Aggregation has been shown to dramatically decrease the quantum yields of the polymers which severely limits the performances of the devices.[195–202] In processing, conjugated polymers are cast from solutions into a thin film. As a result, pre-aggregation in the solution directly impacts the thin film properties.[195,196,197,200,202,203,204] Traditionally, aggregation of conjugated polymers is detected using dynamic light scattering (DLS) measurements,[195,197,198] emission spectra or fluorescence lifetime measurements.[203, 205 , 206 , 207] Each technique has its limitations. For example, DLS measurements cannot detect aggregates smaller than 5nm. If the aggregates are non-emissive or have identical spectra and fluorescence lifetimes as the single chains, emission spectra and fluorescence lifetime measurements are not able to detect aggregate formation. An alternative strategy, which is sensitive to aggregation at even sub-nanomolar concentrations, is fluorescence correlation spectroscopy (FCS).[208–215] When combined with fluorescence burst analysis, the effect of inter-chain interactions and the local solvent environment on the emission of the polymer chains can be inferred.

Past studies have shown that solvent choice affects the properties of the film.[195,197,204,207,216,217] For example, Schwartz *et al.* showed that MEH-PPV adapts a more extended conformation in chlorobenzene than in tetrahydrofuran (THF) and that the extended conformation in chlorobenzene causes aggregates to form.[195] One of the common solvents used in the processing of conjugated polymers is toluene.[218,219] While it is generally believed that toluene is a "good solvent" for conjugated polymers, the π-conjugation in toluene may cause the polymers to adopt a more planar morphology[201] that is conducive to aggregation. This paper demonstrates that FCS and confocal microscopy are viable techniques for the detection of aggregation by examining whether conjugated polymers form aggregates in toluene. In addition to polymers, oligomers were also examined. Oligomers serve as useful model systems for the polymers for the larger polymers.[220–231] Oligomers and polymers should have similar interchain interactions, but oligomers have the added benefit of not having multiple chain lengths and structural defects.[232] Our results indicate that conjugated polymers form non-emissive aggregates in toluene. Many researches have tried to explain the decrease in quantum yield when conjugated polymers aggregate. Single-triplet and singlet-singlet exciton annihilation[233] or the formation of polarons[234,235,236] are possible explanations for the decrease in quantum yield. Scheblykin *et al.* proposed that MEHPPV chains could form "dark regions" when the chains are self-collapsed.[237] Vanden Bout *et al.* reported that the quantum yield of aggregate decreases in relatively polar solvent due to the stabilization of a nonradiative charge-transfer (CT) state.[238] We speculate that the non-emissive aggregates in toluene are the H-aggregate described by Kasha and Davydov,[239,240,241] which will be discussed below along with the spectroscopic results.

4.2. Experimental Methods

Both bulk and single-molecule fluorescent techniques were used to examine two different types of conjugated polymers, poly(3-hexylthiophene) (P3HT) and poly(p-phenylene vinylene) (PPV), in toluene. For PPVs, shorter chain oligomers (OPPV7 and OPPV13) were also examined. For P3HT, three different length of polymers were examined (25-mer, 50-mer, and 70-mer).

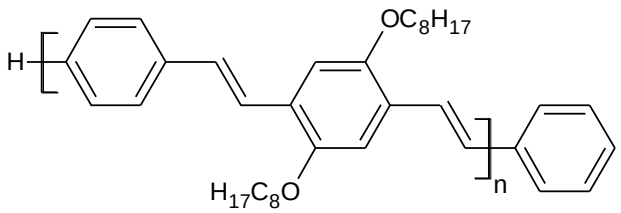

Scheme 4.1. Structure of PPV polymers. n = 3 for OPPV7 and n = 6 for OPPV13

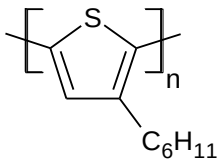

Scheme 4.2. Structure of P3HT polymers

10 μM solutions of polymers were made by the dissolving solid polymers in toluene. Solutions for FCS measurements were diluted with toluene until the concentration of the polymers was around 10 pM. Filtering was done using syringe filters having hydrophobic PTFE membranes and pore sizes of 0.20 μm (EMD Millipore). Absorption spectra and emission spectra were collected using Agilent Cary 50 Bio UV-Vis spectrometer and Jobin-Yvon FluoroMax 2, respectively.

For the confocal microscope, a 440 nm or a 485 nm pulsed diode laser (Picoquant) was the excitation source. A 1.4 NA 100x oil objective (Olympus UPlanSAPO 100x 1.4 oil) was mounted on an inverted microscope (Olympus IX-71). The pinhole placed after the microscope was 100-μm. A 50-50 beam splitter (Semrock) was placed after the pinhole to split the emission onto two single photon avalanche diodes (Micro Photon Devices PDM50). A longpass filter (475-nm for OPPV7 or 515-nm for everything else) was placed in front of the beam splitter to remove scattering. Time-tagging of the photons was done by PicoHarp 300 and PHR 800 (Picoquant). All the data were collected and analyzed using SymPhoTime software package (Picoquant).

For the total internal reflection (TIRF) microscope, the 488 nm output of an Ar-Kr laser (SpectraPhysics) was the excitation source. The images were collected using a CCD camera (Photometrics Evolve 512 EMCCD Camera). The objective mounted to the inverted IX-71 Olympus microscope was an 60x oil immersion objective with 1.4 NA (Olympus). A 515-nm longpass was placed after the microscope to remove scattering. The films are made from 10 μL of 10 μM solutions spin-casted at 3,000 rpm and dried for 30 sec. (Laurell WS-650MZ-23NPP)

FCS measures the diffusion of the fluorescent probes by monitoring the fluctuations of the photon intensities $I(t)$ in the focal volume. The FCS curve, $G(\tau)$, is calculated by cross-correlating the photon intensities of the two detectors.[214]

$$G(\tau) = \frac{\langle \delta I(t) \delta I(t+\tau) \rangle}{\langle I(t) \rangle^2} \qquad \text{(Eq. 4.1)}$$

where $\langle \ \rangle$ denotes average over the entire trajectory, and $\delta I(t)$ is the deviation from the mean photon intensity at time t.

$$\delta I(t) = I(t) - \langle I(t) \rangle \qquad \text{(Eq. 4.2)}$$

If the focal volume is assumed to have a three-dimensional Gaussian shape, the FCS curve is fitted to[8]

$$G(\tau) = \frac{1}{N}\sum_{i=1}^{n} a_i \left(1 + \frac{\tau}{\tau_{D_i}}\right)^{-1} \left(1 + \frac{1}{\omega^2}\left(\frac{\tau}{\tau_{D_i}}\right)\right)^{-\frac{1}{2}} \quad \text{(Eq. 4.3)}$$

where N is the average number of molecules in the focal volume, n is the number of species, a_i is the contribution of the *i*th species, τ_{D_i} is the characteristic residence time for the *i*th species, and ω characterizes the dimension of the focal volume. The diffusion coefficient of the *i*th species, D_i, can calculated from τ_{D_i} by[8]

$$\tau_{D_i} = r_0/4D_i \quad \text{(Eq. 4.4)}$$

4.3. Results and Discussions

4.3.1. TIRF Images of Films

Unfiltered and filtered 10 μM solutions of P3HT 25 and MEH-PPV in toluene were spun on glass slides and their fluorescence were captured with the TIRF microscope. The TIRF image of the films and the distribution of pixel intensities are presented in Figures 4.1 and 4.2.

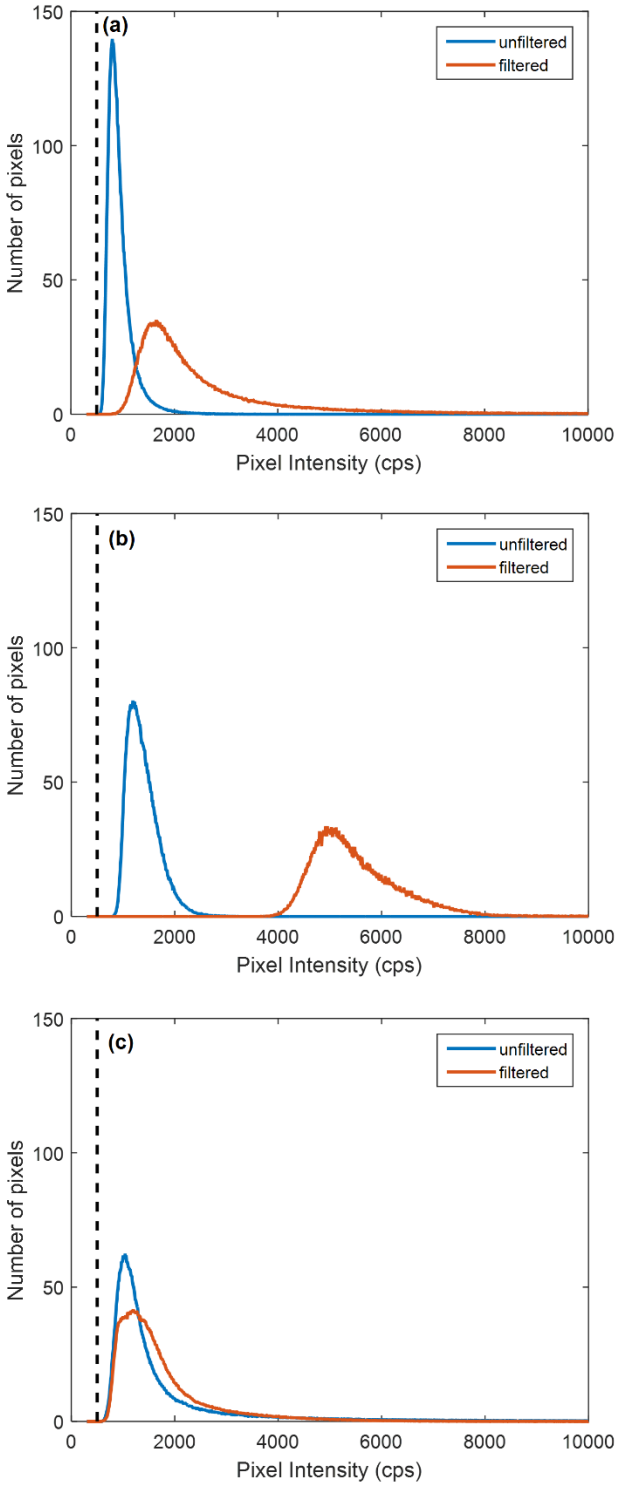

Figure 4.1. Distribution of pixel intensities for (a) P3HT 25 in toluene, (b) MEHPPV in toluene, and (c) MEHPPV in THF. The black dash line represents the background noise level of the camera.

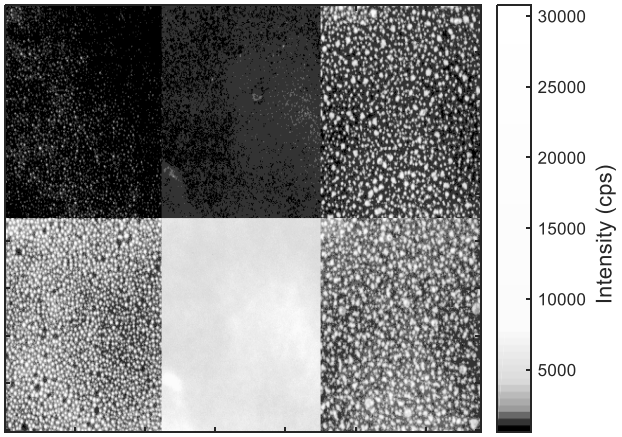

Figure 4.2. TIRF image of (a) P3HT25 in toluene unfiltered, (b) P3HT 25 in toluene filtered, (c) MEHPPV in toluene unfiltered, (d) MEHPPV in toluene filtered, (e) MEHPPV in MeTHF unfiltered, and (f) MEHPPV in MeTHF filtered. The dark level of the range is set at 600 cps, which is higher than the background noise level of the camera.

Even though absorbance measurements (not shown) showed that filtering removes about 1 to 10% of conjugated polymers, the film made from filtered solutions were up to five times brighter than those made form unfiltered solutions. For comparison, films made from THF did not show an increase in brightness after filtering (Figure 4.1c).

The poor quality of the unfiltered film could be caused by aggregates in the solution, because many studies have shown that aggregates have lower quantum yield.[195–202] Furthermore, past studies have shown that average energy transfer length in bulk conjugated materials ranges from 5 nm to 10 nm.[217,242–247] Therefore, low-quantum-yield aggregates would serve as energy traps, quench large area of the films, lower the overall brightness of the films, and make the films appear less uniform. To determine whether conjugated polymers aggregate in toluene, the diffusion rates, emission spectra, and fluorescence lifetimes of the filtered and unfiltered solutions were examined.

4.3.2. Diffusion, Emission Spectra, and Fluorescence Lifetime Measurements

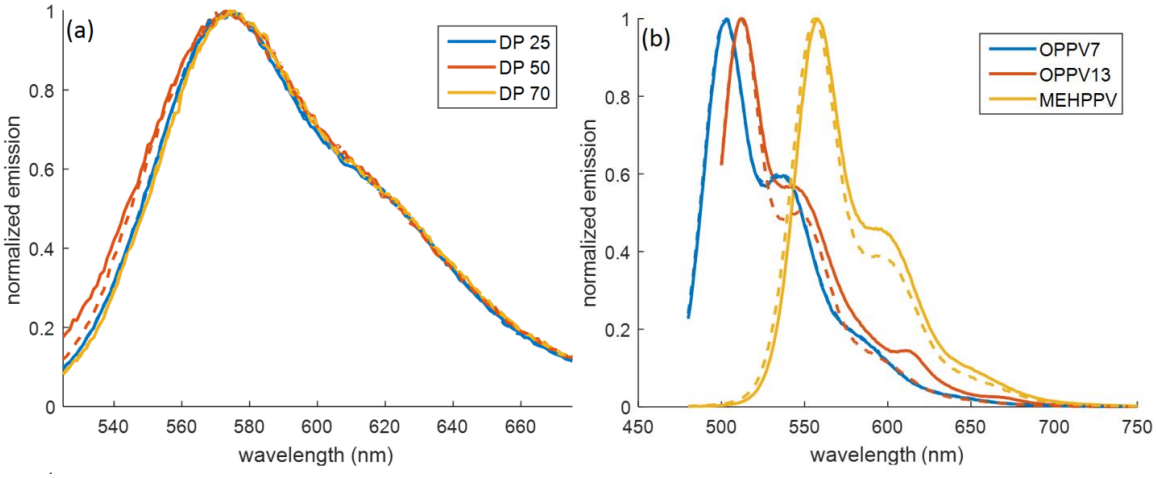

Figure 4.3. Normalized emission spectra of (a) P3HTs and (b) PPVs excited at 465 nm. (–) unfiltered sample and (- -) filtered sample.

The emission spectra and the absorption spectra (not shown) of P3HT and PPV (Figure 4.3) did not show significant changes between the pre-filtered and post-filtered samples. Past studies have shown that the emission spectra of aggregated P3HTs and PPVs show a significant redshift of λ_{max}.[198,200] In addition to the redshift of λ_{max}, the relative intensities of the 0-0 band to the other vibronic features differ significantly between single chains and aggregates.[198,200] If the pre-filtered solution were to contain aggregates, a change in the shape of the emission spectra would be expected. The similarity of the unfiltered and filtered spectra suggests either that the P3HTs and PPVs chains do not aggregate in toluene or the aggregates formed are not emissive. Next, we examined the fluorescence lifetimes.

Typically, changes in the fluorescence lifetime indicate the presence of aggregates. For example, if the aggregates form excimers, the fluorescence lifetime typically increases due to the diminished transition moment to the ground state.[248] The fluorescence lifetime

could also decrease if the aggregates form low-energy dark states that cause an increase in nonradiative decay rate.[198,249,250] In none of the samples studied was the fluorescence lifetime significantly impacted by filtration (See Appendix). For the PPVs, and P3HT 50, the small differences between fitted parameters could be attributed to fitting and random errors from the measurements. For P3HT 25 and P3HT 70, a small increase in the average fluorescence lifetimes was observed. The amplitude of the long component slightly increased, which caused the averaged lifetime to increase. Even though a slight increase in average lifetime could indicate that filtering removed aggregates has a low-energy dark state, the short lifetime component is not affected. Overall, these results suggest that fluorescence lifetime measurements cannot unambiguously determine whether aggregation has occurred in these samples.

Neither the emission spectra nor the fluorescence lifetimes showed significant changes due to filtration. If aggregates were present and emissive, we would expect to see the emission spectra and fluorescence lifetime to change significantly due to the removal of aggregates by filtering. Therefore, these measurements suggested that either there were no aggregates in toluene solution or that the aggregates were non-emissive. As TIRF results suggested aggregation, which contradict results from emission spectra and fluorescence lifetimes, confocal microscopy was used to examined the unfiltered and filtered solutions.

4.3.3. Confocal Microscopy and Fluorescence Correlation Spectroscopy

First, the fluorescent intensities of the polymers and oligomers were measured using the confocal microscope. The average intensities were calculated by totaling the

number of photons collected by both detectors over a 5-minute period. The average intensities were corrected for background by subtracting the average intensity of toluene.

For all six polymers and oligomers studied, the intensities increased after filtering (Table 3), which matched the TIRF results. In addition, as the length of the chain increased, the ratio of the intensities before and after filtering, $\langle I_{\text{filtered}} \rangle / \langle I_{\text{unfiltered}} \rangle$, generally increased. There are two possible explanations for their increase. It could be caused by an increase in quantum yield or by an increase in the number of emitters. In the first scenario, filtering causes the chains to adopt conformations that have higher quantum yields. In the second scenario, filtering breaks up aggregates that resulted in more single chains. To distinguish between the two scenarios, we turned to FCS.

Table 4.1. Fluorescent intensities of P3HT polymers, MEH-PPV, and PPV oligomers measured with confocal microscope.

	$\langle I_{\text{filtered}} \rangle / \langle I_{\text{unfiltered}} \rangle$
P3HT 25	1.51 ± 0.03
P3HT 50	1.4 ± 0.1
P3HT 70	2.5 ± 0.4
OPPV 7	1.31 ± 0.08
OPPV 13	1.46 ± 0.07
MEH-PPV	3.6 ± 0.5

Two different aspects of FCS are useful in detecting aggregation: the normalized FCS curve and $G(0)$. First, the normalized fitted FCS curves were measured (Figure 4 and

SI). For all 6 samples, the decay rate of the FCS curves corresponding to the filtered solutions are the same as, or slightly faster than, those of the unfiltered solutions. If emissive aggregates were present prior to filtration the FCS curves of filtered solution would decay significantly more quickly than would those of the pre-filtered solutions. This is seen in the case of OPPV13 in a 30%/70% THF-acetonitrile mixture (Figure 4), a solvent pair in which OPPV13 forms emissive aggregates. The FCS curve obtained for this sample decays significantly more slowly than that corresponding to monomeric OPPV13 in THF, even though the viscosity of the mixture is similar to that of THF and toluene. Moreover, all of the FCS curves can be reasonably fitted with a single characteristic residence time, τ_D. If emissive aggregates are present, two or more characteristic residence times should be required for fitting. Overall, these results demonstrate that the shape of the FCS decay curve is sensitive to the presence of *emissive* aggregates while the $G(0)$ value may be used to infer the presence of non-emissive species.

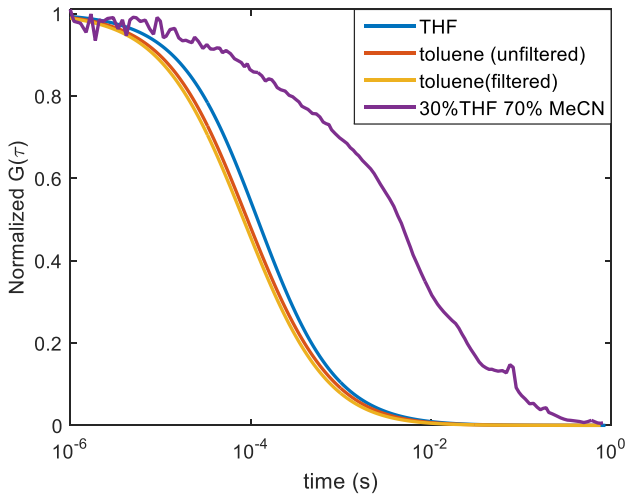

Figure 4.4. Normalized FCS curves of OPPV13 in THF, toluene (unfiltered and filtered), and 30% THF/70% acetonitrile mixture.

At $\tau = 0$, Eq. 4.1 becomes $G(0) = 1/N$, which means $G(0)$ is inversely proportional to the number of emitter, $\langle N \rangle$, in the focal volume, *i.e.* larger $G(0)$ means there are fewer emitters in the focal volume. Furthermore, the brightness of the molecule can be calculated by multiplying the average intensity with $G(0)$.

$$B \text{ (Brightness per molecule)} = \langle I \rangle G(0) = \frac{\langle I \rangle}{\langle N \rangle} \qquad \text{(Eq. 4.5)}$$

If the quantum yields of the emitters increase, the brightness per molecule would increase. If filtering breaks up aggregates into single chains, the number of emitters would increase. The FCS curves are shown in Figure 4.5, and $G(0)$ and brightness per molecule are tabulated in Tables 4.2 and 4.3.

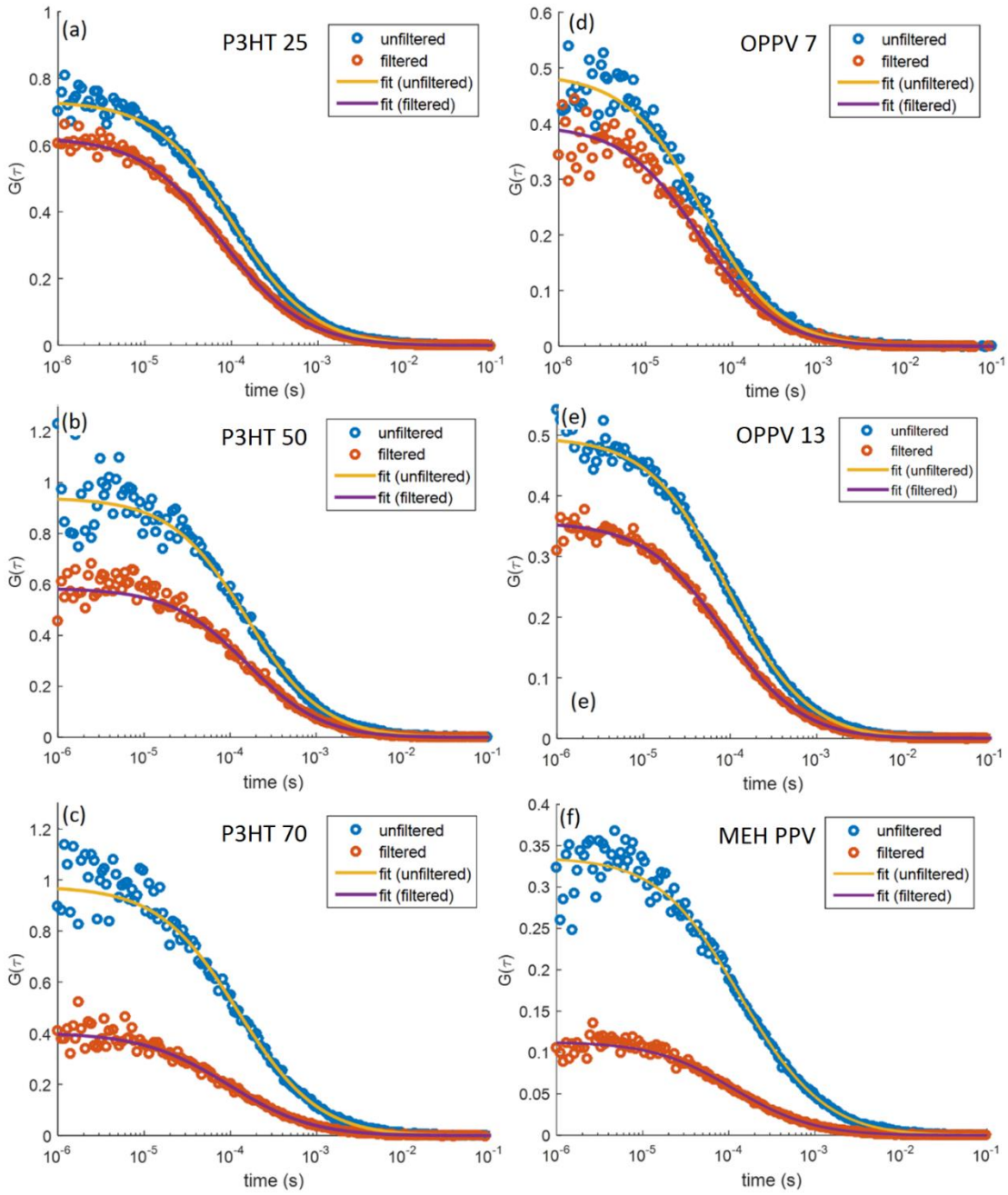

Figure 4.5. FCS of filtered and unfiltered polymers in toluene. The left side displays the result for the P3HT polymers and the right side displays the result for the PPV polymers/oligomers. The top panels correspond to the shortest chains, and the bottom panels to the longest chains. (a) P3HT 25 (b) P3HT 50 (c) P3HT70 (d) OPPV7 (e) OPPV13 (f) MEH-PPV.

Table 4.2. $G(0)$ of PPV and P3HT

	$G_{\text{unfiltered}}(0)$	$G_{\text{filtered}}(0)$	$\frac{G_{\text{filtered}}(0)}{G_{\text{unfiltered}}(0)}$	$\frac{\langle N\rangle_{\text{filtered}}}{\langle N\rangle_{\text{unfiltered}}}$
P3HT 25	0.73 ± 0.02	0.62 ± 0.02	0.86 ± 0.04	1.18 ± 0.05
P3HT 50	0.94 ± 0.07	0.59 ± 0.02	0.62 ± 0.05	1.6 ± 0.1
P3HT 70	0.97 ± 0.10	0.40 ± 0.03	0.42 ± 0.05	2.4 ± 0.3
OPPV7	0.49 ± 0.03	0.40 ± 0.02	0.82 ± 0.06	1.2 ± 0.1
OPPV13	0.25 ± 0.01	0.17 ± 0.01	0.68 ± 0.05	1.5 ± 0.1
MEH-PPV	0.34 ± 0.04	0.11 ± 0.01	0.34 ± 0.05	3.0 ± 0.5

Table 4.3. Counts per molecule of PPV and P3HT

	$B_{\text{unfiltered}}$[a]	B_{filtered}[a]	B_{filtered} / $B_{\text{unfiltered}}$
P3HT 25	1310 ± 30	1680 ± 70	1.28 ± 0.06
P3HT 50	1120 ± 60	960 ± 50	0.86 ± 0.06
P3HT 70	1040 ± 60	1070 ± 60	1.03 ± 0.08
OPPV7	850 ± 20	890 ± 50	1.04 ± 0.06
OPPV13	1620 ± 70	1600 ± 80	0.98 ± 0.06
MEH-PPV	1240 ± 80	1000 ± 50	0.81 ± 0.07

[a] in cps (counts per second) per emitter

For all six P3HTs and PPVs, $G(0)$ decreased after filtering indicates that the average number of emitters in the focal volume increased. Since $\langle I\rangle$ increased and $G(0)$ decreased as the length of the chain increased, the brightness of the emitters was not

affected by filtering. This showed that the quantum yield of the emitter is not affected by filtering. As discussed earlier, the increase in the number of emitters suggested that filtering is breaking aggregates into smaller aggregates or single chains.

We briefly discuss how changes in $G(0)$ and brightness per emitter can be used to infer the effects of filtering. First, if the individual chains are well solvated and exist as individual chains in solution, or if the chains form stable small aggregates that are less than the pore size of the filters, filtering would have no effect on the chains. In this situation, both $G(0)$ and brightness per emitter would be the same before and after filtering. For example, for OPPV13 and P3HT25 in good solvents, such as 2-methylhydrofuran (MeTHF), filtering has no effect on the brightness per emitter and $G(0)$ (Figure 4.6).

Second, if the solvent forces the chain to be in a thermodynamically metastable state that has lower quantum yield, such as the self-collapsed conformation with large torsional strains,[199,237, 251] filtering could cause the chains to relax to a more stable conformation with higher quantum yield. In this situation, since the number of emitters stays constant, $G(0)$ would not change, but brightness per emitter would increase to reflect the change in quantum yield. Third, if the chains form large emissive aggregates that are removed by the filters, $G(0)$ would increase, because the number of emitters decreases. Lastly, if the filters break up weakly bonded aggregates into smaller aggregates or single chains, $G(0)$ would decrease due to the increase in the number of emitters.

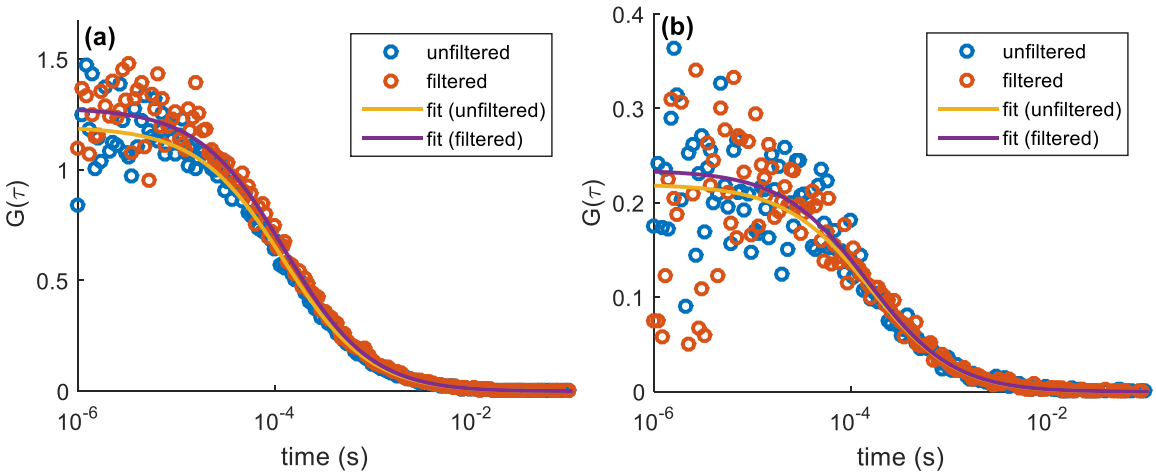

Figure 4.6. FCS of filtered and unfiltered (a) OPPV13 and (b) P3HT 25 in MeTHF.

As the length of the polymers increased, the ratio $\langle N \rangle_{\text{filtered}} / \langle N \rangle_{\text{unfiltered}}$ also increased. The trend suggested that longer chains are more likely to form aggregates than the shorter polymers. There are two reasons that could explain this trend. First, longer chains will have stronger interchain dispersion interactions. Second, if the solvent-chain interactions are unfavorable, longer chains will have more unfavorable chain-solvent interactions. These two factors combine to cause longer chains to aggregate more easily than shorter chains.

There are two possible explanations for the fact that the brightness of the emitters does not change before and after filtering. First, the aggregates are non-emissive. Second, the aggregates have the same quantum yield as the single chains. If the aggregates are emissive, but have a different quantum yield, the brightness per emitter of the pre-filtered solution would be the weighted average of the brightness of the aggregates and the single chains. Earlier discussions showed that the diffusion rates, emission spectra, and fluorescence lifetimes are not affected by filtering. If the aggregates have the same

quantum yields as the single chain, significant changes in diffusion rates, emission spectra, and fluorescence lifetimes should be observed. Therefore, the aggregates formed in toluene are not emissive.

To confirm the results from FCS, the distributions of photon per burst were analyzed (Figure 7). If the number of emitter increases, the number of bursts should increase but the shape of the distribution should be the same. On the other hand, if the quantum yield of the emitter changes, the shape of the distribution should be different. The bursts were harvested using thresholding and the SymphoTime software. The filtered solutions exhibited more number of bursts than the unfiltered solutions even though the solutions had the same concentrations and the measurements were performed over the same amount of time. Even though the number of bursts increased, the two distributions are nearly identical. These two observations suggested that the increase in intensity post-filtering is due to an increase in the number of emitters, and not a change in the quantum yield, which confirms the FCS results. Furthermore, the number of bursts increased by 26%, which is close to the increase in the number of emitter measured in FCS (Table 4.2).

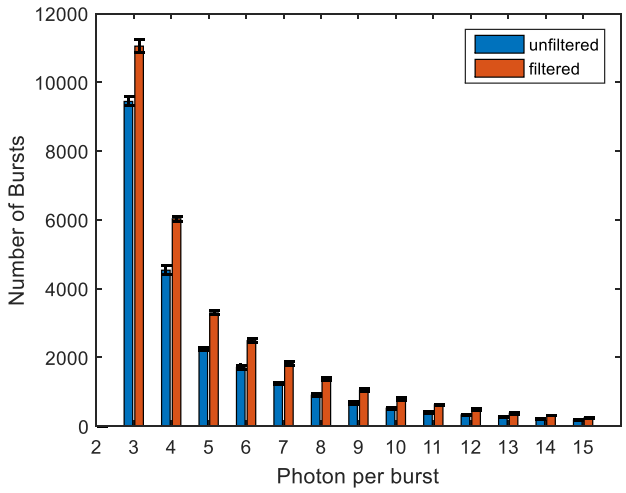

Figure 4.7. Distribution of photons per burst for unfiltered and filtered P3HT 25 in toluene over 1hr.

We briefly speculate on the type of aggregate formed in toluene. Using two coupled chains as the model, there two different types of aggregates are categorized based on whether the two molecular transition moments aligned in-phase (J-aggregate) or out-of-phase (H-aggregate).[239,252,253,254] J-aggregates have red-shifted absorption spectra, and strong emission, while H-aggregates have blue-shifted absorption and weak emission. In the H-aggregate, the 0-0 transition is symmetry forbidden.[200,239,255] The π-π interactions between toluene and the conjugated polymers potentially make the conjugated polymers adopt a planar conformation which is conducive to forming the well-ordered weakly-emissive H-aggregates. As a result of interaction with the solvent, the H-aggregates observed in toluene are likely more ordered and less emissive than the H-aggregates observed in other solvents. Another possibility is that conjugated polymers form weakly-emissive excimers in the unfiltered solution. The planarization of the conjugated polymer by toluene could favor the formation of excimers. Due to the forbidden radiative transition

to the ground state, excimers also have a weak oscillator strength to the ground state, and their lifetimes are typically longer than that of the single chain.[222,230,231,248,256–259] The formation of excimers in the unfiltered solution could explain why the lifetime of unfiltered P3HT25 and P3HT70 exhibit a slightly longer long-component than the filtered samples. (Figures A4.1 – A4.6)

Finally, we will briefly discuss how the presence of aggregate would affect FCS curve with some theoretical calculations. To account for the size of the aggregate, the Stokes-Einstein equation predicts that the diffusion constant is inversely proportional to the hydration radius of the diffusion species.

$$D_1 = \left(\frac{R_2}{R_1}\right) D_2 \qquad \text{(Eq. 4.6)}$$

Therefore, combining Eq. 4 and Eq. 6, the ratio of characteristic resident times are

$$\tau_{D,1} = \left(\frac{R_2}{R_1}\right) \tau_{D,2} \qquad \text{(Eq. 4.7)}$$

When the quantum yields of the diffusion species are different, the contribution of the *i*th species, a_i, is[260]

$$a_i = \frac{N_i q_i^2}{\sum N_i q_i^2} \qquad \text{(Eq. 4.8)}$$

Therefore, the relative contribution of the two species with different quantum yield is

$$\frac{a_i}{a_j} = \frac{N_i q_i^2}{N_j q_j^2} \qquad \text{(Eq. 4.9)}$$

To examine how the presence of aggregates in OPPV13 solution would affect the FCS curves, we assumed that OPPV13 is fully extended in solution. The length of a fully-extended OPPV13 chain, calculated using averaged bond length, is 8.3 nm. With these assumptions, the theoretical FCS curve is

$$G(\tau) = \frac{1}{N}\left\{\frac{a_1}{\left(1+\frac{\tau}{\tau_D}\right)\sqrt{1+\omega^2\left(\frac{\tau}{\tau_D}\right)}} + \frac{a_2}{\left[1+\frac{\tau}{(R_a/8.3)\tau_D}\right]\sqrt{1+\omega^2\left[\frac{\tau}{(R_a/8.3)\tau_D}\right]}}\right\}$$

(Eq. 4.10)

where the first term in the sum is the contribution from single chain, and the second term is the contribution from the aggregates of size R_a. For filtered OPPV13, $N = 1, \tau_D = 0.0005755$ s, and $\omega = 13.9$.

To examine the how having emissive aggregate would affect the FCS curves, we assume $R_a = 200$ nm, which is the smallest aggregate that would be broken up by the filter, and also the largest aggregate that could pass through the filter. These would represent the worst case scenario, where the aggregates in the unfiltered solutions are as small as they could be or the aggregates in the filtered solutions are as large as they could be.

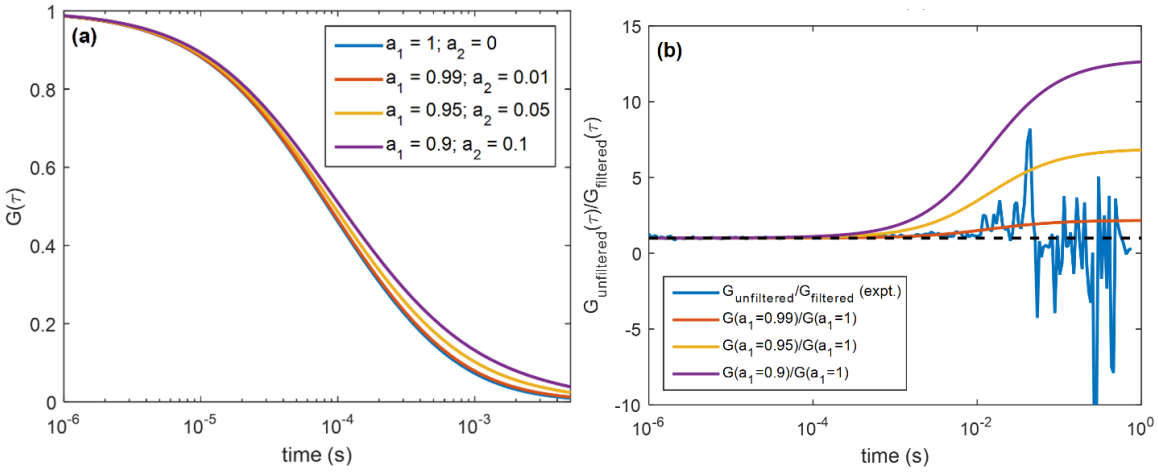

Figure 4.8. Computed FCS curve for 200-nm aggregates of OPPV13 in toluene.

Figure 4.8a shows the calculated FCS curves with different a_1 and a_2. The curve with $a_1 = 1$ is the FCS curve with no aggregates, which represents the curve after filtering.

The curves with $a_1 = 0.99, 0.95,$ and 0.9 would represent FCS with some 200-nm aggregates, which represent the curves before filtering. To compare these theoretical curves with the experimentally-measured curves, the ratios of the unfiltered and filtered curves, ($G_{unfiltered}(\tau)/G_{filtered}(t)$, are plotted in Figure 4.8b. From the figure, the experimental curve matches $G(a_1 = 0.99)/G(a_1 = 1)$ the best, which means that if the aggregates from the unfiltered solutions are emissive, $a_1/a_2 = 99$, and

$$\frac{N_{\text{single chain}} q^2_{\text{single chain}}}{N_{\text{aggregate}} q^2_{\text{aggregate}}} = 99$$

Therefore, if $N_{\text{single chain}} \approx N_{\text{aggregate}}$, the quantum yield of the single chains are 10 times larger than the quantum yield of the aggregate, or if $q_{\text{single chain}} \approx q_{\text{aggregate}}$, there are 100 times more single chains than aggregates.

Overall, the analysis showed that in the worst case scenario, either the aggregates are 10 times less emissive than the single chains or the number of aggregates are 100 times less than the number of single chains. However, it is important to note that unlike the calculated ratio, the experimental ratio did not curve upward at long time limit. The calculated ratios curve upward, because of the large aggregates. Since the experimental ratio stayed around 1 at the long time limit, it is more likely that no large aggregates were detected by FCS.

4.5. Conclusion

Filtering of two different types of conjugated polymers, P3HT and PPV, in toluene with 0.20-μm filters caused the fluorescent intensities to increase and $G(0)$ to decrease. However, brightness per emitter, diffusion rates, emission spectra, and fluorescent

lifetimes are not affected by filtering. These observations suggest that filtering breaks up weakly-bonded non-emissive aggregate into single chains and the increase in fluorescence intensity is caused by the increase in the number of emitters and not by the increase in the quantum yield of the chains. As a result of breaking the aggregates in solution, the films made from filtered solutions are brighter and more uniform than the unfiltered solutions.

Past studies of conjugated polymers in toluene have emphasized that freshly prepared conjugated polymers in toluene are used in their analysis.[199,201] The presence of these aggregates could be the cause why freshly prepared samples are important in the processing of these materials. These aggregates could serve as nucleation sites for irreversible aggregation that degrades the quality of the conjugated polymer solutions. The results from this paper suggest that in order to store conjugated polymers in toluene for an extended period of time, the solutions need to be filtered regularly to break up the aggregates.

4.6 Appendix

4.6.1. Fluorescence Lifetime

The fluorescence lifetimes of PPVs and P3HTs were measured and tabulated in Table S1. The average lifetimes, τ_{avg}, are the amplitude average lifetime. The amplitude average lifetimes were calculated by[261]

$$\tau_{\text{avg}} = \frac{\sum a_i \tau_i}{\sum a_i} \qquad \text{(Eq. A4.1)}$$

where a_i and τ_i are the amplitude and the lifetime of the *i*th component, respectively.

Table A4.1. Fluorescence lifetimes of P3HT and PPV polymers.

	Unfiltered				Filtered			
	τ_1 [a]	τ_2 [a]	A_1 [b]	τ_{avg} [a]	τ_1 [a]	τ_2 [a]	A_1 [b]	τ_{avg} [a]
P3HT 25	0.47	4.9	98	0.56	0.50	3.3	89	0.81
P3HT 50	0.57	6.3	99	0.62	0.59	3.9	96	0.72
P3HT 70	0.57	3.9	89	0.94	0.71	3.9	80	1.3
OPPV 7	0.73	1.8	94	0.79	0.74	2.2	91	0.87
OPPV 13	0.53	1.4	76	0.56	0.56	1.6	79	0.78
MEH-PPV	0.44	1.4	93	0.47	0.47	1.5	90	0.57

[a] in ns. [b] in %.

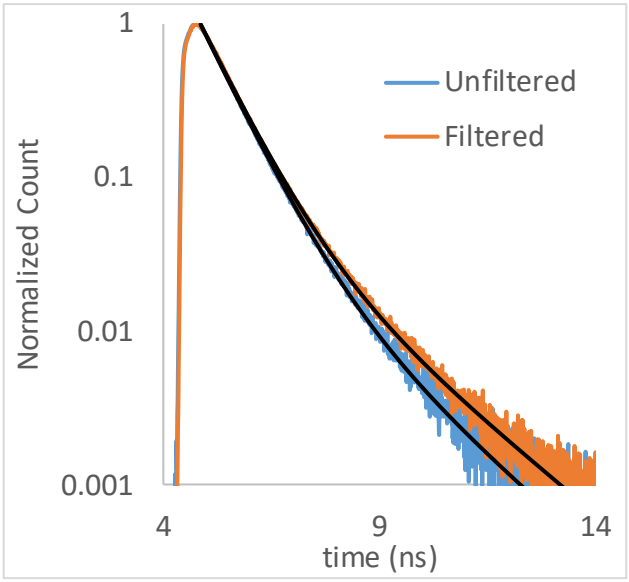

Figure A4.1. Fluorescence lifetime of unfiltered and filtered OPPV7 in toluene.

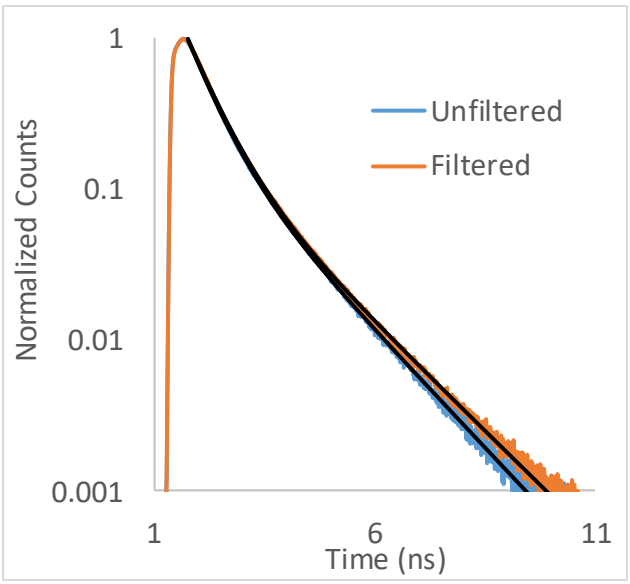

Figure A4.2. Fluorescence lifetime of unfiltered and filtered OPPV13 in toluene.

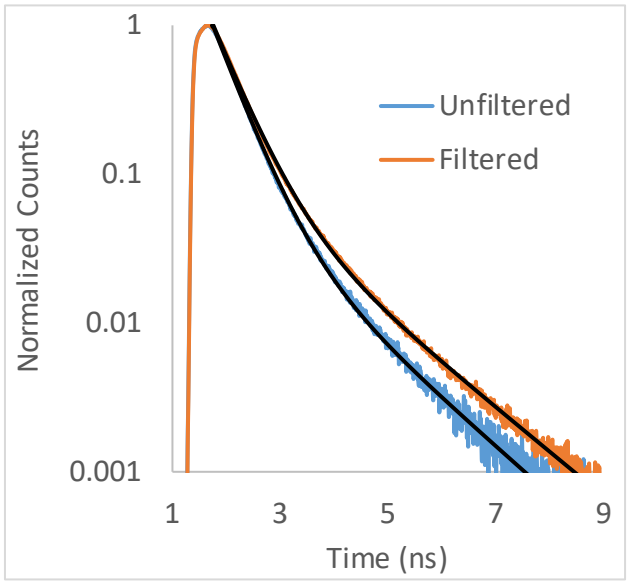

Figure A4.3. Fluorescence lifetime of unfiltered and filtered MEH-PPV in toluene.

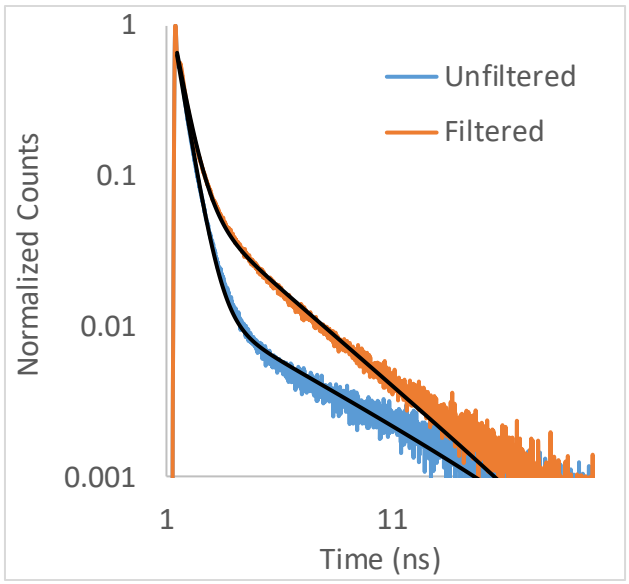

Figure A4.4. Fluorescence lifetime of unfiltered and filtered P3HT DP25 in toluene.

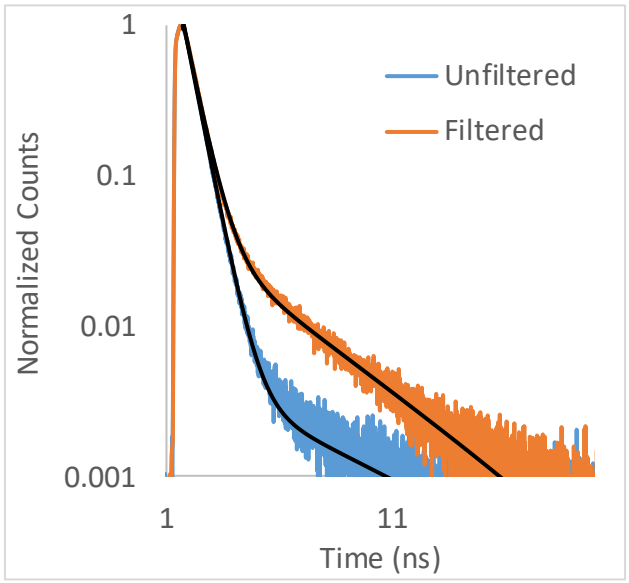

Figure A4.5. Fluorescence lifetime of unfiltered and filtered P3HT DP50 in toluene.

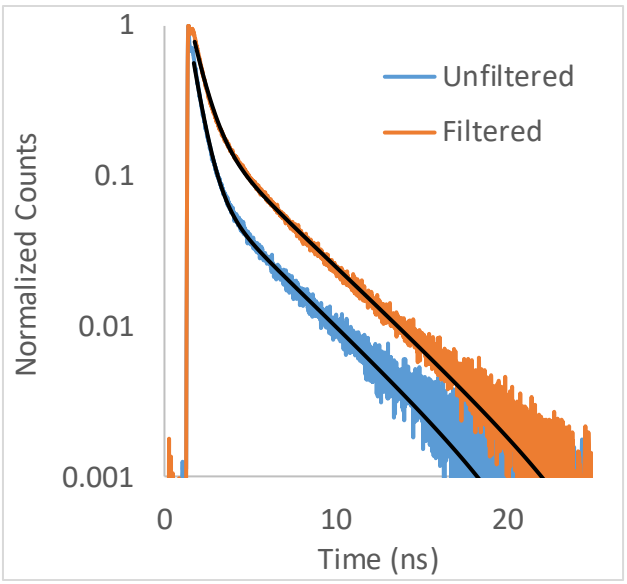

Figure A4.6. Fluorescence lifetime of unfiltered and filtered P3HT DP75 in toluene.

4.6.2. Normalized FCS Curves

The normalized FCS curves of PPVs and P3HTs are presented below.

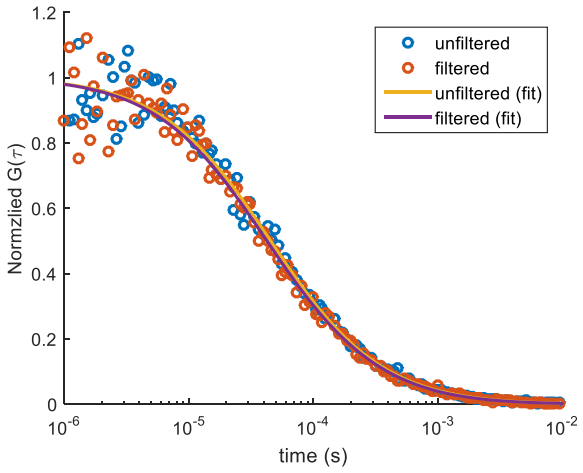

Figure A4.7. Normalized FCS curves for unfiltered and filtered OPPV7 in toluene.

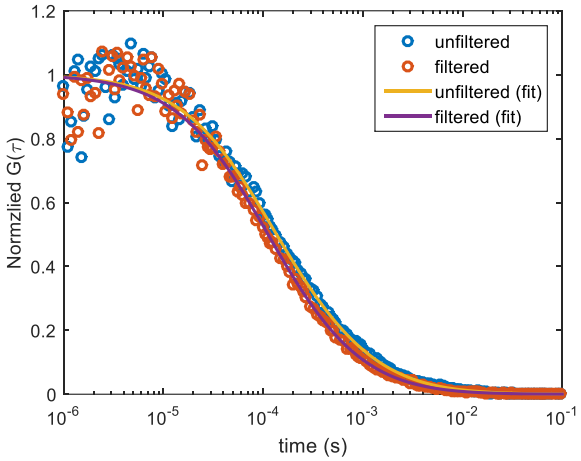

Figure A4.8. Normalized FCS curves for unfiltered and filtered MEHPPV in toluene

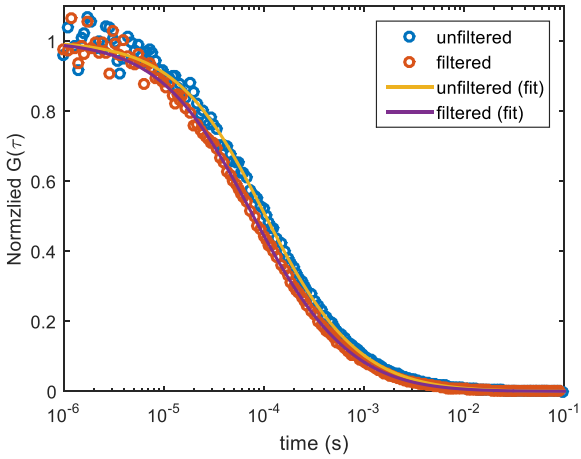

Figure A4.9. Normalized FCS curves for unfiltered and filtered P3HT DP25 in toluene

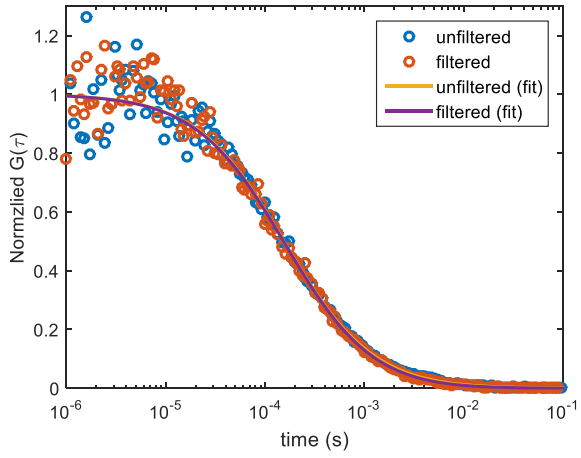

Figure A4.10. Normalized FCS curves for unfiltered and filtered P3HT DP50 in toluene

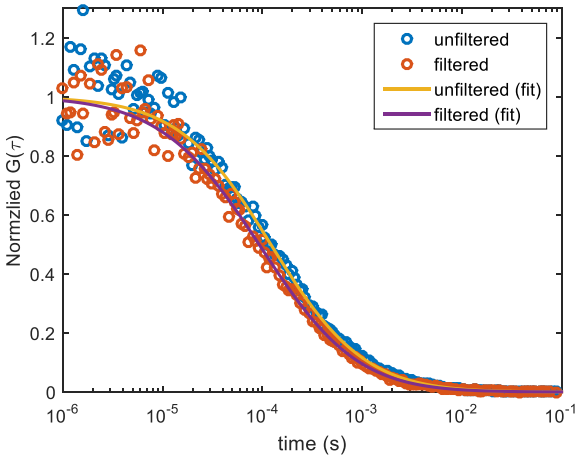

Figure A4.11. Normalized FCS curves for unfiltered and filtered P3HT DP70 in toluene

References

192. Sirringhaus, H.; Tessler, N.; Friend, R. H. Integrated Optoelectronic Devices Based on Conjugated Polymers. *Science*, **1998**, *280*, 1741–1744.
193. Huynh, W. U.; Dittmer, J. J.; Alivisatos, A. P. Hybrid Nanorod-Polymer Solar Cells. *Science*, **2002**, *295*, 2425–2427.
194. Friend, R. H.; Gymer, R. W.; Holmes, A. B.; Burroughes, J. H.; Marks, R. N.; Taliani, C.; Bradley, D. D. C.; Dos Santos, D. A.; Brédas, J. L.; Lögdlund, M.; Salaneck, W. R. Electroluminescence in Conjugated Polymers. *Nature*, **1999**, *397*, 121–128.
195. Nguyen, T.-Q.; Doan, V.; Schwartz, B. J. Conjugated Polymer Aggregates in Solution: Control of Interchain Interactions. *J. Chem. Phys.*, **1999**, *110*, 4068–4078.
196. Nguyen, T.-Q.; Kwong, R. C.; Thompson, M. E.; Schwartz, B. J. Improving the Performance of Conjugated Polymer-Based Devices by Control of Interchain Interactions and Polymer Film Morphology. *Appl. Phys. Lett.*, **2000**, *76*, 2454–2456.
197. Schwartz, B. J. Conjugated Polymers as Molecular Materials: How Chain Conformation and Film Morphology Influence Energy Transfer and Interchain Interactions. *Annu. Rev. Phys. Chem.*, **2003**, *54*, 141–172.
198. Sherwood, G. A.; Cheng, R.; Smith, T. M.; Werner, J. H.; Shreve, A. P.; Peteanu, L. A.; Wildeman, J. Aggregation Effects on the Emission Spectra and Dynamics of Model Oligomers of MEH-PPV. *J. Phys. Chem. C*, **2009**, *113*, 18851–18862.
199. Lin, H.; Hania, R. P.; Bloem, R.; Mirzov, O.; Thomsson, D.; Scheblykin, I. G. Single Chain *versus* Single Aggregate Spectroscopy of Conjugated Polymers. Where is the Border? *Phys. Chem. Chem. Phys.*, **2010**, *12*, 11770–11777.
200. Brazard, J.; Ono, R. J.; Bielawski, C. W.; Barbara, P. F.; Vanden Bout, D. A. Mimicking Conjugated Polymer Thin-Film Photophysics with a Well-Defined Triblock Copolymer in Solution. *J. Phys. Chem. B*, **2013**, *117*, 4170–4176.

201. Wang, D.; Yuan, Y.; Mardiyati, Y.; Bubeck, C.; Koynov, K. From Single Chains to Aggregates, How Conjugated Polymers Behave in Dilute Solutions. *Macromolecules*, **2013**, *46*, 6217–6224.
202. Hong, J.; Jeon, S.K.; Kim, J. J.; Devi, D.; Chacon-Madrid, K.; Lee, W.; Koo, S. M.; Wildeman, J.; Sfeir, M. Y.; Peteanu, L. A. The Effects of Side-Chain-Induced Disorder on the Emission Spectra and Quantum Yields of Oligothiophene Nanoaggregates: A Combined Experimental and MD-TDDFT Study. *J. Phys. Chem. A*, **2014**, *118*, 10464–10473.
203. Hao, X.-T.; McKimmie, L. J.; Smith, T. A. Spatial Fluorescence Inhomogeneities in Light-Emitting Conjugated Polymer Films. *J. Phys. Chem. Lett.*, **2011**, *2*, 1520–1525.
204. Nguyen, T.-Q.; Yee, R. Y.; Schwartz, B. J. Solution Processing of Conjugated Polymers: the Effects of Polymer Solubility on the Morphology and Electronic Properties of Semiconducting Polymer Films. *J. Photochem. and Photobio. A*, **2001**, *144*, 21–30.
205. Fauvell, T. J.; Zheng, T.; Jackson, N. E.; Ratner, M. A.; Yu, L.; Chen, L. X. Photophysical and Morphological Implications of Single-Strand Conjugated Polymer Folding in Solution. *Chem. Mater.*, **2016**, *28*, 2814–2822.
206. Thomas, A. K.; Brown, H. A.; Datko, B. D.; Garcia-Galvez, J. A.; Grey, J. K. Interchain Charge-Transfer States Mediate Triplet Formation in Purified Conjugated Polymer Aggregates. *J. Phys. Chem. C*, **2016**, *120*, 23230–23238.
207. So, W. Y.; Hong, J.; Kim, J. J.; Sherwood, G. A.; Chacon-Madrid, K.; Werner, J. H.; Shreve, A. P.; Peteanu, L. A.; Wildeman, J. Effects of Solvent Properties on Spectroscopy and Dynamics of Alkoxy-Substituted PPV Oligomer Aggregates. *J. Phys. Chem. B*, **2012**, *116*, 10504–10513.
208. Aragón, S.R.; Pecora, R. Fluorescence Correlation Spectroscopy as a Probe of Molecular Dynamics. *J. Chem. Phys.* **1976**, *64*, 1791–1803.
209. Rigler, R.; Mets, Ü.; Widengren, J.; Kask, P. Fluorescence Correlation Spectroscopy with High Count Rate and Low Background: Analysis of Translational Diffusion. *Eur. Biophys. J.* **1993**, *22*, 169–175.
210. Gell, C.; Brockwell, D. J.; Beddard, G. S.; Radford, S. E.; Kalverda, A. P.; Smith, D. A. Accurate Use of Single Molecule Fluorescence Correlation Spectroscopy to Determine Molecular Diffusion Times. *Single Mol.* **2001**, *2*, 177–181.
211. Moerner, W. E.; Fromm, D. P.; Methods of Single-Molecule Fluorescence Spectroscopy and Microscopy. *Rev. Sci. Instrum.* **2003**, *74*, 3597–3619.
212. Enderlein, J.; Gregor, I.; Patra, D.; Fitter, J. Art and Artefacts of Fluorescence Correlation Spectroscopy. *Current Pharmaceutical Biotechnology* **2004**, *5*, 155–161.
213. Enderlein, J.; Gregor, I.; Patra, D.; Dertinger, T.; Kaupp, U. B. Performance of Fluorescence Correlation Spectroscopy for Measuring Diffusion and Concentration. *Chem. Phys. Chem*. **2005**, *6*, 2324–2336.
214. Tcherniak, A.; Reznik, C.; Link, S.; Landes, C. F. Fluorescence Correlation Spectroscopy: Criteria for Analysis in Complex Systems. *Anal. Chem.* **2009**, *81*, 746–754.
215. Elson, E. L. Fluorescence Correlation Spectroscopy: Past, Present, Future. *Biophys. J.* **2011**, *101*, 2855–2870.
216. Huser, T.; Yan, M. Solvent-Related Conformational Changes and Aggregation of Conjugated Polymers Studied by Single Molecule Fluorescence Spectroscopy. *J. Photochem. Photobio. A: Chem.*, **2001**, *144*, 43–51.

217. Bolinger, J. C.; Traub, M. C.; Brazard, J.; Adachi, T.; Barbara, P. F.; Vanden Bout, D. A. Conformation and Energy Transfer in Single Conjugated Polymers. *Acc. Chem. Res.*, **1993**, *45* 1992–2001.
218. Günes, S.; Neugebauer, H.; Sariciftci, N. S. Conjugated Polymer-Based Organic Solar Cells. *Chem. Rev.*, **2007**, *107*, 1324–1338.
219. Shen, W.; Xiao, M.; Tang, J.; Wang, X.; Chen, W.; Yang, R.; Bao, X.; Wang, Y.; Jiao, J.; Huang, L.; Liu, J.; Wang, W.; Belfiore, L. A. Effective Regulation of the Micro-Structure of Thick P3HT:PC71BM Film by the Incorporation of Ethyl Benzenecarboxylate in Toluene Solution. *RSC Adv.*, **2015**, *5*, 47451–47457.
220. Oelkrug, D.; Egelhaaf, H.-J.; Gierschner, J.; Tompert, A. Electronic Deactivation in Single Chains, Nano-Aggregates and Ultrathin Films of Conjugated Oligomers. *Synth. Met.*, **1996**, 76, 249–253.
221. Oelkrug, D.; Tompert, A.; Gierschner, J.; Egelhaaf, H.-J.; Hanack, M.; Hohloch, M.; Steinhuber, E. Tuning of Fluorescence in Films and Nanoparticles of Oligophenylenevinylenes. *J. Phys. Chem. B*, **1998**, *102*, 1902–1907.
222. van Hutten, P. F.; Krasnikov, V. V.; Hadziioannou, G. A Model Oligomer Approach to Light-Emitting Semiconducting Polymers. *Acc. Chem. Res.*, **1999**, *32*, 257–265.
223. Bredas, J.-L.; Cornil, J.; Beljonne, D.; dos Santos, D. A.; Shuai, Z. Excited-State Electronic Structure of Oligomers and Polymers: A Quantum-Chemical Approach to Optical Phenomena, *Acc. Chem. Res.*, **1999**, *32*, 267–276.
224. Brédas, J. L.; Beljonne, D.; Cornil, J.; Calbert, J. P.; Shuaí, Z.; Silbey, R. Electronic Structure of π-Conjugated Oligomers and Polymers: A Quantum-Chemical Approach to Transport Properties. *Synth. Met.*, **2001**, *125*, 107–116.
225. Collison, C. J.; Treemaneekam, V.; Oldham Jr., W. J.; Hsu, J. H.; Rothberg, L. J. Aggregation Effects on the Structure and Optical Properties of a Model PPV Oligomer. *Synth. Met.*, **2001**, *119*, 515–518.
226. Peeters, E.; Ramos, A. M.; Meskers, S. C. J.; Janssen, R. A. J. Singlet and Triplet Excitations of Chiral Dialkoxy-p-Phenylene Vinylene Oligomers. *J. Chem. Phys.*, **2000**, *112*, 9445–9454.
227. Schenning, A. P. H. J.; Jonkheijm, P.; Peeters, E.; Meijer, E. W. Hierarchical Order in Supramolecular Assemblies of Hydrogen-Bonded Oligo(p-phenylene vinylene)s. *J. Am. Chem. Soc.* **2001**, *123*, 409–416.
228. Lim, S.-H.; Bjorklund, T. G.; Bardeen, C. J. Characterization of Individual Submicron Distyrylbenzene Aggregates Using Temperature-Depencdent Picosecond Fluorescence and Atomic Force Microscopy. *J. Phys. Chem. B*, **2004**, *108*, 4289–4295.
229. Bussian, D. A.; Summers, M. A.; Liu, B.; Bazan, G. C.; Burratto, S. K. Photon Pair Correlation Spectroscopy of Single Tetrahedral Oligophenylenevinylene Molecules at Room Temperature. *Chem. Phys. Lett.*, **2004**, *388*, 181–185.
230. Gierschner, J.; Oelkrug, D. *Optical Properties of OligophenyleneVinylenes*. American Scientific Publishers, Stevenson Ranch, CA, 2004.
231. Gierschner, J.; Ehni, M.; Egelhaaf, H. J.; Medina, B. M.; Beljonne, D.; Benmansour, H.; Bazan, G. C. Solid-State Optical Properties of Linear Polyconjugated Molecules: π-Stack Contra Herringbone. *J. Chem. Phys.*, **2005**, *123*, 144914.

232. Summers, M. A.; Kemper, P. R.; Bushnell, J. E.; Robinson, M. R.; Bazan, G. C.; Bowers, M. T.; Buratto, S. K. Conformation and Luminescence of Isolated Molecular Semiconductor Molecules. *J. Am. Chem. Soc.*, **2003**, *125*, 5199–5203.
233. Steiner, F.; Vogelsang, J.; Lupton, J. M. Singlet-Triplet Annihilation Limits Exciton Yield in Poly(3-Hexylthiophene). *Phys. Rev. Lett.*, **2014**, *112*, 137402.
234. Cook, S.; Furube, A.; Katoh, R. Analysis of the Excited States of Regioregular Polythiophene P3HT. *Energ. Environ. Sci.*, **2008**, *1*, 294–299.
235. Piris, J.; Dykstra, T. E.; Bakulin, A. A.; van Loosdrecht, P. H. M.; Knulst, W.; Trinh, M. T.; Schins, J. M.; Siebbeles, L. D. A. Photogeneration and Ultrafast Dynamics of Excitons and Charges in P3HT/PCBM Blends. *J. Phys. Chem. C*, **2009**, *113*, 14500–14506.
236. Sheng, C. X.; Tong, M.; Singh, S.; Vardeny, Z. V. Experimental Determination of the Charge/Neutral Branching Ratio η in the Photoexcitation of π-Conjugated Polymers by Broadband Ultrafast Spectroscopy. *Phys. Rev. B*, **2007**, *75*, 085206.
237. Lin, H.; Tian, Y.; Zapadka, K.; Persson, G.; Thomsson, D.; Mirzov, O.; Larsson, P.-O.; Widengren, J.; Scheblykin, I. G. Fate of Excitations in Conjugated Polymers: Single-Molecule Spectroscopy Reveals Nonemissive "Dark" Regions in MEH-PPV Individual Chains. *Nano Lett.*, **2009**, *9*, 4456–4461.
238. Paquin, F.; Latini, G.; Sakowicz, M.; Karsenti, P.-L.; Wang, L.; Beljonne, D.; Stingelin, N.; Silva, C. Charge Separation in Semicrystalline Polymeric Semiconductors by Photoexcitation: Is the Mechanism Intrinsic or Extrinsic? *Phys. Rev. Lett.*, **2011**, *106*, 197401.
239. Davydov, A. S. *Theory of Molecular Excitons*; McGraw-Hill: New York, 1962.
240. Kasha, M.; Rawls, H. R.; El-Bayoumi, M. A. The Exciton Model in Molecular Spectroscopy. *Pure Appl. Chem.*, **1965**, *11*, 371–392.
241. Spano, F. C. The Spectral Signatures of Frenkel Polarons in H- and J-Aggregates. *Acc. Chem. Res.*, 2010, *43*, 429–439.
242. Kroeze, J. E.; Savenije, T. J.; Vermeulen, M. J. W.; Warman, J. M. Contactless Determination of the Photoconductivity Action Spectrum, Exciton Diffusion Length, and Charge Separation Efficiency in Polythiophene-Sensitized TiO2 Bilayers. *J. Phys. Chem. B*, **2003**, *107*, 7696–7705.
243. Lüer, L.; Egelhaaf, H.-J.; Oelkrug, D.; Cerullo, G.; Lanzani, G.; Huisman, B.-H.; de Leeuw, D. Oxygen-Induced Quenching of Photoexcited States in Polythiophene Films. *Org. Electron.*, **2004**, *5*, 83–89.
244. Lewis, A. J.; Ruseckas, A.; Gaudin, O. P. M.; Webster, G. R.; Burn, P. L.; Samuel, I. D. W. Singlet Exciton Diffusion in MEH-PPV Films Studied by Exciton-Exciton Annihilation. *Organic Electron.*, **2006**, *7*, 452–456.
245. Goh, C.; Scully, S. R.; McGehee, M. D. Effects of Molecular Interface Modification in Hybrid Organic-Inorganic Photovoltaic Cells. *J. Appl. Phys.*, **2007**, *101*, 114503.
246. Shaw, P. E.; Ruseckas, A.; Samuel, I. D. W. Exciton Diffusion Measurements in Poly(3-hexylthiophene). *Adv. Mater.* **2008**, *20*, 3516–3520.
247. Vogelsang, J.; Adachi, T.; Brazard, J.; Vanden Bout, D. A.; Barbara, P. F. Self-Assembly of Highly Ordered Conjugated Polymer Aggregates with Long-Range Energy Transfer. *Nature Materials*, **2011**, *10*, 942–946.

248. Samuel, I. D. W.; Rumbles, G.; Collison, C. J. Efficient Interchain Photoluminescence in a High-Electron Affinity Conjugated Polymer. *Phys. Rev. B* **1995**, *52*, R11573–R11576.
249. Cornil, J.; dos Santos, D. A.; Crispin, X.; Brédas, J. L. Influence of Interchain Interactions on the Absorption and Luminescence of Conjugated Oligomers and Polymers: A Quantum-Chemical Characterization. *J. Am. Chem. Soc.*, **1998**, *120*, 1289–1299.
250. Tretiak, S.; Saxena, A.; Martin, R. L.; Bishop, A. R. Interchain Electronic Excitations in Poly(phenylenevinylene) (PPV) Aggregates. *J. Phys. Chem. B*, **2000**, *104*, 7029–7037.
251. Hu, D.; Yu, J.; Wong, K.; Bagchi, B.; Rossky, P. J.; Barbara, P. F. Collapse of Stiff Conjugated Polymers with Chemical Defects into Ordered, Cylindrical Conformations. *Nature*, **2000**, *405*, 1030–1033.
252. Siddiqui, S.; Spano, F. C. H- and J- Aggregates of Conjugated Polymers and Oligomers: A Theoretical Investigation. *Chem. Phys. Lett.*, **1999**, *308*, 99–105.
253. Beljonne, D.; Cornil, J.; Silbey, R.; Millié, P.; Brédas, J. L. Interchain Interactions in Conjugated Materials: The Exciton Model versus the Supermolecular Approach. *J. Chem. Phys.* **2000**, *112*, 4749−4758.
254. Spano, F. C. Excitons in Conjugated Oligomer Aggregates, Films, and Crystals. *Annu. Rev. Phys. Chem.*, **2006**, *57*, 217−243.
255. Clark. J.; Chang, J.-F.; Spano, F. C.; Friend, R. H.; Silva, C. Determining Exciton Bandwidth and Film Microstructure in Polythiophene Films Using Linear Absorption Spectroscopy. *Appl. Phys. Lett.*, **2009**, *94*, 163306.
256. Löwe, C.; Weder, C. Oligo(p-phenylene Vinylene) Excimers as Molecular Probes: Deformation-Induced Color Changes in Photoluminescent Polymer Blends. *Adv. Mater.*, **2002**, *14*, 1625–1629.
257. Jagtap, S. P.; Mukhopadhyay, S.; Coropceanu, V.; Brizius, G. L.; Brédas, J.-L.; Collard, D. M. Closely Stacked Oligo(phenylene ethynylene)s: Effect of π-Stacking on the Electronic Properties of Conjugated Chromophores. *J. Am. Chem. Soc.*, **2012**, *134*, 7176–7185.
258. Brown, K. E.; Salamant, W. A.; Shoer, L. E.; Young, R. M.; Wasielewski, M. R. Direct Observation of Ultrafast Excimer Formation in Covalent Perylenediimide Dimers Using Near-Infrared Transient Absorption Spectroscopy. *J. Phys. Chem. Lett.*, **2014**, *5*, 2588–2593.
259. Lindquist, R. J.; Lefler, K. M.; Brown, K. E.; Dyar, S. M.; Margulies, E. A.; Young, R. M.; Wasielewski, M. R. Energy Flow Dynamics within Cofacial and Slip-Stacked Perylene-3,4-dicarboximide Dimer Modesl of π-Aggregates. *J. Am. Chem. Soc.*, **2014**, *136*, 14912–14923.
260. Wachsmuth, M.; Waldeck, W.; Langowski, J. Anomalous Diffusion of Fluorescent Probes Inside Living Cell Nuclei Investigated by Spatially-Resolved Fluorescence Correlation Spectroscopy. *J. Mol. Biol.*, **2000**, *298*, 677–689.
261. Sillen, A.; Engelborghs, Y. The Correct Use of "Average" Fluorescence Parameters. *Photochemistry and Photobiology*, **1998**, *67*, 475–486.

Chapter 5. Fluorescent Studies of Model Oligomers of MEH-PPV in Ionic Liquids

5.1. Introduction

Although ILs have been used in a variety of electorchemical devices, [262–267] the combination of IL and conjugated polymers in electrochemical devices had not been sufficiently explored. Osteryoung *et al.* were one of the first to report the use of ILs in preparation of conjugated polymer films, and to show that the polymers show reversible and stable electrochemical behaviors. [268, 269] Mattes *et al.* prepared electrochemical mechanical actuators, eletrochromic windows, and numeric displays from conjugated polymers and ILs. These devices showed enhanced lifetime and fast cycle switching speed, Furthermore, their experiments were carried out under ambient conditions, and not under inert nitrogen atmosphere.[270] A better understanding of the polymer morphology and the interactions between polymer and ILs will improve and design and the performances of these devices.

More specifically, ILs are known to form nonpolar and polar domains. [271–274] Experiments and simulations have shown that these regions range from 11 Å to 20Å.[275–280] Past studies of conjugated polymers have also shown that solvent choice affects the properties of films made from these materials.[281,282] Our interest here is in to understand how these domains and ions affect conjugated polymers.

In this study, we examined the fluorescence behavior of PPV oligomers in ILs, and used these results to infer the morphology of the oligomers. Oligomers serve as useful model systems for the larger polymers.[283–294] Oligomers and polymers should have similar

interchain interactions, but oligomers have the added benefit of not having multiple chain lengths or structural defects.[295]

5.2. Experimental Methods

The structures for the model oligomer and ILs are shown in Schemes 5.1 and 5.2. Four different lengths were studied: OPPV5 (n=2), OPPV7 (n=3), OPPV9 (n=4), and OPPV13 (n=6). Three different ionic liquids (Iolitec) were used for this study, and they are 1-butyl-1-methylpyrrolidinium bis(trifluoromethylsulfonyl)imide [$Pyrr_{1,4}$][Tf_2N], 1-butyl-3-methylimidazolium bis(trifluoro-methylsulfonyl)imide [Bmim][Tf_2N], and 1-butyl-3-ethylimidazolium bis(trifluoromethylsulfonyl) imide [Emim][Tf_2N]. All three ILs have the same anion. [Bmim] and [$Pyrr_{1,4}$] have the same alkyl chain length, but [Bmim] is aromatic, while [$Pyrr_{1,4}$] is not. [Bmim] and [Emim] are both aromatic, but have different alkyl chain length. Oligomers were first dissolved in THF, then diluted to the desired concentration with THF or IL. For the ILs, the solutions were heated in a vacuum oven to remove THF.

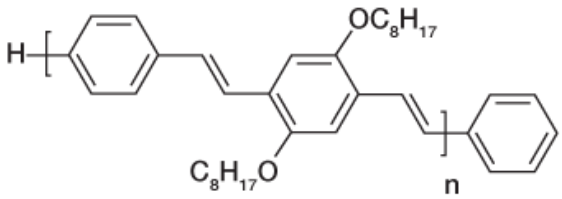

Scheme 5.1. Repeating unit of model oligomers

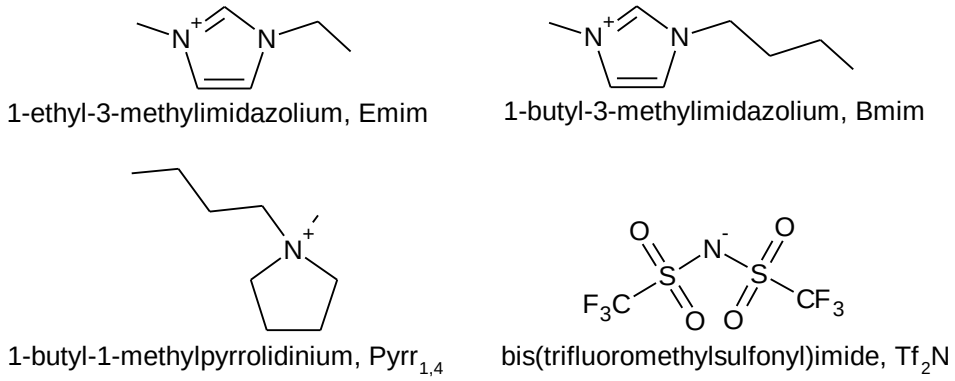

Scheme 5.2. Structure of IL cations and anion

The emission spectra and fluorescence anisotropy measurements of the oligomers were collected with fluorimeter. (Jobin-Yvon FluoroMax 2) The fluorescence lifetimes and fluorescence correlation spectra were collected using a confocal microscope. For the confocal microscope, 440 nm pulsed diode lasers (Picoquant) was the excitation source. A 1.4 NA 100x oil objective (Olympus UPlanSAPO 100x 1.4 Oil) was mounted on an inverted microscope (Olympus IX-71). The pinhole placed after the microscope was 100-μm in diameter. A 50-50 beam splitter (Semrock) was placed after the pinhole to split the emission onto two single photon avalanche diodes (Micro Photon Devices PDM50). A longpass filter (475-nm for OPPV7 or 515-nm for everything else) was placed in front of the beam splitter to remove scattering. Time-tagging of the photons was done by PicoHarp 300 and PHR 800 (Picoquant). All the data were collected and analyzed using SymPhoTime (Picoquant).

Fluorescence correlation spectroscopy (FCS) measures the diffusion of the fluorescent probes by monitoring the fluctuations of the photon intensities $I(t)$ in the focal volume. The FCS curve, $G(\tau)$, is calculated by cross-correlating the photon intensities of

the two detectors. If the focal volume is assumed to have a three-dimensional Gaussian shape, the correlation curves can be fitted with

$$G(t) = \left(\frac{1}{N}\right)\left(1 + \frac{t}{\tau_D}\right)^{-1}\left[1 + \kappa^2\left(\frac{t}{\tau_D}\right)\right]^{-\frac{1}{2}} \quad \text{(Eq. 5.1)}$$

where κ describes the shape of the focal volume, and τ_D is the characteristic residence time. The diffusion constant of the fluorophore can be calculated using Eq. 5.2

$$D = \frac{\omega_{xy}^2}{4\tau_D} \quad \text{(Eq. 5.2)}$$

where ω_{xy} is the radial radius of the focal volume.

To compare the FCS curve between different solvents, the correlation curve can be adjusted to account for the difference in viscosity. The Stokes-Einstein relation predicts that the diffusion constant is inversely proportion to the product of the medium viscosity and the hydration radius of the diffusing particle. Therefore, the ratio of diffusion constants in two different solvents is proportional to

$$\frac{D_1}{D_2} = \frac{R_2\eta_2}{R_1\eta_1} \quad \text{(Eq. 5.3)}$$

By combing Eq. 5.2 and Eq. 5.3, the ratio of the characteristic residence times becomes

$$\tau_{D,1} = \left(\frac{R_2\eta_2}{R_1\eta_1}\right)\tau_{D,2} \quad \text{(Eq. 5.4)}$$

Finally, substitution Eq. 5.4 into Eq. 5.1 and assuming that the shape of the focal volume, κ, stays constant, the correlation curves should obey the following relation:

$$G_1(t) = G_2\left[\left(\frac{R_1\eta_1}{R_2\eta_2}\right)t\right] \quad \text{(Eq. 5.5)}$$

Graphically, if the FCS curves are plotted on a lin-log plot (a plot with linear scale on the y-axis and logarithm scale on the x-axis), a change in hydration radius or viscosity shifts the curve horizontally.

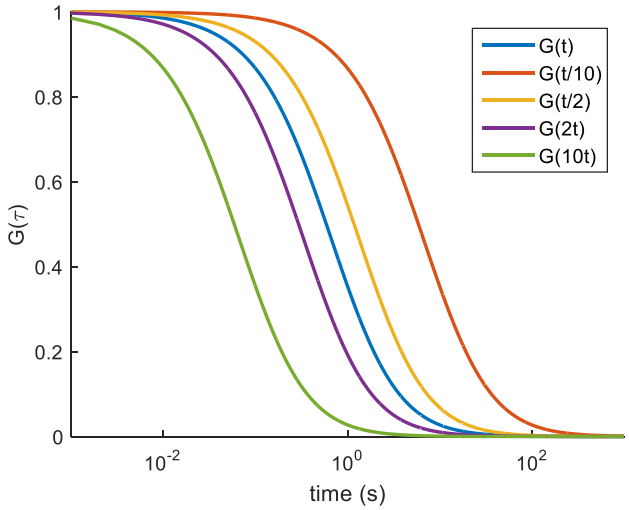

Figure 5.1. FCS curves with different with different ratio of $R_1\eta_1/R_2\eta_2$

5.3. Results

5.3.1 Emission spectra, Fluorescence Lifetime, and Fluorescence Anisotropy

The emission spectra of the oligomers in THF and ILs are shown in Figures 5.2 and 5.3. In Figure 5.2, the emission spectra are normalized by the λ_{max} of each to facilitate comparison. In Figure 3, the emission spectra are normalized by the λ_{max} of the oligomers in THF to show the amount of fluorescence quenching in each oligomer. For example, the maximum intensity for OPPV5 in $[Pyrr_{1,4}][Tf_2N]$ is 0.35, which meant its intensity was 35% of OPPV5 in THF. For ease of comparison, the wavelengths and the normalized intensities for the 0-0 transition are tabulated in Table 5.1.

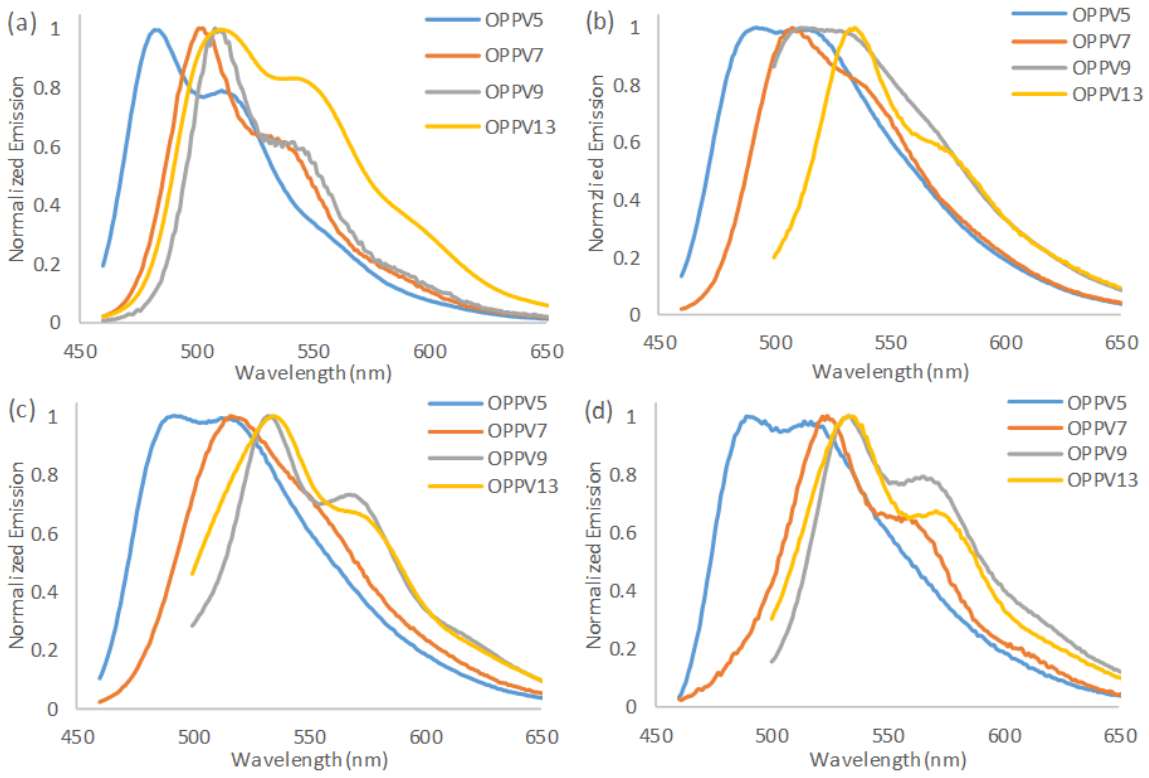

Figure 5.2. Emission spectra of OPPV5, OPPV7, OPPV9 and OPPV13 in (a) THF, (b) $[Pyrr_{1,4}][Tf_2N]$, (c) $[Bmim][Tf_2N]$, and (d) $[Emim][Tf_2N]$. The emission spectra are normalized with respect to themselves.

When dissolved in IL, the emission spectra of all the oligeomers redshifted by 10 to 20 nm, and for the most part retained the vibronic structure observed in THF. When PPV oligomers aggregate in THF-methanol mixtures, the ratio of the 0-0 band to the 0-1 band changes. For small aggregates, the 0-1 band is taller than the 0-0 band, and as the size of the aggregate increases, the height of the 0-0 band increases. Based on the spectral changes observed when oligomers aggregate in methanol, these emission spectra suggest that either the conjugated oligomers are not aggregating or they are forming large aggregates (>1000nm) in ILs. The redshifts in the emission spectra could be caused by a variety of factors. For example, ILs are more polar than THF, therefore the redshift observed could

be a solvatochromic shift where the excited state was stabilized by the polar environment. Another possibility is that the ILs, especially the aromatic ILs, cause the oligomers to become more planar, due to the π-π solvent-solute interactions. As a result of the planarization, conjugation length increased, and emission redshifted.

Table 5.1. Wavelength and normalized intensity for the 0-0 transition.

	Wavelength [a]				Normalized Intensity			
	OPPV5	OPPV7	OPPV9	OPPV13	OPPV5	OPPV7	OPPV9	OPPV13
THF	483	502	507	512	1.00	1.00	1.00	1.00
$Pyrr_{1,4}$	491	512	512	531	0.34	0.28	0.14	0.02
Bmim	495	523	529	531	0.73	0.10	0.06	0.01
Emim	489	525	531	533	0.28	0.02	0.02	0.01

[a] in nm

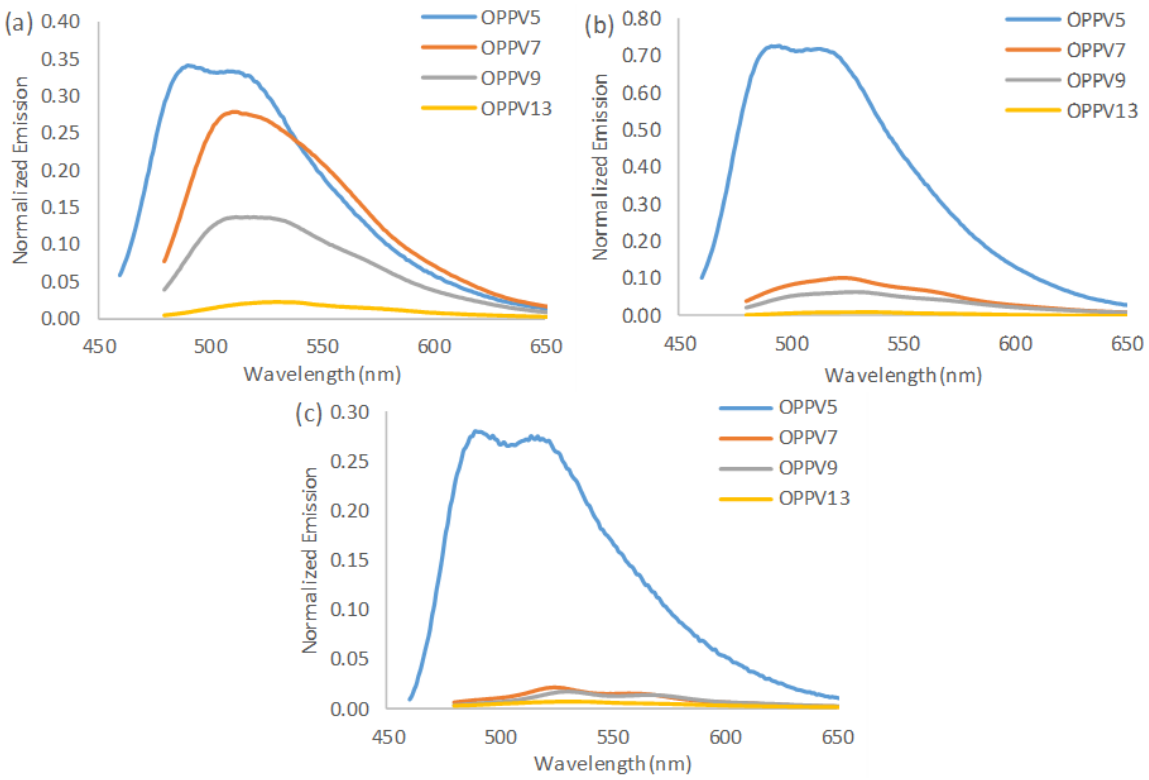

Figure 5.3. Emission spectra of OPPV5, OPPV7, OPPV9, and OPPV13 in (a) $[Pyrr_{1,4}][Tf_2N]$, (b) $[Bmim][Tf_2N]$, and (c) $[Emim][Tf_2N]$. The emission spectra are normalized with respect to the emission spectra of the oligomers in THF to show the relative degree of quenching.

All of the oligomers exhibited emission quenching when dissolved in ILs. The trend observed was that longer chains were quenched more efficiently than the shorter chains. Field-induced quenching measurements showed that, at the same applied field, longer chains are quenched more than shorter chains due to the stabilization of the free electron-hole pair state.[297] Due to the ionic nature of ILs, ILs could also stabilize the free electron-hole pair state, and cause the longer oligomers to quench more than the shorter oligomers.

To gain greater insight into their phenomenon, the fluorescence lifetimes of the oligomers were measured (Table 5.2 and Figure 5.4).

Table 5.2. Fluorescence lifetime of the model oligomers in THF and IL [a]

	THF	$Pyrr_{1,4}$	Bmim	Emim
OPPV5	0.87 (97%) 4.3 (3%)	1.9 (70%) 6.3 (30%)	1.3 (96%) 3.7 (4%)	1.4 (94%) 4.5 (6%)
OPPV7	0.74 (90%) 2.0 (10%)	1.6 (68%) 6.0 (32%)	0.88 (77%) 2.0 (23%)	0.32 (86%) 2.1 (14%)
OPPV9	0.78 (94%) 4.0 (6%)	1.2 (75%) 5.6 (25%)	0.74 (88%) 1.7 (12%)	0.35 (91%) 2.1 (9%)
OPPV13	0.65 (98%) 5.0 (2%)	1.0 (78%) 6.0 (22%)	0.68 (92%) 3.9 (8%)	0.61 (82%) 4.5 (18%)

[a] Fluorescence lifetimes are reported in ns. The number in the parenthesis is the relative amplitude of each component.

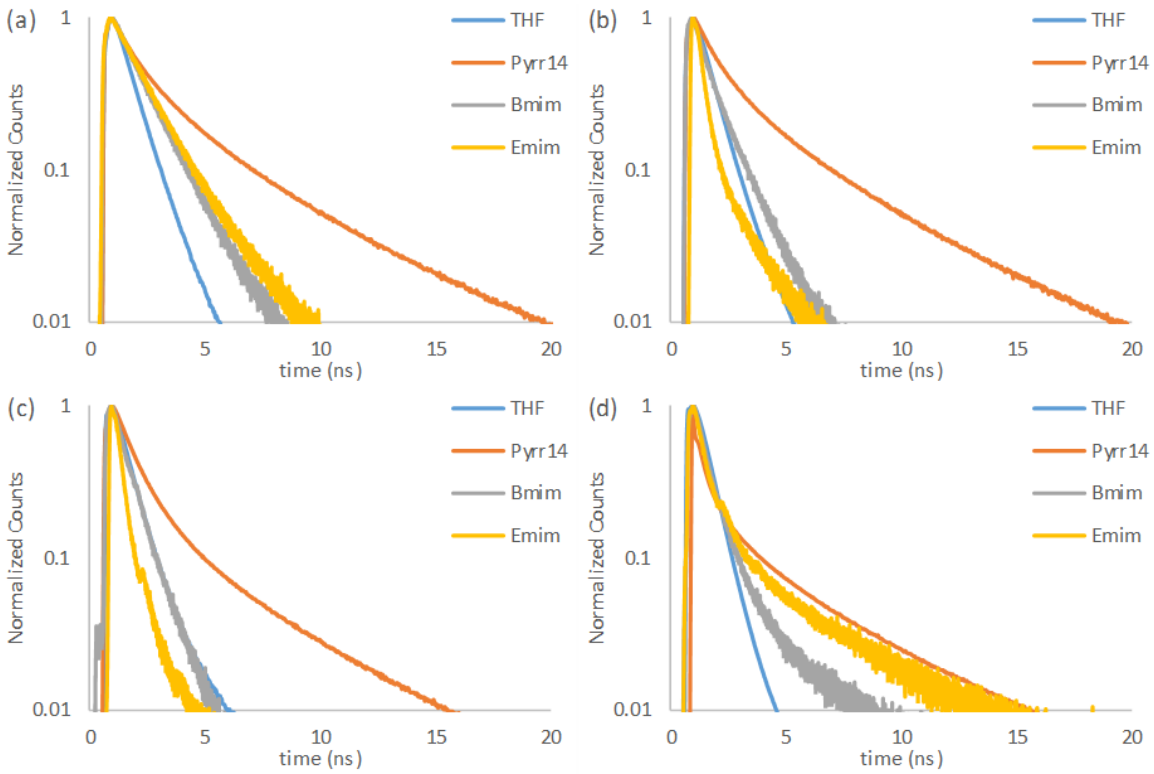

Figure 5.4. Fluorescence lifetime of (a) OPPV5, (b) OPPV 7, (c) OPPV9, and (d) OPPV13 in THF, [Pyrr$_{1,4}$][Tf$_2$N], [Bmim][Tf$_2$N], and [Emim][Tf$_2$N]

In general, oligomers exhibited a longer fluorescence lifetime in IL than in THF. The exceptions are OPPV7 and OPPV9 in [Emim][Tf$_2$N], for which the fluorescence lifetimes were shorter in the IL than in THF. A longer fluorescence lifetime could be due to the formation of excimers. Due to the forbidden transition to the ground state, excimers typically have longer fluorescence lifetime. For example, in some cyano-PPV films, the fluorescence lifetime is ~5 ns due to the formation of excimers.[285,293,294,298,299]

The fluorescence anisotropy (Table 5.3) was calculated by

$$r = \frac{GI_{VV} - I_{VH}}{GI_{VV} - 2I_{VH}} \qquad \text{(Eq. 5.6)}$$

where I_{XY} denotes the fluorescence intensity with X-orientation for excitation and Y-orientation for detection, and $G(= I_{HH}/I_{HV})$ is a correction factor that corrects for the detection efficiencies of the horizontal (H) and vertical (V) orientation.

Table 5.3. Fluorescence anisotropy of oligomers in THF, $Pyrr_{1,4}$, Bmim, and Emim.

	THF	$Pyrr_{1,4}$	Bmim	Emim
OPPV5	0.06	0.40	0.31	0.32
OPPV7	0.16	0.31	0.17	0.25
OPPV9	0.14	0.20	0.11	0.15
OPPV13	0.24	0.18	0.18	0.21

As expected, the fluorescence anisotropy increases as the chain length increases in THF. Reorientational motions is slower for longer oligomers and, as a result, the fluorescence anisotropy increases. However, the opposite trend was observed in ILs. As the length of the chain increased, the fluorescence anisotropy generally decreased. The decrease in fluorescence anisotropy could indicate that as oligomers becomes more compact and smaller as the chain length increases or that intrachain-hopping of the exciton is more efficient for the longer chain. Efficient intrachain hopping would cause the oligomers to emit from a different segment of the chain than the segment that was excited. As a result, the fluorescence anisotropy would decrease.

Before presenting the results from confocal microscopy, we will summarize the trends observed from bulk fluorescent measurements. In ILs, the emission of all the oligomers was red-shifted and quenched, and the fluorescence lifetimes were generally

longer. As the length of the chain increased, the emission of each molecule was increasingly quenched, and the fluorescence anisotropy decreased.

5.3.2 Confocal Microscopy

Next, we examined the oligomers using confocal microscopy, a single-molecule spectroscopic technique. Due to the background fluorescence from imidazolium based ILs, only results for pyrrolidinium ILs are presented. The absorption spectra of imidazolium ILs stretches from UV to 500 nm, therefore, the emission from the imidazolium ILs overwhelms the emission from polymer at nanomolar concentration.

The brightness per emitter is reported in Table 5.4. the brightness of the molecule can be calculated by multiplying the average intensity with $G(0)$.

$$B \text{ (Brightness per molecule)} = \langle I \rangle G(0) = \frac{\langle I \rangle}{\langle N \rangle} \qquad \text{(Eq. 5.7)}$$

At $\tau = 0$, Eq. 5.1 becomes $G(0) = 1/N$. Therefore, multiplying the average intensity by $G(0)$ is same as dividing the average intensity by the average number of emitters in the focal volume. The counts per emitter for Rhodamine 6G in THF versus in the IL is also reported as a control.

Table 5.4. The ratio of brightness (cps) per emitter for rhodamine 6G (R6G) and oligomers in THF versus IL.

	R6G	OPPV5	OPPV7	OPPV9	OPPV13
B_{IL}/B_{THF}	1.12	0.43	0.31	0.40	0.08

As expected, the intensity ratio was close to 1 for rhodamine 6G, which is not expected to have different intensities in THF *versus* in an IL. Similar to the trends observed in bulk emission spectra, as the length of the polymer increases, greater quenching was observed. Furthermore, with the exception of OPPV9, the amounts of quenching were similar between the bulk emission spectra and confocal measurement. From the bulk emission spectra, the intensity ratios of IL *versus* THF were 0.34, 0.28, and 0.02 for OPPV5, OPPV7, and OPPV13, respectively, while the intensity ratios from confocal were 0.43, 0.31, and 0.08 for OPPV5, OPPV7, and OPPV13, respectively. The agreement between confocal measurements and bulk emission spectra indicate that the oligomers behave similarly at high and low concentration. This is important, because it showed that there was no concentration-dependent aggregation. For some solvents, oligomers aggregate at higher concentration due to unfavorable solvent-oligomer interactions.

5.3.3 Fluorescence Correlation Spectroscopy (FCS)

The normalized FCS curves for oligomers in THF and IL are shown in Figure 5.5.

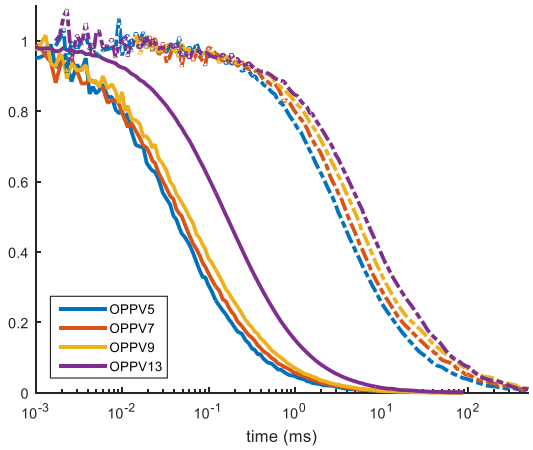

Figure 5.5. The normalized FCS curves for model oligomers in THF versus in the IL.

The shapes of the FCS curves in the IL are similar to that in THF. The IL FCS curves looked like the THF FCS curves but shifted horizontally. The similarity in shapes suggests that either the oligomers are not aggregating, or the aggregates formed have a very narrow size distribution. An example of how aggregates of varying sizes change the shape of the FCS curve is shown below in Figure 5.6. OPPV13 forms aggregates of varying sizes in a mixture of acetonitrile and THF. When there were aggregates of varying sizes, the FCS curves exhibit a multi-component decays. Another indication was the relative decay rate. Even though acetonitrile and THF have similar viscosity, the FCS curve for acetonitrile/THF mixture decays much more slowly than the FCS curve for THF.

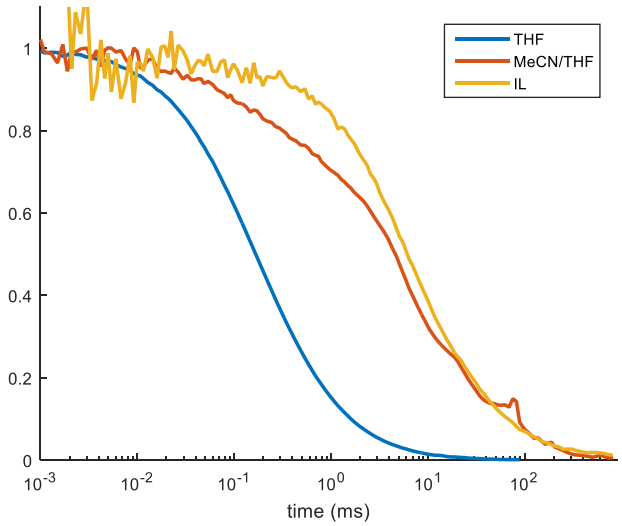

Figure 5.6. FCS curves of OPPV 13 in THF, MeCN/THF mixture, and IL.

As discussed in the experimental methods section, if the dimension of the focal volumes and hydration radius stay constant, an increase in viscosity should shift the FCS curves horizontally, and the FCS curves can be compared using

$$G_{THF}(\tau) = G_{IL}\left[\left(\frac{R_{THF}\eta_{THF}}{R_{IL}\eta_{IL}}\right)t\right] \quad \text{(Eq. 5.8)}$$

where η_{THF} and η_{IL} are the viscosities of THF and IL, respectively, and R_{THF} and R_{IL} are the hydration radius of the oligomers in THF and IL, respectively. Table 5.5 shows the ratio that gives the best fit of the FCS curves.

Past studies showed that due to the ionic nature of ILs, the Stokes-Einstein relation may not hold.[300] Therefore, Rhodamine 6G and Nile Red, which should have the same hydration of radius in THF and IL, were included as control. At 25°C, the reported viscosity of THF and [$Pyrr_{1,4}$][Tf_2N] are 0.48 and 85 mPa s, respectively,[301] which gives a viscosities ratio, η_{IL}/η_{THF}, of 180. Using the reported viscosity ratio, the hydration radius ratios are 1.07 and 0.85 for R6G and NR, respectively. As expected from Stokes-Einstein relation, since the hydration radius of R6G and NR should not differ significantly between THF and IL, the ratios are close to 1. Overall, the ratios for R6G and NR showed that the Stokes-Einstein relation holds fairly well when comparing THF and the IL. Therefore, we could use the ratio to determine the size of the oligomers in IL *versus* in THF.

Table 5.5. The ratio of the product of hydration radius and viscosity that gives the best fit.

	R6G	Nile Red	OPPV5	OPPV7	OPPV9	OPPV13
$\frac{R_{IL}\eta_{IL}}{R_{THF}\eta_{THF}}$	190	150	79	84	77	36
$\frac{R_{IL}}{R_{THF}}$ [a]	1.07	0.85	0.45	0.47	0.44	0.20

[a] Assuming $\eta_{THF}/\eta_{IL} = 180$

For the oligomers, the ratios of the hydration radii are all less than 1. This suggests that the oligomers are unlikely to form large aggregates that are more than 10x or 20x the size of a single chain. This also suggests that the oligomers undergo a morphology change and became more compact in the IL. The decrease in hydration radius could be caused by either the collapse of the octoxy- substituent or the collapse of the phenylene vinylene backbone.

To estimate the effect of folding the alkoxy substituents on the hydration radius, the radii of gyration for two conformations of OPPV5 were calculated. The radius of gyration is numerically similar to the hydration radius. Therefore, it can be used as an estimate of hydration radius.[302] The radius of gyration was calculated as follow

$$R_g^2 = \frac{1}{N}\sum_i (r_i - r_{\text{mean}})^2 \qquad \text{(Eq. 5.9)}$$

where r_i is the position of the *i*th atom and r_{mean} is the average position of all atoms. Figure 5.7 shows the two conformations used in the calculation. In Fig. 5.7a, the octoxy-substituent was fully extended and the alkyl chains were in the *anti* conformation. In Fig. 5.7b, the octoxy- substituent was collaped, and the alkyl chains were in the *gauche* conformation. The radii of gyration were 10.0Å and 9.0Å for the extended and collapsed conformations, respectively. This suggested that the collapse of the alkyl chains only reduced the radius of gyration by 10%, which is less than the 50% reduction observed in FCS measurements. Furthermore, although the effect of collapsing the sidechains becomes less significant as the length of the backbone increases, the reduction in hydration radius increases as the length of the oligomer increases. Therefore, the decrease in hydration radius is likely caused by the collapse of the oligomer backbone, and not of the alkoxy substituent.

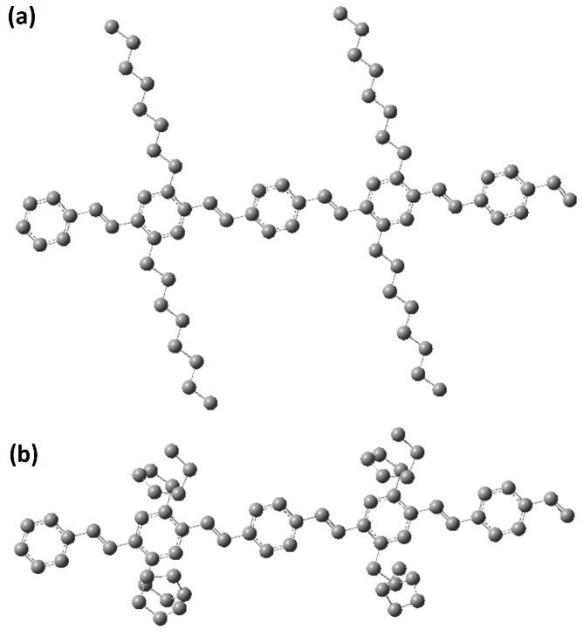

Figure 5.7. The (a) extended and (b) collapsed conformation of OPPV5

5.4. Discussion

We will summarize the findings from bulk and single-molecule spectroscopy measurements, and speculate on the morphology of the oligomers in ILs. Due to background fluorescence, single-molecule spectroscopy measurements with [Bmim][Tf_2N] and [Emim][Tf_2N] were not available, therefore, this discussion will be based on the results of [$Pyrr_{1,4}$][Tf_2N]. However, as the trends observed with fluorescence were similar between the three ILs, the conclusions drawn from [$Pyrr_{1,4}$][Tf_2N] are likely also applicable to [Bmim][Tf_2N] and [Emim][Tf_2N].

First, average intensity measurements obtained from bulk emission spectra and confocal microscopy showed that the amount of quenching in [$Pyrr_{1,4}$][Tf_2N] is similar at both high and low concentration. Therefore, we can safely assume that the chain conformations of the oligomers at high concentration are same at low concentration.

Next, control experiments with R6G and NR showed that the Stokes-Einstein relation holds when comparing the FCS curves of THF and the ILs. With that, the FCS measurements show that the hydration radii of the oligomers are smaller in ILs than in THF. Moreover, as the length of the chain increases, the reduction in hydration radius increases. MD simulations show that the length scale of the polar/nonpolar domain for 1-butyl-3-methylimidazolium hexafluorophosphate is 12Å, which is significantly smaller than the fully extended oligomers. Using average bond length, the estimated lengths of the oligomers are 30Å, 43Å, 56Å, 83Å for OPPV5, OPPV7, OPPV9, and OPPV13, respectively. To minimize the unfavorable oligomer-polar region interactions, oligomers prefer a morphology that increase the favorable oligomer-oligomer and oligomer-nonpolar region interactions. Due to the short length of the oligomer chain backbones, self-collapse of the chain as observed in MEHPPV, is unlikely. The more likely scenario is that the oligomers formed compact, ordered small aggregates. The polar and nonpolar regions likely prevent formation of large aggregates and force the size distribution of the aggregates to be narrow. Synthesis of nanoparticles in ILs has shown similar effects.[303–307]

The small aggregate model also explains the trends observed in fluorescence anisotropy and the hydration radius. With longer chains, the aggregates will have to compact more densely to reduce unfavorable interactions. Therefore, as chain length increases, the reduction in hydration radius decreases and fluorescence anisotropy also decreases.

Considering the increase in fluorescence lifetime and the red-shift in emission spectra, the aggregates formed could be excimers. Excimers have long radiative lifetime and weak oscillator strength due to the forbidden nature of the transition to the ground state.

Excimers are also typically lower in energy, which explains the red-shift observed in emission spectra. However, emissions from excimer are typically unstructured, due to the unbound nature of the ground state.[296,285,293,294,298,299] While the emission of OPPV9 could potentially be viewed as unstructured. The emission spectra of the other oligomers are clearly structured.

Another possible model is a two-state model, the core-shell model.[308–315] In the core-shell model, the densely-packed core is surrounded by less densely packed shell. The shell gives the structured emission similar to the emission of a single chain. In this model, the red-shift observed in this emission can be attributed to solvatochromism. However, unlike other two-state models, the emission from the core is not observed, and the two-state model cannot explain the increase in fluorescence lifetime observed.

The last model to consider is the H-aggregate and J-aggregate model developed by Kasha and Davydov.[316,317,318] When the chains in the aggregate are strongly interacting, the absorption spectra will be split into two bands, corresponding to the H-aggregate and J-aggregate. If the aggregates formed are primarily H-aggregates, in which the transition moments are aligned out-of-phase, the transition to the ground state is forbidden, and emission is quenched. However, the H-aggregate model does not explain the red-shift observed in the emission spectra.

5.5. Conclusion

In summary, from the reduction in hydration radius and the relative length of the oligomers *versus* nonpolar regions in ILs, we speculate that the oligomers form small compact aggregates. The size of the polar and nonpolar regions in ILs limit the size of the

aggregates formed, and create a narrow size distribution of aggregates. We considered three different aggregation models (excimers, core-shell, and H-aggregate) to explain the changes observed in fluorescence lifetimes and emission spectra. However, none of the models can adequately explain all the observations.

With respect to applications of conjugated polymers in ILs, the significant quenching observed is a disadvantage. However, if the quenching is due to the aggregation of the conjugated polymers, ILs with longer alkyl chains and larger nonpolar domain would likely reduce the number of aggregates formed, and, therefore, reduce the quenching observed.

References

262. Noda, A.; Susan, M. A. B. H.; Kudo, K.; Mitsushima, S.; Hayamizu, K.; Watanabe, M. Brønsted Acid-Base Ionic Liquids as Proton-Conducting Nonaqueous Electrolytes. *J. Phys. Chem. B*, **2003**, *107*, 4024–4033.

263. Xiang, H. F.; Yin, B.; Wang, H.; Lin, H. W.; Ge, X. W.; Xie, S.; Chen, C. H. Improving Electrochemical Properties of Room Temperature Ionic Liquid (RTIL) Based Electrolyte for Li-Ion Batteries. *Electrochimica Acta*, **2010**, *55*, 5204–5209.

264. Abraham, T. J.; MacFarlane, D. R.; Pringle, J. M. Seebeck Coefficients in Ionic Liquids – Prospects for Thermo-electrochemical Cells. *Chem. Commun.*, **2011**, *47*, 6260–6262.

265. MacFarlane, D. R.; Pringle, J. M.; Howlett, P. C.; Forsyth, M. Ionic Liquids and Reactions at the Electrochemical Interface. *Phys. Chem. Chem. Phys.*, **2010**, *12*, 1659–1669.

266. Lane, G. H.; Bayley, P. M.; Clare, B. R.; Best, A. S.; MacFarlane, D. R.; Forsyth, M.; Hollenkamp, A. F. Ionic Liquid Electrolyte for Lithium Melta Batteries: Physical, Electrochemical, and Interfacial Studies of N-Methyl-N-butylmorpholinium Bis(fluorosulfonyl)imide. *J. Phys. Chem. C*, **2010**, *114* 21775–21785.

267. Lane, G. H.; Best, A. S.; MacFarlane, D. R.; Forsyth, M.; Bayley, P. M.; Hollenkamp, A. F. The Electrochemistry of Lithium in Ionic Liquid/Organic Diluent Mixtures. *Electrochimica Acta*, **2010**, *55*, 8947–8952.

268 Tang, J.; Osteryoung, R. A. Formation and Electrochemistry of Polyaniline in Ambient-Temperature Molten Salts. *Synth. Met.*, **1991**, *45*, 1–13.

269 Tang, J.; Osteryoung, R. A. Electrochemistry of Polyaniline in Ambient-Temperature Molten Salts. *Synth. Met.*, **1991**, *44*, 307–319.

270. Lu, W.; Fadeev, A. G.; Qi, B.; Smela, E.; Mattes, B. R.; Ding, J.; Spinks, G. M.; Mazurkiewicz, J.; Zhou, D.; Wallace, G. G.; MacFarlane, D. R.; Forsyth, S. A.; Forsyth, M. Use of Ionic Liquids for π-Conjugated Polymer Electrochemical Devices, *Science*, **2002**, *297*, 983–987.
271. Wang, Y.; Voth, G. A. Unique Spatial Heterogeneity in Ionic Liquids. *J. Am. Chem. Soc.* **2005**, *127*, 12192–12193.
272. Lopes, J. N. A. C.; Gomes, M. F. C.; Pádua, A. A. H. Nonpolar, Polar, and Associating Solutes in Ionic Liquids. *J. Phys. Chem. B*, **2006**, *110*, 16816–16818.
273. Lopes, J. N. A. C.; Pádua, A. A. H. Nanostructural Organization in Ionic Liquids. *J. Phys. Chem. B* **2006**, *110*, 3330–3335.
274. Hettige, J. J.; Kashyap, H. K.; Annapureddy, H. V. R.; Margulis, C. J. Anions, the Reporters of Structure in Ionic Liquids. *J. Phys. Chem. Lett.* **2013**, *4*, 105–110.
275. Inamura, Y.; Yamamuro, O.; Hayashi, S.; Hamaguchi, H. Dynamics Structure of a Room-Temperature Ionic Liquid bmimCl. *Phys. B Condens. Matter* **2006**, *385-386*, 732–734.
276. Yamamuro, O.; Yamada, T.; Kofu, M.; Nakakoshi, M.; Nagao, M. Hierarchical Structure and Dynamics of an Ionic Liquid 1-Octyl-3-Methylimidazolium Chloride. *J. Chem. Phys.* **2011**, *135*, 054508.
277. Triolo, A.; Russina, O.; Fazio, B.; Triolo, R.; Di Cola, E. Morphology of 1-Alkyl-3-Methylimidazolium Hexafluorophosphate Room Temperature Ionic Liquids. *Chem. Phys. Lett.*, **2008**, *457*, 362–365.
278. Annapureddy, H. V. R.; Kashyap, H, K.; De Biase, P. M.; Margulis, C. J. What is the Origin of the Prepeak in the X-ray Scattering of Imidazolium-Based Room-Temperature Ionic Liquids? *J. Phys. Chem. B*, **2010**, *114*, 16838–16846.
279. Castner Jr., E. W.; Margulis, C. J.; Maroncelli, M.; Wishart, J. F. Ionic Liquids: Structure and Photochemical Reactions. *Annu. Rev. Phys. Chem.*, **2011**, *62*, 85–105.
280. Santos, C. S.; Sanjeeva Murthy, N.; Baker, G. A.; Castner Jr., E. W. Communication: X-Ray Scattering from Ionic Liquids with Pyrrolidinium Cations. *J. Chem. Phys.*, **2011**, *134*, 121101.
281. Huser, T.; Yan, M. Solvent-Related Conformational Changes and Aggregation of Conjugated Polymers Studied by Single Molecule Fluorescence Spectroscopy. *J. Photochem. Photobio. A: Chem.*, **2001**, *144*, 43–51.
282. Bolinger, J. C.; Traub, M. C.; Brazard, J.; Adachi, T.; Barbara, P. F.; Vanden Bout, D. A. Conformation and Energy Transfer in Single Conjugated Polymers. *Acc. Chem. Res.*, **1993**, *45* 1992–2001.
283. Oelkrug, D.; Egelhaaf, H.-J.; Gierschner, J.; Tompert, A. Electronic Deactivation in Single Chains, Nano-Aggregates and Ultrathin Films of Conjugated Oligomers. *Synth. Met.*, **1996**, 76, 249–253.
284. Oelkrug, D.; Tompert, A.; Gierschner, J.; Egelhaaf, H.-J.; Hanack, M.; Hohloch, M.; Steinhuber, E. Tuning of Fluorescence in Films and Nanoparticles of Oligophenylenevinylenes. *J. Phys. Chem. B*, **1998**, *102*, 1902–1907.
285. van Hutten, P. F.; Krasnikov, V. V.; Hadziioannou, G. A Model Oligomer Approach to Light-Emitting Semiconducting Polymers. *Acc. Chem. Res.*, **1999**, *32*, 257–265.

286. Bredas, J.-L.; Cornil, J.; Beljonne, D.; dos Santos, D. A.; Shuai, Z. Excited-State Electronic Structure of Oligomers and Polymers: A Quantum-Chemical Approach to Optical Phenomena, *Acc. Chem. Res.*, **1999**, *32*, 267–276.
287. Brédas, J. L.; Beljonne, D.; Cornil, J.; Calbert, J. P.; Shuaí, Z.; Silbey, R. Electronic Structure of π-Conjugated Oligomers and Polymers: A Quantum-Chemical Approach to Transport Properties. *Synth. Met.*, **2001**, *125*, 107–116.
288. Collison, C. J.; Treemaneekam, V.; Oldham Jr., W. J.; Hsu, J. H.; Rothberg, L. J. Aggregation Effects on the Structure and Optical Properties of a Model PPV Oligomer. *Synth. Met.*, **2001**, *119*, 515–518.
289. Peeters, E.; Ramos, A. M.; Meskers, S. C. J.; Janssen, R. A. J. Singlet and Triplet Excitations of Chiral Dialkoxy-p-Phenylene Vinylene Oligomers. *J. Chem. Phys.*, **2000**, *112*, 9445–9454.
290. Schenning, A. P. H. J.; Jonkheijm, P.; Peeters, E.; Meijer, E. W. Hierarchical Order in Supramolecular Assemblies of Hydrogen-Bonded Oligo(p-phenylene vinylene)s. *J. Am. Chem. Soc.* **2001**, *123*, 409–416.
291. Lim, S.-H.; Bjorklund, T. G.; Bardeen, C. J. Characterization of Individual Submicron Distyrylbenzene Aggregates Using Temperature-Depencdent Picosecond Fluorescence and Atomic Force Microscopy. *J. Phys. Chem. B*, **2004**, *108*, 4289–4295.
292. Bussian, D. A.; Summers, M. A.; Liu, B.; Bazan, G. C.; Burratto, S. K. Photon Pair Correlation Spectroscopy of Single Tetrahedral Oligophenylenevinylene Molecules at Room Temperature. *Chem. Phys. Lett.*, **2004**, *388*, 181–185.
293. Gierschner, J.; Oelkrug, D. *Optical Properties of OligophenyleneVinylenes*. American Scientific Publishers, Stevenson Ranch, CA, 2004.
294. Gierschner, J.; Ehni, M.; Egelhaaf, H. J.; Medina, B. M.; Beljonne, D.; Benmansour, H.; Bazan, G. C. Solid-State Optical Properties of Linear Polyconjugated Molecules: π-Stack Contra Herringbone. *J. Chem. Phys.*, **2005**, *123*, 144914.
295. Summers, M. A.; Kemper, P. R.; Bushnell, J. E.; Robinson, M. R.; Bazan, G. C.; Bowers, M. T.; Buratto, S. K. Conformation and Luminescence of Isolated Molecular Semiconductor Molecules. *J. Am. Chem. Soc.*, **2003**, *125*, 5199–5203.
296. Sherwood, G. A.; Cheng, R.; Smith, T. M.; Werner, J. H.; Shreve, A. P.; Peteanu, L. A.; Wildeman, J. Aggregation Effects on the Emission Spectra and Dynamics of Model Oligomers of MEH-PPV. *J. Phys. Chem. C*, **2009**, *113*, 18851–18862.
297. Legaspi, C. M.; Peteanu, L. A.; Yaron, D. J. Modeling Field-Induced Quenching in Poly(p-phenylene vinylene) Polymers and Oligomers. *J. Phys. Chem. B*, **2015**, *119*, 7625–7634.
298. Samuel, I. D. W.; Rumbles, G.; Collison, C. J. Efficient Interchain Photoluminescence in a High-Electron Affinity Conjugated Polymer. *Phys. Rev. B* **1995**, *52*, R11573–R11576.
299. Löwe, C.; Weder, C. Oligo(p-phenylene Vinylene) Excimers as Molecular Probes: Deformation-Induced Color Changes in Photoluminescent Polymer Blends. *Adv. Mater.*, **2002**, *14*, 1625–1629.
300. Jeong, D.; Choi, M. Y.; Kim, H. J.; Jung, Y.J. Fagility, Stokes-Einstein Violation, and Correlated Local Excitations in a Coarse-Grained Model of An Ionic Liquid. *Phys. Chem. Chem. Phys.*, **2001**, *12*, 2001–2010.
301. Zhang, S.; Sun, N.; He, X.; Lu, X.; Zhang, X. Physical Properties of Ionic Liquids: Database and Evaluation. *J. Phys. Chem. Ref. Data.* **2006,** *35*, 1475–1517

302. Kok, C. M.; Rudin, A. Relationship between the Hydrodynamic Radius and the Radius of Gyration of a Polymer in Solution. *Makromol. Chem., Rapid Commun.*, **1981**, *2*, 655–659.
303. Dupont, J.; Fonseca, G. S.; Umpierre, A. P.; Fichtner, P. F. P.; Teixeira, S. R. Transition-Metal Nanoparticles in Imidazolium Ionic Liquids: Recyclable Catalysts for Biphasic Hydrogenation Reactions. *J. Am. Chem. Soc.*, **2002**, *124*, 4228–4229.
304. Fonseca, G. S.; Domingos, J. B.; Nome, F.; Dupont, J. On the Kinetics of Iridium Nanoparticles Formation in Ionic Liquids and Olefin Hydrogenation. *J. Mol. Catal. A: Chemical.*, **2006**, *248*, 10–16.
305. Fonseca, G. S.; Umpierre, A. P.; Fichtner, P. F. P.; Teixeira, S. R.; Dupont, J. The Use of Imidazolium Ionic Liquids for the Formation of Stabilization of Ir^0 and Rh^0 Nanoparticles: Efficient Catalysts for the Hydrogenation of Arenes. *Chem. Eur. J.*, **2003**, *9*, 3263–3269.
306. He, Z.; Alexandridis, P. Nanoparticles in Ionic Liquids: Interactions and Organization. *Phys. Chem. Chem. Phys.*, **2015**, *17*, 18238–18261.
307. Do, I. Drzal, L. T. Room Temperature Ionic Liquids for Size Control of Noble Metal Nanoparticles on Carbon Supports. Carbon, **2014**, *75*, 43–55.
308. Amrutha, S. R.; Jayakannan, M. Probing the π-Stacking Induced Molecular Aggregation in π-Conjugated Polymers, Oligomers, and Their Blends of p-Phenylenevinylenes. *J. Phys. Chem. B*, **2008**, *112*, 1119–1129.
309. Padmanaban, G.; Ramakrishnan, S. Fluorescence Spectroscopic Studies of Solvent- and Temperature- Induced Conformational Transition in Segmented Poly[2-methoxy-5-(2'-ethylhexyl)oxy-1,4-phenylenevinylene] (MEHPPV). *J. Phys. Chem. B*, **2004**, *108*, 14933–14941.
310. Collison, C. J.; Rothberg, L. J.; Treemaneekarn, V. Li, Y. Conformational Effects on the Photophysics of Conjugated Polymers: A Two Species Model for MEH-PPV Spectroscopy and Dynamics. *Macromolecules*, **2001,** *34*, 2346–2352.
311. Ho, P. K. H.; Kim, J.-S.; Tessler, N.; Friend, R. H. Photoluminescence of Poly(p-phenylenevinylene)-Silica Nanocomposites: Evidence for Dual Emission by Franck-Condon Analysis. *J. Chem. Phys.*, **2001**, *115*, 2709–2720.
312. Wang, P.; Cuppoletti, C. M.; Rothberg, L. J. Bimodal Inhomogeneity in Conjugated Polymer Spectroscopy: Experimental Tests of a Two Conformation Model. *Synth. Met.* **2003**, *137*, 1461–1463.
313. Menon, A.; Galvin, M.; Walz, K. A.; Rothberg, L. Structural Basis for the Spectroscopy and Photophysics of Solution-Aggregated Conjugated Polymers. *Synth. Met.*, **2004**, *141*, 197–202.
314. Sumpter, B. G.; Kumar, P.; Mehta, A.; Barnes, M. D.; Shelton, W. A.; Harrison, R. J. Computational Study of the Structure, Dynamics, and Photophysical Properties of Conjugated Polymers and Oligomers under Nanoscale Confinement. *J. Phys. Chem. B*, **2005**, *109*, 7671–7685.
315. Kim, D. Y.; Grey, J. K.; Barbara, P. F. A Detailed Single Molecule Spectroscopy Study of the Vibronic States and Energy Transfer Pathways of the Conjugated Polymer MEH-PPV. *Synth. Met.*, **2006**, *156*, 336–345.
316. Davydov, A. S. *Theory of Molecular Excitons*; McGraw-Hill: New York, 1962.
317. Kasha, M.; Rawls, H. R.; El-Bayoumi, M. A. The Exciton Model in Molecular Spectroscopy. *Pure Appl. Chem.*, **1965**, *11*, 371–392.

318. Spano, F. C. The Spectral Signatures of Frenkel Polarons in H- and J-Aggregates. *Acc. Chem. Res.*, 2010, *43*, 429–439.

Chapter 6. Phase Separation using Supported Polymeric Ionic Liquids

6.1. Introduction

Recently, polymeric ionic liquids (PIL) have attracted interest in several areas, and many different methods for synthesizing PILs have been published.[319–333] In addition to being ILs, PILs offer additional structural support. In material science, PILs have been used in thermoresponsive materials, and anion-sensitive materials.[334–343] For synthesis, PILs have been used as catalysts, support for catalysts, and surfactant for synthesis of nanoparticles.[344–348] In energy storage and fuel cells, PILs have been used in synthesis of conductive polymer, dye-sensitized solar cells, lithium ion batteries, and electrochemical actuators. [349–353] Last, PILs have also been used for CO_2 capture and separation and absorption, such as chromatography and microextraction of pollutants, metal ions, and proteins.[354–361]

Although PILs have been used in a variety of areas, researches to understand PILs have been limited. The structure of PILs and their interactions within themselves and with other molecules are not well understood. For example, the PILs have been successfully incorporated in lithium batteries, that are chemically and thermally stable. However, choosing the right combination of PILs and ILs is difficult. With simulation and better understanding of the interactions between PILs and ILs and with the electrodes, selecting the right combination will become easier.

One of the difficulties with simulations involving PILs is the demand of computational power and time. With the number of atoms in PILs, molecular dynamics (MD) simulation with an all-atom description is slow and demands a lot of computational power. Below, we developed a coarse-grained description for ILs and PILs. The coarse-

grained description cuts the number of atoms in the system by half, and decrease the amount of time by a factor of four. Furthermore, we showed that the IL and PIL structure simulated with the coarse-grained model is similar to that obtained from an all-atom model.

The coarse-grained model was also used to show that block copolymer with PILs can be used to create microstructure by separating a mixture of water and hexane. These materials have been incorporated into electrochemical devices, such as lithium batteries. Elabd *et al.* used the block copolymers as the electrolyte and the separator for lithium batteries.[362,363] They also showed that these block copolymers form microphase-separated morphology, and have higher ion conductivity than batteries with ILs as electrolytes.[329,364] Using coarse-grained model, we showed that the microphase morphology of block copolymers with PILs can be used to form nanometer-scale aqueous and organic layers.

6.2. Simulation Methods

In molecular dynamics, electrons and quantum mechanics are ignored. All motions in the simulation are governed by Newton's classical mechanics and follow Newton's equations of motion. Atoms are modeled as soft spheres, bonds and bond angles are modeled as springs, and dihedral angels are modeled by periodic functions. Potential energy can be separated into the bonded potentials and nonbonding interactions.

$$E_{potential} = E_{bonded} + E_{nonbonding} \quad \text{(Eq. 6.1)}$$

$$E_{bonded} = \sum_{ij} \frac{k_{ij}\left(r_{ij} - r_{ij,0}\right)^2}{2} + \sum_{ijk} \frac{k_{ijk}\left(\theta_{ijk} - \theta_{ijk,0}\right)^2}{2} + \sum_{ijkl}\sum_{n=0}^{5} C_{n,ijkl}\left[\cos(\psi)\right]^n \quad \text{(Eq. 6.2)}$$

$$E_{nonbonding} = \sum_{ij} \epsilon_{ij}\left(\frac{\sigma_{ij}^{12}}{r_{ij}^{12}} - \frac{\sigma_{ij}^{6}}{r_{ij}^{6}}\right) + \sum_{ij} \frac{q_i q_j}{r_{ij}} \quad \text{(Eq. 6.3)}$$

where $k_{ij}, k_{ijk}, C_{n,ijkl},$ and $\epsilon_{ij}\sigma_{ij}$ are force field parameters, $r_{ij,0}$ and $\theta_{ijk,0}$ are the optimal bond length, bond angle, and dihedral angle, respectively, r_{ij} is the distance between *i*th and *j*th particles, and q_i, q_j are the charges of the *i*th and *j*th particles. In order to speed up the simulations, coarse-grained force field parameters were developed based on the all-atom force field developed by Lopes *et al*[365,366] and OPLS-AA.[367] For the coarse-grained model, hydrogen atoms are combined with the nearest atom. Therefore, –CH3, –CH2–, and –CH– are modeled as a single sphere. The partial charge of the sphere is the sum of the partial charges of the combined atoms. Parameters related to bond angle and bond length are unchanged, *i.e.* the parameters for the central atom is used for the new sphere. However, the parameters for dihedral and Lennard-Jones parameter had to be adjusted. The new parameters are presented in Table 6.1, and the atom names are shown in Fig. 6.1.

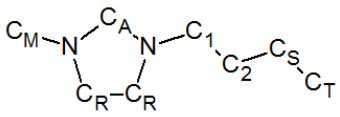

Figure 6.1. Atom names for the coarse-grained model

Table 6.1. Forcefield parameters for the coarse-grained imidazolium cation.

Lennard-Jones Potential and Charges

Atom	Charge	σ (nm)	ϵ (kJ mol^{-1})
C_R	0.08	0.355	0.292880
N	0.15	0.325	0.711280
C_A	0.10	0.350	0.292880
C_M	0.2	0.380	0.276114
C_1	0.09	0.365	0.276114
C_2	0.13	0.365	0.276114
C_S	0.00	0.365	0.276114
C_T	0.00	0.380	0.276114

Dihedral Potential

Dihedral	C_0	C_1	C_2	C_3	C_4	C_5
C-C-C-C	-30	0	60	-60	0	0
N-C-C-C	-80	0	15	-15	0	0

Fig. 6.2 shows the distributions of the dihedral angles for the all-atom simulations and the coarse-grained simulations for 1-butyl-3-methylimidazolium hexafluorophosphate, [Bmim][PF_6]. PF_6 was also simulated using a coarse-grained description. [368] The distribution of the coarse-grained model matched the distribution of the all-atom model fairly well. The coarse-grained model was not able to match the distribution of the *gauche* conformation well, because the Lennard-Jones potential of the sphere pushed the spheres apart.

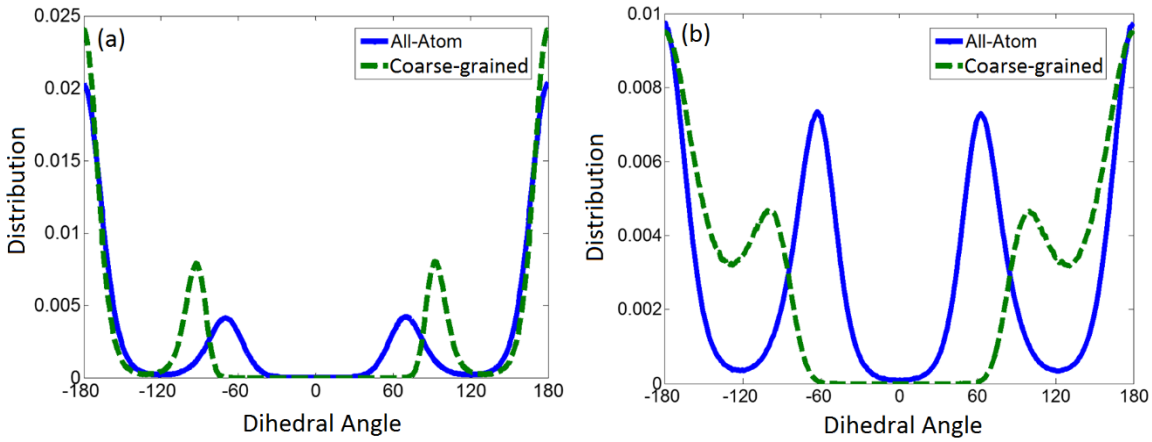

Figure 6.2. Distribution of dihedral angels for all-atom and coarse-grained for [Bmim][BF_6]. (a) The dihedral angle for N-C-C-C of the butyl chain. (b) The dihedral angle for C-C-C-C of the butyl chain.

Figures 6.4 and 6.5 show the radial distribution function of the all-atom model and coarse-grained model for [Bmim][PF_6]. Figure 6.3 shows the atom name for the radial distribution function. Figures 6.4 and 6.5 show that the structure of the coarse-grained IL matched the all-atom IL fairly well. Some small differences were observed, such as the radial distribution of P around P (Fig. 6.5), but those differences were expected, due to approximation of an octahedron with a sphere.

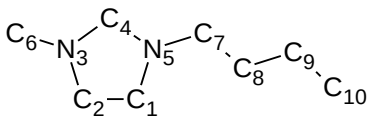

Figure 6.3. Atom names for coarse-grained [Bmim].

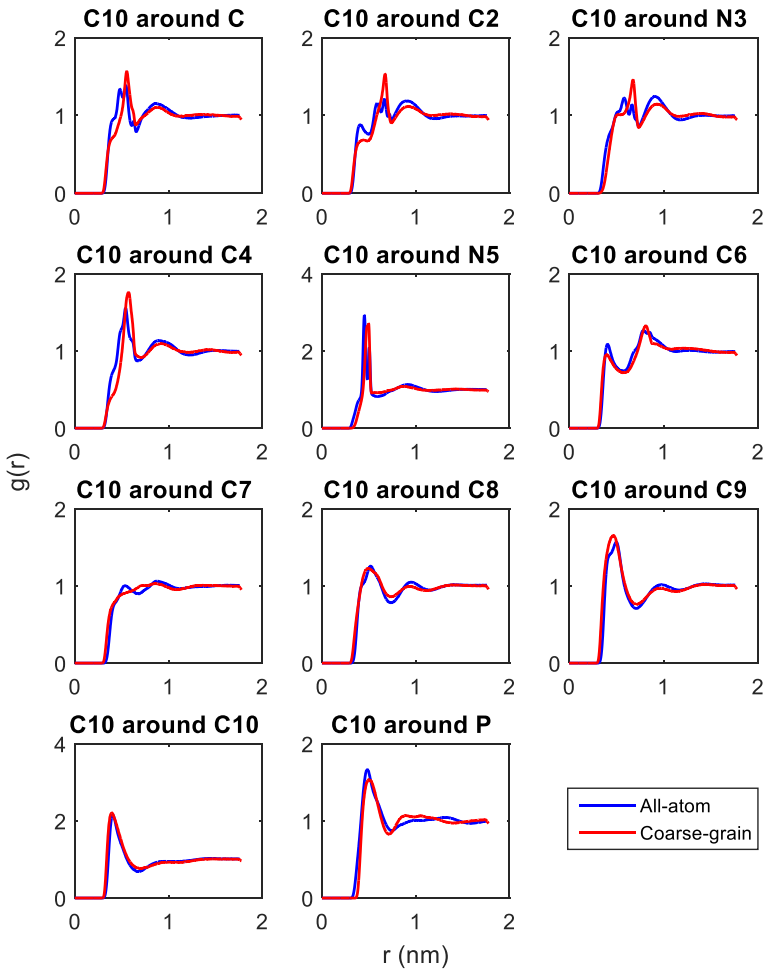

Figure 6.4. Radial distribution of C10 (the last carbon in the butyl chain) around all other atoms.

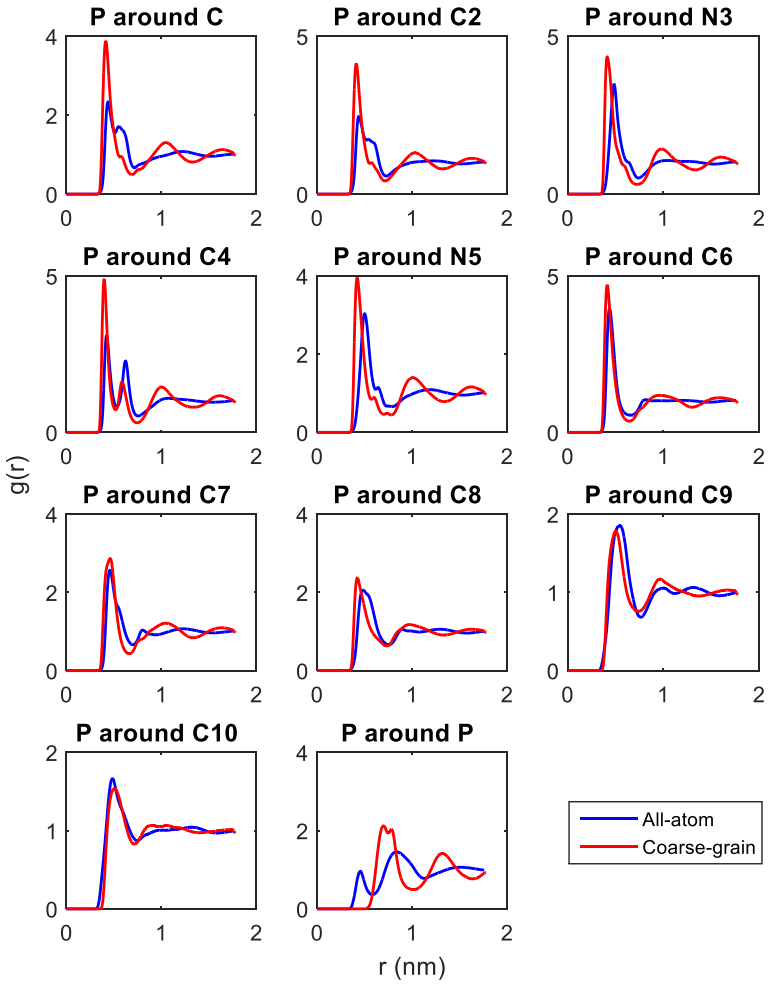

Figure 6.5. The radial distribution of the coarse-grained PF_6 around all other atoms.

Since radial distribution functions only showed pair distribution, the structure of the coarse-grained IL was also examined by simulating graphene-IL supercapacitor. The number density and charge density of the all-atom IL and coarse-grained IL were compared. (Figures 6.6 and 6.7). The simulation system consisted of 256 ion pairs of 1-ethyl-3-methylimidazolium tetrafluoroborate, [Emim][BF_4], sandwiched between 2 parallel graphene electrodes. The graphene electrodes, separated by 6.6 nm, were modeled as two rigid, flat graphene sheets with area 3.396×3.431 nm^2. The electrodes were uniformly charged by changing the partial charges of the carbon atoms so that the surface charge

densities were $\pm 0.43\ e/\text{nm}^2$. The graphene plate at $r = 3.3$ nm was charged negatively, and the graphene plate at $r = -3.3$ nm was charged positively. The ILs were described using the coarse-grained model. After annealing from 700K, the production run was 10 ns long at 350 K.

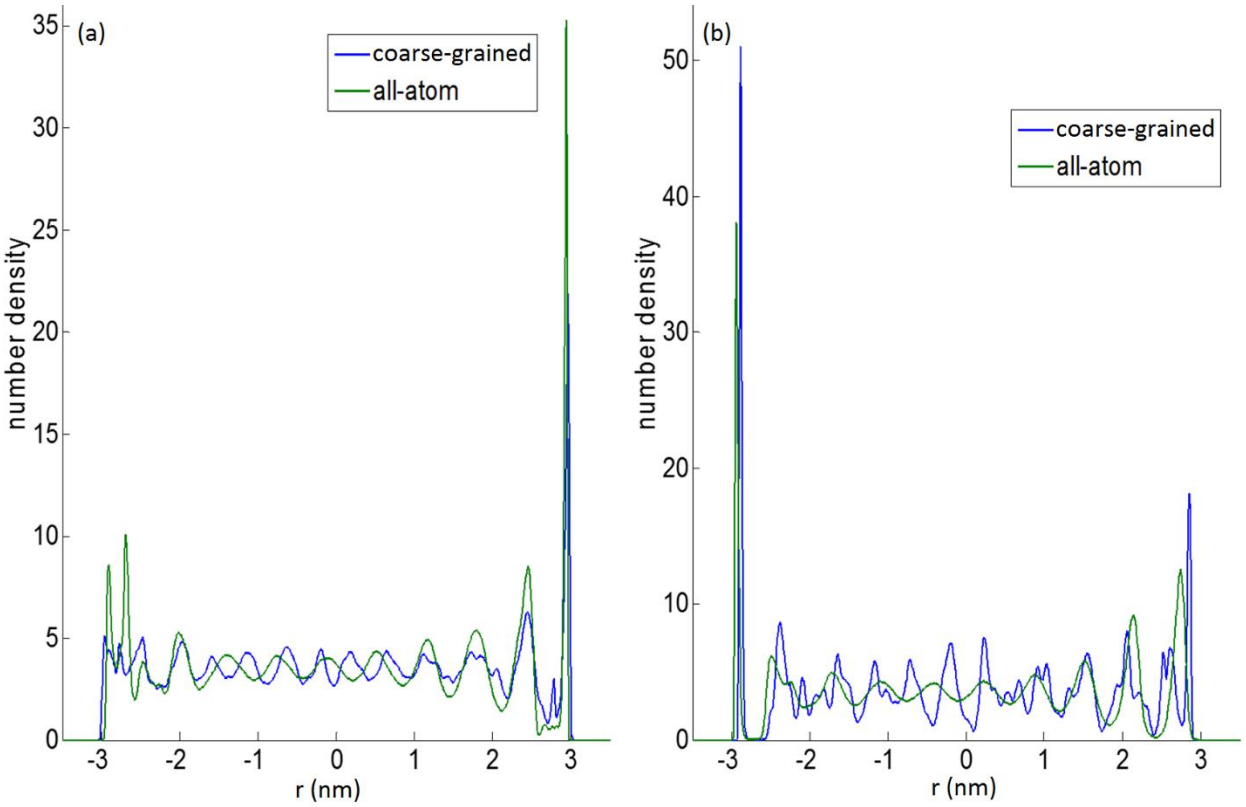

Figure 6.6. Number densities of (a) cation, [Emim], and (b) anion, [BF_4].

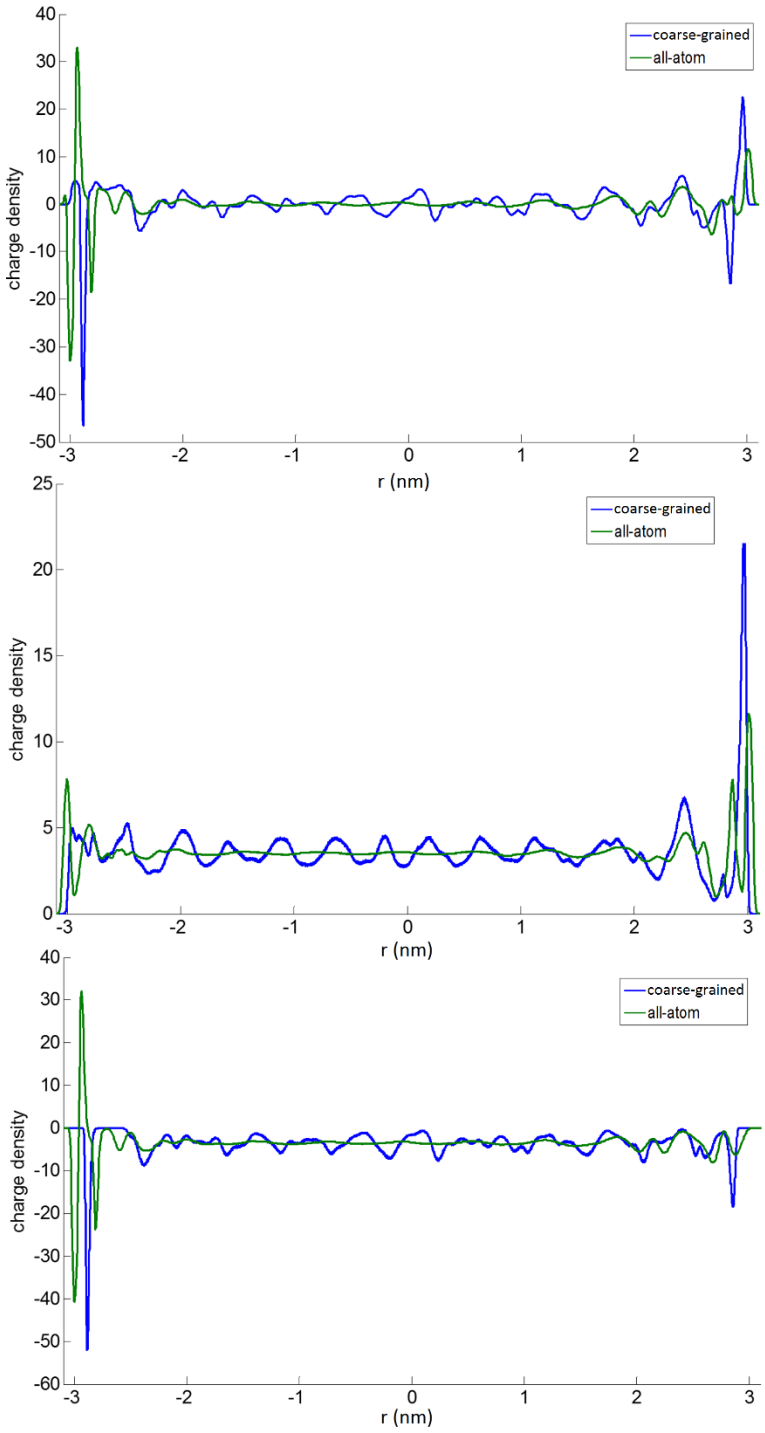

Figure 6.7. Charge densities for (a) cation + anion, (b) cation, and (c) anion.

Number densities showed that the structures of the ILs were similar between the all-atom model and the coarse-grained model. The coarse-grained model was able to capture the structure of the first few layers near the electrodes fairly well. The biggest difference between the two models was that the anion is more structured for the coarse-grained model. For example, near $r = 0$ nm for anion, the anion structure had a large amplitude for the coarse-grained model. Charge densities also showed that the coarse-grained model was more structured than the all-atom model. The charge densities for all-atom model were flat around $r = 0$ nm, but the coarse-grained model showed fluctuations. The charge densities also showed the main drawback of coarse-grained model, the loss of detail. For example, the all-atom charge density of anion near the positive electrode ($r = -3.3$ nm) had 3 peaks, 2 negative peaks and 1 positive peak, but the coarse-grained charge density only had 1 negative peak. The difference was due to combining the fluorine atoms and phosphorus atoms. The 2 negative peaks in the all-atom charge density were due to the negatively charged fluorine atoms, and the positive peak was due to the positively charged phosphorus atom. With coarse-grained model, this detail was lost, and only one negative peak was observed. Overall, the graphene-IL supercapacitor showed that the coarse-grained model captured the general structure of IL fairly well.

With coarse-grained model, the dynamics are faster than the all-atom model. To adjust for the different in dynamics, the temperature of the coarse-grained model has to be multiplied by a temperature factor to get the temperature of the all-atom model. To find the temperature factor, the diffusion constant of [Bmim][PF_6] at several different temperatures were calculated (Figure 6.8). Comparison of the diffusion constants showed that the correction factor for the temperature is 1.4, *i.e.*

$$T_{\text{all-atom}} = 1.4 \times T_{\text{coarse-grained}} \qquad \text{(Eq. 1)}$$

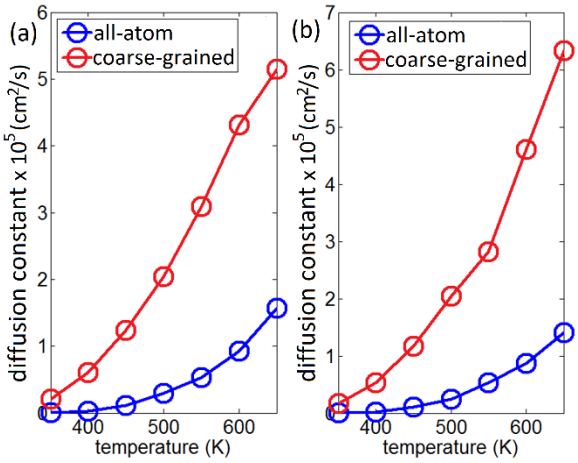

Figure 6.8. Diffusion constants of (a) [Bmim] and (b) [BF_4] using coarse-grained model and all-atom model.

Lastly, to show that the coarse-grained model is able to capture the structure of the polymeric IL. The end-to-end distance and radius of gyration for a polymeric IL were compared. The structure of the polymeric IL is shown in Scheme 6.1. The polymer consisted of a ethene backbone. The R group attached to the backbone is an imidazolium attached to a benzene ring. To compare the structure of the polymeric ILs, a chain with n =20 is solvated with 580 [Emim][Cl] ion pairs. After annealing from 700 K, 10 ns at 350 K was simulated.

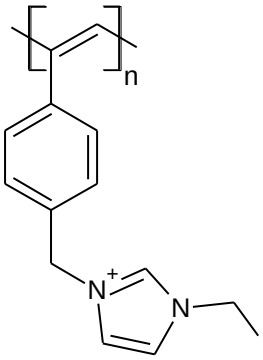

Scheme 6.1. Structure of polymeric anion.

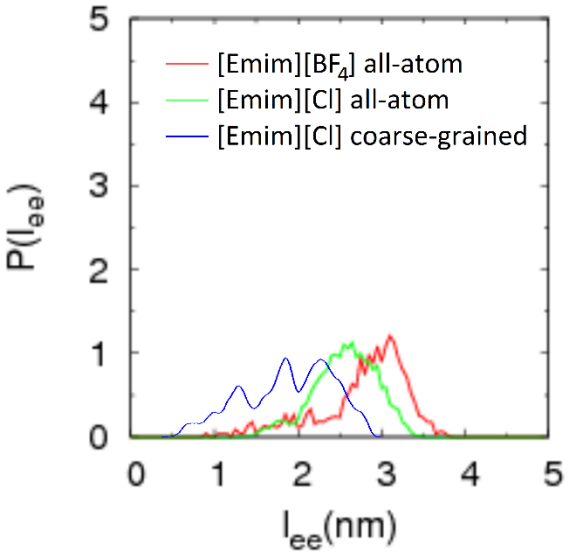

Figure 6.9. End-to-end distance for the polymeric IL with all-atom model and coarse-grained model.[369]

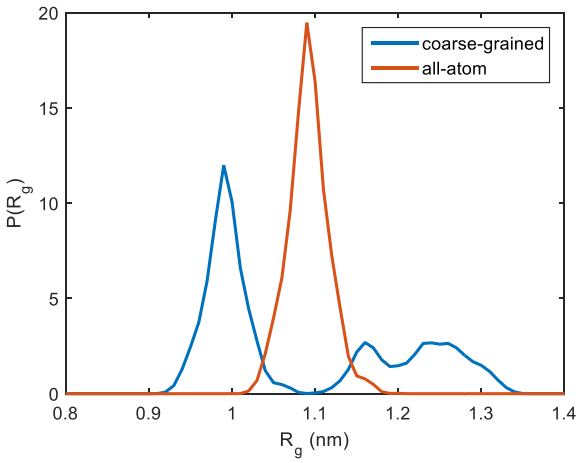

Figure 6.10. Radius of gyration for the polymeric IL with all-atom model and coarse-grained model.[369]

Both the distribution of the end-to-end distance and the distribution of the radius of gyration showed that the coarse-grained description of the polymeric IL was slightly smaller than all-atom description. With the coarse-grained description the backbone of the polymeric IL is less extended than the all-atom description. However, the difference was only about 10%, therefore, the coarse-grained description is still an adequate model for the polymeric IL.

The rest of the chapter will describe the use of the coarse-grained model to simulate block copolymer of polymeric IL for phase separation. The structure of the block copolymer is shown in Scheme 6.2. The block copolymers are attached to a graphene plate with area 4.2×4.2 nm^2. The block copolymers were solvated in water-hexane mixture, and the counterion for copolymer B is $BF4^-$. Another graphene plate is used to keep the solvent molecules from escaping. The simulation details of the 6 systems are summarized in Table 6.2.

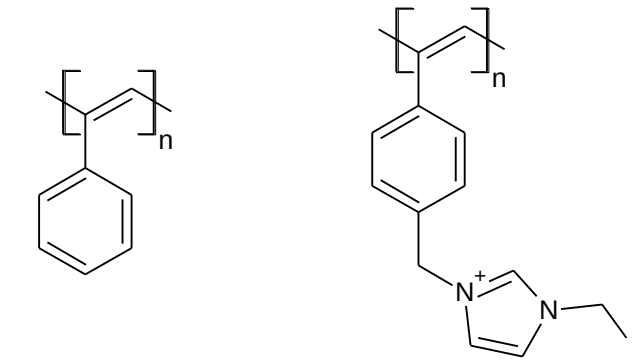

Copolymer A Copolymer B

Scheme 6.2. Structure of the block copolymer.

Table 6.2. Simulation details of the block copolymers.

	Polymer	# of water	# of hexane	# of BF_4
4NPN	4 $A_{15}B_{15}A_{15}$	1114	305	60
2NPN/2PNP	2 $A_{15}B15A_{15}$ 2 $B_{15}A_{15}B_{15}$	1834	251	90
2NPN/2NNP	2 $A_{15}B_{15}A_{15}$ $2A_{15}A_{15}B_{15}$	1271	348	60
2PNN/2PPP	2 $B_{15}A_{15}A_{15}$ 2 $B_{15}B_{15}B_{15}$	2760	189	120
NPN	1 $A_{15}B_{15}A_{15}$	1567	498	15
PNP	1 $B_{15}A_{15}B_{15}$	3579	212	30

The ratio of water to hexane molecules were calculated such that the volume ratio of water to hexane matches the ratio of copolymer B to copolymer A. For example, in NPN, the volume ratio of water to hexane was 1:2, while in PNP, the volume ratio of water to

hexane was 2:1. Each system was annealed from 800 K, and the production runs were 10-ns long at 300 K.

6.3. Results and Discussion

6.3.1. Structure

First, we will look at the structure of the block copolymer and the number density of the hexane and water in the simulation box. Figure 6.11 shows snapshots of 4NPN and NPN. With the block copolymers attached to the graphene plate, the water-hexane mixtures separated into three different layers, instead of just two layers (water and hexane). The block copolymers created a 3-nm layer of water in between the hexane layers. For both 4 NPN and NPN, where the polymers are 3 nm and 6 nm apart, respectively, the water-hexane mixture separated into the 3-layer structure. It is important to note that water and hexane molecules were randomly distributed throughout the box before the systems were annealed. Water and hexane molecules separated throughout the annealing and equilibration processes. To look at the distribution of water and hexane molecules in the simulation box. The number densities along the z-axis are plotted in Fig. 6.12.

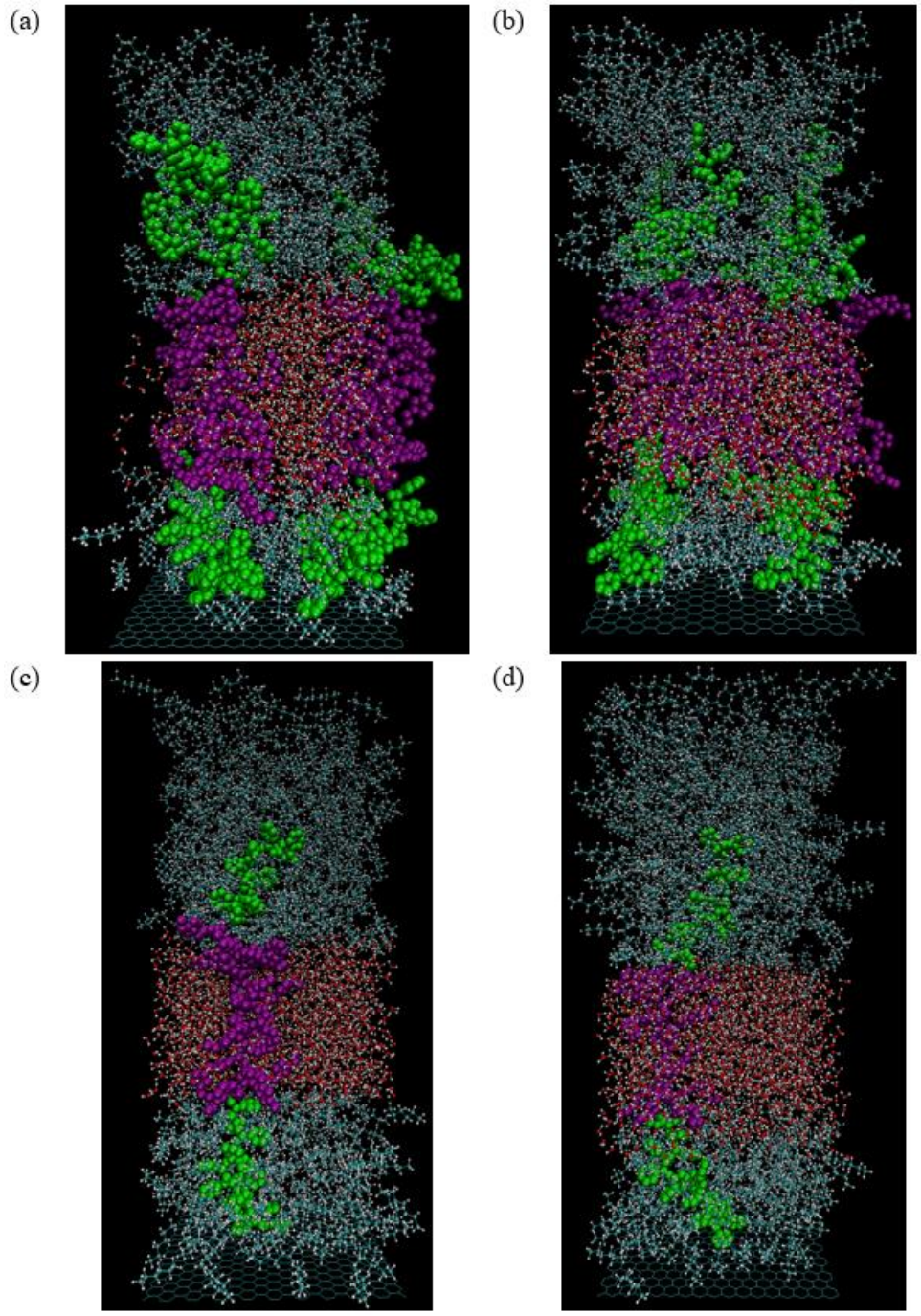

Figure 6.11. Snapshots of 4NPN (a, b) and NPN (c, d). Green – copolymer A (without IL). Purple – copolymer B (with IL). Red/white – water. Green/gray – hexane.

First, we will look at 4NPN and NPN (Figure 6.12a and 6.12e). These two systems showed the most rigid and regular structures. With these two structures, the mixtures separated into three layers. Starting from the graphene plate with the polymers attached, the first two nanometer was a layer of hexane, then a 3-nm water layer, and finally a hexane layer. The layers where water and hexane mixed were only 0.5-nm thick for these two systems.

Next, we will look at systems with different order of copolymers and see if these systems helped water and hexane mix. First, we will look at 2NPN/2NNP (Figure 6.12c). With these two polymers, if the polymers were fully extended, the first layer will only have copolymer A, and the next two layers will have a mix of copolymer A and copolymer B. However, the first two layers of NNP polymer collapsed, and the third segment of NNP polymer lined up with the second segment in the NPN polymer. As a result, the water-hexane mixture separated into three layers. A 3.5-nm layer of water was sandwiched between two layers of hexane. Unlike 4NPN and NPN, the number density of water was not symmetric. In the region between $z = 2$ nm and $z = 3$ nm, the density of copolymer B was higher than the density of the solvents. With 4NPN and NPN, the number densities of the solvent (water or hexane) were always higher or equal to the number densities copolymers, which meant that the copolymers were well solvated. With 2NPN/2NNP, the region between $r = 2$ nm and $r = 3$ nm had higher density of the copolymer than the solvent.

Next, we will look at 2NPN/2PNP and 2PNN/2PPP (Figure 6.12b and 6.12d). With these polymers, the polymers cannot collapse or shift like 2NPN/2NNP, and as a result, some mixing of water and hexane was observed. For 2NPN/2PNP, the regions between

$r = 0.5$ nm and $r = 2.5$ nm contained both water and hexane, which were 4 to 5 times thicker than the mixing regions observed in 4NPN, NPN, or 2NPN/2NNP. For 2PNN/2PPP, a more significant mixing was observed. The regions between $r = 0.5$ nm and $r = 4.5$ nm contained both water and hexane, which is 3.5 nm thicker than the 0.5-nm layer observed in other systems. In these mixing regions, the number densities of the copolymers were higher than the number densities of the solvent, which showed that the copolymers were not well solvated due to the unfavorable interactions.

Lastly, we will look at PNP (Figure 6.12f). For PNP, one would expect to have a hexane layer sandwiched by water layers. However, due to the polymers being far apart (6 nm), the first two layers of the PNP polymer collapsed, and the entire PNP polymer is within 2 nm of the graphene plate. As a result, separation of phase was not achieved using the polymer.

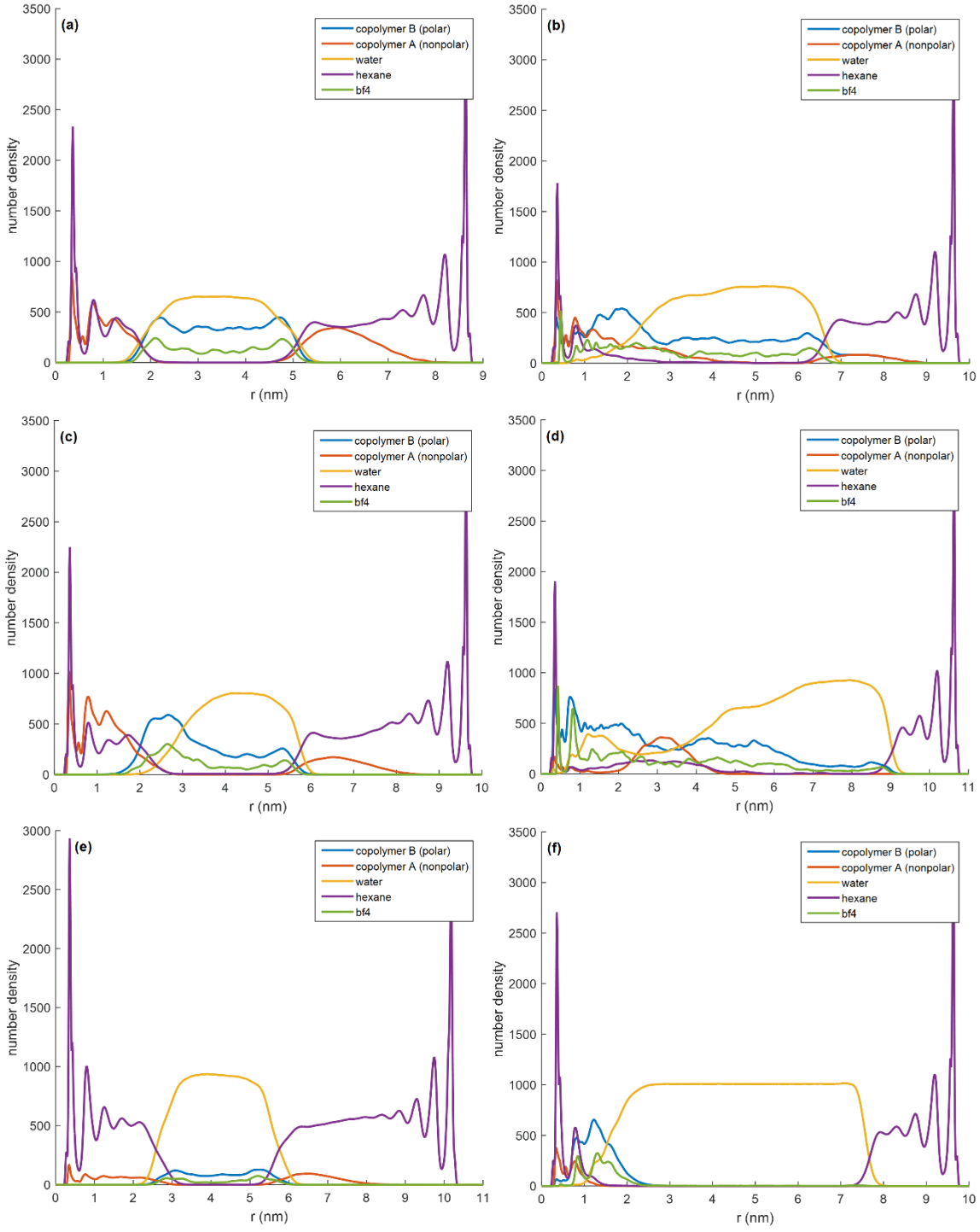

Figure 6.12. Number densities along the z-axis for (a) NPN, (b) 2NPN/2PNP, (c) 2NPN/2NNP, (d) 2PNN/2PPP, (e) NPN, and (f) PNP.

6.2.1. Dynamics

We will examine the diffusion along the xy-plane for the 6 systems. The diffusion constant along the xy-plane, D_{xy} is tabulated in Table 3. The xy-plane diffusion constant of water for systems with 4 polymers attached was less than the xy-plane diffusion of pure water. For example, for 4NPN, the diffusion constant is a third of that for pure water. When the density of the copolymer decreased, the diffusion constant of water increased. For example, for NPN, the diffusion constant of water was same as that of pure water. Surprisingly, the diffusion constant of hexane was not affected by the presence of the polymers. This means that hexane is not interacting as strongly with the copolymer as water. Water, on the other hand, formed strong hydrogen bonding with the imidazolium hydrogens and BF_4 anion, which is reflected in the decrease in diffusion constant.

Table 6.3. 2D diffusion constant of water and hexane.

	$D_{x,y}$(water) [a]	$D_{x,y}$(hexane) [a]
Pure water/hexane	1.12×10^{-5}	3.91×10^{-5}
4NPN	4.25×10^{-6}	3.56×10^{-5}
2NPN/2PNP	6.59×10^{-6}	4.11×10^{-5}
2NPN/2NNP	7.80×10^{-6}	3.98×10^{-5}
2PNN/2PPP	8.18×10^{-6}	3.52×10^{-5}
NPN	1.24×10^{-5}	5.08×10^{-5}
PNP	1.23×10^{-5}	3.53×10^{-5}

[a] in cm_2/s

6.4. Conclusion

Micro-phase-separation was achieved with block copolymers attached to a graphene plate. With 15-repeating units of each copolymer, water-hexane mixture separated into three layers with a 3-nm water layer in the middle. This structure held even when the distance between the copolymers increased from 3 nm to 6 nm.

On the other hand, when different copolymers occupy the same region in the z-axis, the polymers forced water and hexane to mixed. However, due to the unfavorable interactions, those regions had more copolymers than solvents, which indicated that the copolymers were not well-solvated.

References

319. Gu, Y.; Lodge, T. P. Synthesis and Gas Separation Performance of Triblock Copolymer Ion Gels with a Polymerized Ionic Liquid Mid-Block, *Macromolecules*, **2011**, *44*, 1732–1736.

320. Margaretta, E. Fahs, G. B.; Inglefield, Jr., D. L.; Jangu, C.; Wang, D.; Heflin, J. R.; Moore, R. B.; Long, T. E. Imidazolium-Containing ABA Triblock Copolymers as Electroactive Devices. *ACS Appl. Mater. Interfaces*, **2016**, *8*, 1280–1288.

321. Chen, H.; Choi, J. H.; Salas-de la Cruz, D.; Winey, K. I.; Elabd, Y. A. Polymerized Ionic Liquids: the Effect of Random Copolymer Composition on Ion Conduction. *Macromolecules*, **2009,** 42, 4809–4816.

322. Jovanovski, V.; Marcilla, R.; Mecerreyes, D. Tuning the Properties of Functional Pyrrolidinium Polymers by (Co)polymerization of Diallyldimethylammonium Ionic Liquids. *Macromol. Rapid Commun.* **2010,** *31*, 1646–1651.

323. Vijayakrishna, K.; Jewrajka, S. K.; Ruiz, A.; Marcilla, R.; Pomposo, J. A.; Mecerreyes, D.; Taton, D.; Gnanou, Y. Synthesis by RAFT and Ionic Responsiveness of Double Hydrophilic Block Copolymers Based on Ionic Liquid Monomer Units. *Macromolecules*, **2008**, *41*, 6299–6308.

324. Mori, H.; Yahagi, M.; Endo, T. RAFT Polymerization of N-vinylimidazolium Salts and Synthesis of Thermoresponsize Ionic Liquid Block Copolymers. *Macromolecules*, **2009**, *42*, 8082–8092.

325. Tauer, L.; Weber, N.; Texter, J. Core-Shell Particle Interconversion with Di-Stimuli-Responsive Diblock Copolymers. *Chem. Commun.*, **2009**, *40*, 6065–6067.

326. Vijayakrishna, K.; Mecerreyes, D.; Gnanou, Y.; Taton, D. Polymeric Vesicles and Micelles Obtained by Self-Assembly of Ionic Liquid-Based Block Copolymers Triggered by Anion or Solvent Exchange. *Macromolecules*, **2009**, *42*, 5167–5174.
327. Yuan, J.; Schlaad, H.; Giordano, C.; Antonietti, M. Double Hydrophilic Diblock Copolymers Containing a Poly(Ionic Liquid) Segement: Controlled Synthesis, Solution Property, and Application as Carbon Precursor. *Euro. Polymer J.*, **2011**,*47*, 772–781.
328. Texter, J.; Vasantha, V. A.; Crombez, R.; Maniglia, R.; Slater, L. Mourey, T. Triblock Copolymer Based on Poly9Propylene Oxide) and Poly(1-[11-Acryloylundecyl]-3-Methyl-Imidazolium Bromide). *Macromol. Rapid Commun.*, **2012**, *33*, 69–74.
329. Ye, Y.; Choi, J. H.; Winey, K. I.; Elabd, Y. A. Polymerized Ionic Liquid Block and Random Copolymers: Effect of Weak Microphase Separation on Ion Transport. *Macromolecules*. **2012**, *45*, 7027–7035.
330. Stancik, C. M.; Lavoie, A. R.; Achurra, P. A.; Waymouth, R. M.; Gast, A. P.; A Neutron Scattering Study of the Structure and Water Partitioning of Selectively Deuterated Copolymer Micelles. *Langmuir*, **2004**, *20*, 8975–8987.
331. Yang, W.; He, X.; Gao, J.; Guo, H.; He, X.; Wan, F.; Zhao, X.; Yu, Y.; Pei, B. Synthesis, Characterization, and Tunable Wettability of Poly(Ionic Liquid) Brushes via Nitroxide-Mediated Radical Polymerization (NMP). *Chinese Sci. Bulletin*, **2010**, *55*, 3562–3568.
332. Vygodskii, Y. S.; Shaplov, A. S.; Lozinskaya, E. I.; Lyssenko, K. A.; Golovanov, D. G.; Malyshkina, I. A.; Gavrilova, N. D.; Buchmeiser, M. R. Conductive Polymer Electrolytes Derived from Poly(norborene)s with Pedant Ionic Imidazolium Moieties. *Macromole. Chem. Phys.*, **2008**, *209*, 40–51.
333. Wiesenauer, E. F.; Edwards, J. P.; Scalfani, V. F.; Bailey, T. S.; Gin, D. L. Synthesis and Ordered Phase Separation of Imidazolium-Based Alkyl-Ionic Diblock Copolymers Made via ROMP. *Macromolecules*. **2011**, *44*, 5075–5078.
334. Ma, X.; Crombez, R.; Ashaduzzaman, M.; Kunitake, M. Slater, L. Mourey, T.; Texter, J. Polymer Dewetting via Stimuli Responsive Structural Relaxation-Contact Angle Analysis. *Chem. Commun.*, **2011**, *47*, 10356–10358.
335. He, X.; Yang, W.; Pei, X. Preparation, Characterization, and Tunable Wettability of Poly(Ionic Liquid) Brushes via Surface-Initiated Atom Transfer Radical Polymerization. *Macromolecules*, **2008**, *41*, 4615–4621.
336. Amajjahe, S.; Ritter, H. Supramolecular Controlled Pseudo-LCST Effects of Cyclodextrin-Complexed Poly(Ionic Liquids). *Macromolecules*, **2008**, *41*, 3250–3253.
337. Amajjahu, S.; Ritter, H. Anion Complexation of Vinylimidazolium Salts and its Influence on Polymerization. *Macromolecules*, **2008**, *41*, 716–718.
338. Seno, K.-I.; Kanaoka, S.; Aoshima, S. Synthesis and LCST-type Phase Separation Behavior in Organic Solvents of Poly(Vinyl Ethers) with Pendant Imidazolium or Pyridinium Salts. *J. Polymer Sci. Part A: Polymer Chem.*, **2008**, *46*, 5724–5733.
339. Azzaroni, O; Brown, A. A.; Huck, W. T. S. Tunable Wettability by Clicking into Polyelectrolyte Brushes. *Adv. Mater.*, **2007**, *9*, 151–154.
340. Dobbelin, M.; Tena-Zaera, R.; Marcilla, R.; Iturri, J.; Moya, S.; Pomposo, J. A.; Mecerreyes, D.; Multiresponsize PEDOT-Ionic Liquid Materials for the Deisngn of Surfaces with Switchable Wettability. *Adv. Funct. Mater.*, **2009**, *19*, 3326–3233.

341. Dobbelin, M.; Arias, G.; Loinaz, I. Llarena, I.; Mecerreyes, D.; Moya, S. Tuning Surface Wettability of Poly(3-Sulfopropyl Methacrylate) Brushes by Cationic Surfactant-Driven Interactions. *Macromol. Rapid Commun.*, **2008**, *29*, 871–875.
342. Ishikawa, T.; Kobayashi, M.; Takahara, A. Macroscipoc Frictional Properties of Poly(1-(2-Methacryloyloxy)Ethyl-3-Butyl Imidazolium Bis(trifluoromethanesulfonyl)-imide) Brushes Surfaces in an Ionic Liquid. *ACS Appl. Mater. Interfaces*, **2010**, *2*, 1120–1128.
343. Jia, W.; Wu, Y.; Huang, J.; An, W.; Xu, D.; Wu, W.; Li, F.; Li, G. Poly(ionic Liquid) Brush Coated Electrospun Membrane: A Useful Platform for the Development of Functionalized Membrane Sysmtes. *J. Mater. Chem.*, **2010**, *20*, 8617–8623.
344. Jeon, E. H.; Nguyen, M. D.; Chung, C. I.; Kim, Y. J.; Kim, H. S.; Cheong, M.; Lee, J. S. Polymer-Supported Metylselenite for the oxidative Carbonylation of Aniline. *Appl. Catalysis A: General*, **2007**, *332*, 65–69.
345. Pourjavadi, A.; Hosseini, S. H.; Soleyman, R. Crosslinked Poly(Ionic Liquid) as High Loaded Dual Acidic Organocatalyst. *J. Mol. Catalysis A; Chemical*, **2012**, *365*, 55–59.
346. Zhao, P.; Leng, Y.; Wang. J. Heteropolyanion-Paired Cross-Linked Ionic Copolymer: An Efficient Heterogeneous Catalyst for Hydroxylation of Benzene with Hydrogen Peroxide. *Chem. Engineer. J.*, **2012**, *204–206*, 72–78.
347. Liu, F.; Wang, L.; Sun, Q.; Zhu, L.; Meng, X.; Xiao, F. S. Transesterification Catalyzed by Ionic Liquid on Superhydrophobic Mesoporous Polymers: Heterogeneous Catalysts that are Faster than Homogenous Catalysts. *J. Am. Chem. Soc.*, **2012**, *134*, 16948–16950.
348. Mu, X. D.; Meng, J. Q.; Li, Z. C., Kou, Y. Rhodium Nanoparticles Stabilized by Ionic Copolymers in Ionic Liquids: Long Lifetime Nanocluster Catalysts for Benzene Hydrogenation. *J. Am. Chem. Soc.*, **2005**, *127*, 9694–9695.
349. Li, W.; Fang, J.; Lv, M.; Chen. C.; Chi, X.; Yang, Y.; Zhang, Y. Novel Anion Exchange Membranes Based on Polymerizable Imidazolium Salt for Alkaline Fuel Cell Applications. *J. Mater. Chem.*, **2011**, *21*, 11340–11346.
350. Azaceta, E.; Marcilla, R.; Sanchez-Diaz, A.; Palomares, E.; Mercerreyes, D. Synthesis and Characterization of Poly(1-Vinyl-3-Alkylimidazolium) Iodide Polymers for Quasi-Solid Electrolytes in Dye Sensitized Solar Cells. *Electrochimica Acta*, **2010**, *56*, 42–46.
351. Appetecchi, G. B.; Kim, G. T.; Montanino, M.; Carewska, M.; Marcilla, R.; Mecerreyes, D.; De Meatza, I. Ternary Polymer Electrolytes Containing Pyrrolidinium-Based Polymeric Ionic Liquids for Lithium Batteries. *J. Power Sources*. **2010**, *195*, 3668–3675.
352. Li, M. Yang, L.; Fang, S.; Dong, S. Novel Polymeric Ionic Liquid Membranes as Solid Polymer Electrolytes with High Ionic Conductivity at Moderate Temperature. *J. Membrane Sci.*, **2011**, *366*, 245–250.
353. Zhao, J.; Shen, X.; Yan, F.; Qiu, L.; Lee, S.; Sun, B. Solvent-Free Ionic Liquid/Poly(Ionic Liquid) Electrolytes for Quasi-Solid-State Dye-Sensitized Solar Cells. *J. Mater. Chem.*, **2011**, *21*, 7326–7330.
354. Tang, J.; Tang, H.; Sun, W.; Radosz, M.; Shen, Y. Poly(ionic Liquid)s as New Materials for CO_2 Absorption. *J. Polymer Sci Part A: Polymer Chem.*, **2005**, *43*, 5477–5489.

355. Mineo, P. G.; Livoti, L.; Giannetto, M.; Gulino, A.; Lo Schiavo, S.; Cardiano, P. Very Fast CO_2 Response and Hydrophobic Properties of Novel Poly(Ionic Liquid)s. *J. Mater. Chem.*, **2009**, *19*, 8861–8870.
356. Bhavsar R. S.; Kumbharkar, S. C.; Kharul, U. K. Polymeric Ionic Liquids (PILs): Effect of Anion Variation on Their CO_2 Sorption. *J. Membrane Sci.*, **2012**, *389*, 305–315.
357. Bara, J. E.; Lessmann, S.; Gabriel, C. J.; Hatakeyama, E. S.; Noble, R. D.; Gin, D. l. Synthesis and Performance of Polymerizable Room-Temperature Ionic Liquids as Gas Separation Membranes. *Industrial Engineering & Chemical Research*, **2007**, *46*, 5397–5404.
358. Wang, Y.; Deng, Q. L.; Fang, G. Z.; Pan, M. F.; Yu, Y.; Wang, S. A Novel Ionic Liquid Monolithic Column and its Separation Properties in Capillary Electrochromatography. *Analytica Chimica Acta*, **2012**, *712*, 1–8.
359. Graham, C. M.; Meng, Y.; Ho, T.; Anderson, J.L. Sorbent Coatings for Solid-Phase Microextraction Based on Mixtures of Polymeric Ionic Liquids. *J. Separation Sci.*, **2011**, *34*, 340–346.
360. Mahlambi, M.; Malefetse, T.; Mamba, B.; Krause, R. β-Cyclodextrin-Ionic Liquid Polyurethanes for the Removal of Organic Pollutants and Heavy Metals from Water: Synthesis and Characterization. *J. Polymer Research*, **2010**, *17*, 589–600.
361. Li, J.; Han, H.; Wang, Q.; Liu, X.; Jiang, S. Polymeric Ionic Liquid as a Dynamic Coating Additive for Separation of Basic Proteins by Capillary Electrophoresis. *Analytica Chimica Acta*, **2010**, *674*, 243–248.
362. Nykaza, J. R.; Benjamin, R.; Meek, K. M.; Elabd, Y. A. Polymerized Ionic Liquid Diblock Copolymer as an Ionomer and Anion Exchange Membrane for Alkaline Fuel Cells. *Chem. Engineer. Sci.*, **2016**, *154*, 119–127.
363. Nykaza, J. R.; Savage, A. M.; Pan, Q.; Wang, S.; Beyer, F. L.; Tang, M. H.; Li, C. Y.; Elabd, Y. A. Polymerized Ionic Liquid Diblock Copolymers as Solid-State Electrolyte and Separator in Lithium-Ion Battery. *Polymer*, **2016**, *101*, 311–318.
364. Choi, J.-H.; Ye, Y.; Elabd, Y. A.; Winey, K. I. Network Structure and Strong Microphase Separation for High Ion Conductivity in Polymerized Ionic Liquid Block Copolymers. *Macromolecules*, **2013**, *46*, 5290–5300.
365. Canongia Lopes, J. N.; Deschamps, J.; Pádua, A. A. H. Modeling Ionic Liquids Using a Systematic All-Atom Force Field. *J. Phys. Chem. B* **2004**, *108*, 2038−2047.
366. Canongia Lopes, J. N.; Deschamps, J.; Pádua, A. A. H. Modeling Ionic Liquids Using a Systematic All-Atom Force Field. *J. Phys. Chem. B* **2004**, *108*, 11250.
367. Jorgensen, W. L.; Maxwell, D. S.; Tirado-Rives, J. Development and Testing of the OPLS All-Atom Force Field on Conformational Energetics and Properties of Organic Liquids. *J. Am. Chem. Soc.*, **1996**, *118*, 11225–11236.
368. Jeong, D.; Choi, M. Y.; Kim, H. J.; Jung, Y. J. Fragility, Stokes-Einstein Violation, and Correlated Local Excitations in a Coarse-Grained model of an Ionic Liquid. *Phys. Chem. Chem. Phys.* **2010**, *12*, 2001–2010.
369. All-Atom Data Provided by Dr. YonngSeon Shim.